Institute of Analytical Chemistry, Chemo- and Biosensors

University of Regensburg

Impedance analysis and single ion channel recordings on pore-suspending lipid bilayers based on highly ordered pore arrays

Doctoral Dissertation
Submitted for the Degree of Doktor der Naturwissenschaften
(Dr. rerum naturalis)
of the Faculty of Chemistry and Pharmacy

by
Winfried Römer
born in Höchstädt an der Donau

in June 2004

This work was performed at the Institute of Analytical Chemistry, Chemo- and Biosensors of the University of Regensburg between September 2001 and June 2004 under the supervision of Prof. Dr. Claudia Steinem.

Date of Thesis Defence: 20. 07. 2004

Board of examiners: Chairperson: Prof. Dr. Jörg Daub

First referee: Prof. Dr. Claudia Steinem

Second referee: Prof. Dr. Werner Kunz

Third referee: Prof. Dr. Otto S. Wolfbeis

Acknowledgments

I want to express my most profound gratitude to the following people who contributed to the completion of my dissertation:

First of all, I am very grateful to my supervisor Prof. Dr. Claudia Steinem, who gave me the opportunity to carry out my thesis at the Institute of Analytical Chemistry, Chemo- and Biosensors of the University of Regensburg. She offered help and support whenever I needed it.

I gratefully acknowledge the extensive help of PD Dr. Wolfgang Fischer, who introduced me in single ion channel recordings, especially the voltage-clamp technique, and allowed me to work in his laboratory at the Department of Biochemistry of the University of Oxford. He was an excellent collaborator.

I am likewise thankful to Stefan Schweizer, Petra Göring, Ulrike Rehn and Ralph Wehrspohn from the Max-Planck Research Center for Microstructure Physics in Halle (Saale). They introduced me in the complex field of electrochemical pore formation in semiconductors and scanning electron microscopy.

I very much enjoyed working at the Institute of Analytical Chemistry, Chemo- and Biosensors with its unique familiar atmosphere and generous working conditions.
I would like to thank all the people who worked at this institute during the course of my PhD studies and made it a pleasure for me to be there!

The realization of this thesis was supported by the Bundesministerium für Bildung und Forschung (BMBF) within the nanobiotechnology project.

Furthermore, I would like to thank my best friends Stefan Jenning, Rolf Hörger, Michael Wörnzhofer and Christoph Grünewald. It was good to have them around!

Last but not least, I would like to thank the three most important persons in my life, my parents, Johann and Carola Römer, for mental and material support during my whole studies and Karin for all that cannot be described with words.

TABLE OF CONTENTS

1 INTRODUCTION 1

1.1 Biological membranes 1

1.2 Artificial membrane model systems 3

1.2.1 Lipid vesicles 3

1.2.2 Langmuir monolayers 4

1.2.3 Solid supported membranes 5

1.2.4 Freestanding black lipid membranes 7

1.2.5 Lipid bilayers suspending microfabricated apertures 8

1.3 Membrane channels 9

1.3.1 Ion channel formation by self-assembly of antibiotic peptides 10

1.3.1.1 Gramicidin 10

1.3.1.2 Alamethicin 12

1.3.2 Ion channel formation by self-assembly of Vpu transmembrane domains 14

1.3.2.1 Structure and function of full-length Vpu and its transmembrane fragment 14

1.3.2.2 Inhibition of ion channel activity 15

2 AIM OF THIS THESIS 16

3 ANALYTICAL AND PREPARATIVE METHODS 17

3.1 Analytical methods 17

3.1.1 Scanning electron microscopy 17

3.1.1.1 Principle of scanning electron microscopy 17

3.1.1.2 Scanning electron microscopy setup 18

3.1.2 Electrical impedance spectroscopy 18

3.1.2.1 Principle of impedance spectroscopy 18

3.1.2.2 Review of AC circuits 19

3.1.2.3 The impedance Z 20

3.1.2.4 Forms of data presentation 21

3.1.2.5 Equivalent circuits modeling 23

3.1.2.6 Impedance setup 24

3.1.3 Fluorescence intensity recordings 26

3.1.4 Single channel recordings 26

3.1.4.1 Principle of voltage-clamping 26

3.1.4.2 Current measurement circuitry 28

3.1.4.3 Channel recording setup 29

3.2 Preparative methods 30

3.2.1 Fabrication of porous substrates 30

3.2.1.1 Porous alumina 31

3.2.1.2 Macroporous silicon 39

3.2.2 Functionalization of porous substrate surfaces 44

3.2.2.1 Deposition of a thin gold layer 44

3.2.2.2 Self-assembled monolayers on gold-covered porous substrates 45

3.2.3 Formation of pore-suspending lipid bilayers by the painting technique 45

3.2.3.1 Formation of nano-BLMs and micro-BLMs 45

3.2.3.2 Formation of porous matrix-supported BLMs 46

3.2.4 Formation of pore-suspending lipid bilayers by vesicle spreading and fusion . 46

3.2.4.1 Formation of pore-suspending lipid bilayers by spreading and fusion of thiolipid-containing vesicles 47

3.2.4.2 Formation of pore-suspending lipid bilayers by spreading and fusion of positively charged DODAB vesicles to negatively charged porous substrate surfaces 48

4 RESULTS 49

4.1 Characterization of the porous substrates 49

4.1.1 Porous alumina 49

4.1.1.1 Impedance analysis of the pore opening process of porous alumina 50

4.1.1.2 Characterization of porous alumina by scanning electron microscopy 54

4.1.2 Macroporous silicon 56
4.1.2.1 Electrochemical characterization of macroporous silicon 56
4.1.2.2 Characterization of macroporous silicon by scanning electron microscopy 57
4.2 Formation of pore-suspending lipid bilayers by the painting technique 59
4.2.1 Formation and stability of nano-BLMs based on porous alumina 59
4.2.1.1 Thinning out process of the solvent 63
4.2.1.2 Long-term stability of nano-BLMs followed by impedance spectroscopy 64
4.2.1.3 Long-term stability of nano-BLMs investigated by fluorescence intensity recordings 66
4.2.2 Formation and stability of micro-BLMs based on macroporous silicon 69
4.2.2.1 Formation of micro-BLMs 69
4.2.2.2 Long-term stability of micro-BLMs 71
4.2.3 Formation and stability of porous matrix-supported BLMs based on porous substrates 73
4.2.3.1 Formation of porous matrix-supported BLMs 73
4.2.3.2 Stability of porous matrix-supported BLMs 74
4.3 Formation of pore-suspending lipid bilayers by vesicle spreading and fusion 76
4.3.1 Lipid bilayer formation via spreading of thiolipid-containing vesicles 76
4.3.1.1 Vesicle spreading and fusion on planar gold electrodes 76
4.3.1.2 Vesicle spreading and fusion on porous alumina substrates 79
4.3.1.3 Calculation of the pore coverage 84
4.3.2 Formation of lipid bilayers based on porous alumina via electrostatic attractions 86
4.4 Ion channel recordings after peptide incorporation in pore-suspending lipid bilayers... 87
4.4.1 Impedance analysis of gramicidin doped nano-BLMs 87
4.4.2 Single channel recordings of ion channels integrated in pore-suspending lipid bilayers 88
4.4.2.1 Single channel recordings of gramicidin in nano-BLMs 89

4.4.2.2 Single channel recordings of synthetic Vpu$_{1-32}$ in micro-BLMs and porous matrix-supported BLMs 91

4.4.2.3 Single channel recordings of alamethicin in nano-BLMs and porous matrix-supported BLMs 96

5 DISCUSSION 100

5.1 Choice of porous substrates 100

5.2 Formation of pore-suspending lipid bilayers by the painting technique 102

5.2.1 Nano- and micro-BLMs based on prefunctionalized porous substrates 102

5.2.2 Porous matrix-supported BLMs formed without prefunctionalization of the porous substrate 106

5.3 Formation of pore-suspending lipid bilayers by vesicle spreading and fusion 107

5.4 Ion channel insertion in pore-suspending lipid bilayers 110

5.4.1 The dimeric gramicidin channel in nano-BLMs 110

5.4.2 Ion channel activity of synthetic peptide Vpu$_{1-32}$ integrated in micro-BLMs and porous matrix-supported BLMs 111

5.4.3 The voltage-gated alamethicin bundle integrated in nano-BLMs and porous matrix-supported BLMs 114

6 SUMMARY AND OUTLOOK 116

7 REFERENCES 121

ANNEX 135

STATEMENT OF INDEPENDENCE 144

1 INTRODUCTION

1.1 Biological membranes

Biological membranes maintain the spatial organization of life. Membranes defined the boundaries of the first living cells and still work to shield cellular metabolism from changes in the environment. They also organize the interior of eukaryotic cells by separating compartments for specialized purposes. Membranes are not static barriers, but active structures. To function effectively, they must selectively pass molecules and ions from one side to the other.

Early on, lipids were identified as the major component of membranes. Lipids are amphiphilic compounds with a small hydrophilic headgroup attached to long hydrocarbon chains. It was recognized that hydrophobic compounds passed more readily than water-soluble ones through biological membranes. These observations resulted in the notion that biological membranes have a hydrophobic character. The calculation that the lipid content was twice that needed for a single layer led to the concept of the lipid bilayer (Gorter and Grendel, 1925) [1, 2]. In a lipid bilayer, the lipids are aligned with the headgroups facing the water on either surface of the membrane and the hydrophobic hydrocarbons sandwiched in between [3-6].

The fluid mosaic model

In 1972, S.J. Singer and G.L. Nicolson proposed the *fluid mosaic model* for the membrane structure [6], which suggested that membranes are dynamic structures composed of lipids and proteins. In this model, the lipid bilayer is a fluid matrix, in essence, a two-dimensional solvent for proteins, because the components are not held together by bonds but are free to diffuse and move independently within the plane of the membrane. Both lipids and proteins are capable of rotational and lateral movement. Transverse motion may also occur, but is more unlikely.

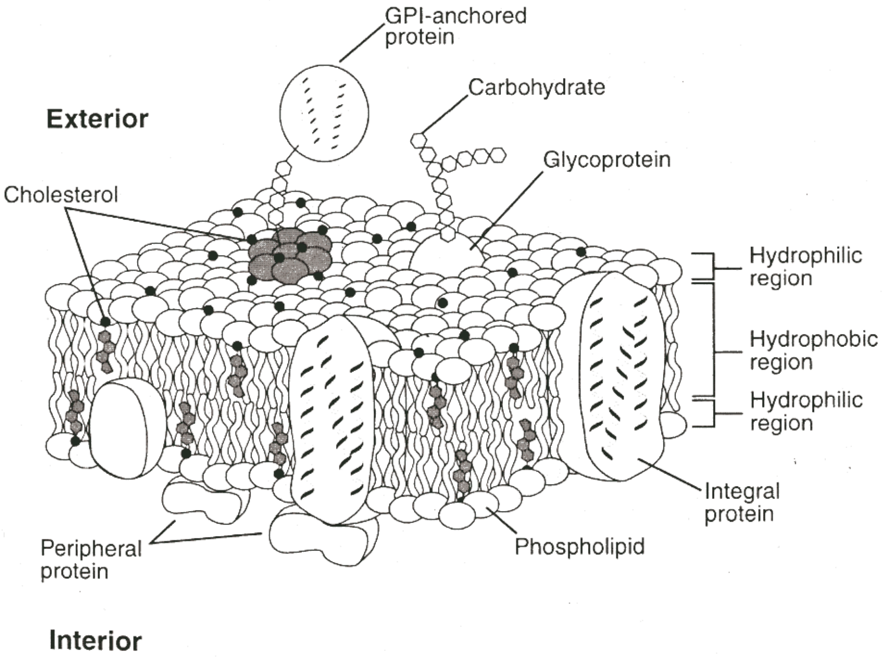
GPI-anchored protein
Carbohydrate
Exterior
Glycoprotein
Cholesterol
Hydrophilic region
Hydrophobic region
Hydrophilic region
Integral protein
Peripheral protein
Phospholipid
Interior

FIGURE 1: Schematical representation of a biological membrane based on the *fluid mosaic model* proposed by Singer and Nicolson in 1972 (from [5]).

Singer and Nicolson pointed out that proteins can be associated with the membrane surface (peripheral proteins) by virtue of ionic interactions and hydrogen bonds or be embedded in the bilayer to varying degrees (integral proteins). The *fluid mosaic model* suggested a value of approximately 5 nm for membrane thickness, the same thickness as a lipid bilayer itself [6]. A schematical representation of a biological membrane, based on the *fluid mosaic model*, is displayed in Fig. 1.

The strategy underlying biological membrane function is that the best barrier between aqueous compartments is a hydrophobic lipid layer. The water-soluble compounds being present within cells and in theirs environments, are not soluble in the lipid milieu of the membrane and pass slowly or not at all through a thin lipid layer. This mechanism has a number of advantages which life has exploited. First, the lipid bilayer is a natural structure and assembles spontaneously. Second, the structure is flexible and allows for growth and movement as well as for the insertion and operation of protein machinery. Finally, the structure has a low dielectric constant giving the membrane electrical properties which are used in signalling, transport and energy transduction. The structure determines the fundamental properties of fluidity, permeability and membrane potential [3-5].

Although the lipid bilayer is basically a symmetrical structure, natural membranes are not. Membranes in nature are known to have intrinsically an asymmetrical distribution of lipids, as well as to form laterally organized functional microdomains enriched in certain types of lipids in liquid-ordered phase (glycosphingolipids, sphingomyelin), cholesterol and a subset of membrane proteins. Such domains, called ´rafts´, are postulated to play key roles in complex cellular functions such as signal transduction or endocytic traffic [3-5, 7, 8].

1.2 Artificial membrane model systems

One of the major challenges in bioscience today is the biomimesis of the cell membrane required for the investigation of membrane related processes like cell adhesion, photosynthesis or nerve excitation. The physical properties and functional roles of individual species in membranes are exceedingly difficult to ascertain in an intact biological membrane due to its complex composition. In order to gain insight into the roles of individual components, it is necessary to construct appropriate membrane model systems. Different artificial systems mimicking the properties of cell membranes have been created, e.g. lipid vesicles, Langmuir monolayers, black lipid membranes and solid supported membranes, for understanding the function of lipid bilayers and membrane proteins.

1.2.1 Lipid vesicles

Vesicles, also referred as liposomes, are microscopic spherical lipid bilayers enclosing a volume of aqueous solution. Preparation of this simple membrane model system involves the hydration of a lipid film by vortexing under low shear conditions. The probability of vesicle formation depends on the nature of the lipid, temperature, water content, ionic ambience and pressure. It is possible to form multilamellar vesicles

(MLVs) by hydration of certain phospholipids. MLVs are concentric phospholipid spheres formed one inside the other in diminishing size and separated by narrow aqueous spaces. Small unilamellar vesicles (SUVs) can be prepared from MLVs by ultrasonic irradiation [9] or by passage through a French press.

The most popular technique for preparing large unilamellar vesicles (LUVs) involves the direct extrusion of MLVs under moderate pressure through polycarbonate filters of defined pore size [10]. This process can generate LUVs with size distributions in the range of 50-1000 nm depending on the pore size of the employed filter. Extrusion does not require detergents or solvents, which are difficult to remove, and it can be applied to all lipids which adopt bilayer stuctures. This technique is rapid, straightforward and convenient.

Lipid vesicles can be used, besides models of biomembranes, as drug carriers and be loaded with a great variety of molecules, such as proteins, nucleotides, and even plasmids [11]. The main drawback of small vesicles is that owing to their minute size, powerful electrical methods cannot be applied at the present time.

1.2.2 Langmuir monolayers

Besides vesicles as spherical model membranes, there exist planar lipid layers as membrane models. Amphipathic lipids are spread from a dilute solution in a volatile solvent on a water-subphase of a Langmuir trough made of Teflon. The solvent evaporates and the lipids orient at the air-water interface to a lipid monolayer which represents half of a bilayer where the polar regions are in the aqueous phase and the acyl chains point to air. Such films, called Langmuir monolayers, can be laterally compressed by barriers of the Langmuir trough. Moveable barriers seal the sides of the water surface so that the surface area can be varied.

A characteristic parameter of the system is the surface tension γ. γ can be measured as the force acting on a plate or a filter paper (Wilhelmy system). The surface tension of a clean water surface at room temperature is $\gamma_{\text{water}} = 72.4$ mN/m. The difference:

$$\pi = \gamma_{\text{water}} - \gamma \qquad \textbf{(Eq-1)}$$

is called surface pressure. A study of the surface pressure as a function of surface area occupied by the monolayer film, called surface-pressure-area isotherms, yields information on the molecular packing of the lipids. In these experiments, the molecules at the interface are compressed, resulting in an increase in surface pressure at a certain area per molecule because the molecules repel each other. Phase transitions of the system, i.e. the chain ordering transition of lipids, appear in the isotherm as regions of constant pressure (first order phase transition with a coexistence of two phases) or as a kink (second order phase transition). Aside from the area per molecule, other external parameters can be varied on a Langmuir trough: temperature, content of salt, polymers or proteins in the subphase.

Langmuir monolayers consisting of phospholipids rank among model membranes, even if they only represent a single monolayer [12].

1.2.3 Solid supported membranes

For technological applications, the lifetime and mechanical stability of the membrane are extremely important. Planar lipid bilayers deposited onto solid surfaces, called solid supported membranes (SSMs), have overcome the problems of black lipid membranes (see chapter 1.2.4) and have opened a range of possibilities in developing practical planar membrane biosensors. A multitude of surface sensitive analytical techniques such as scanning probe microscopy [13], surface plasmon resonance spectroscopy [14] and quartz crystal microbalance technique [15, 16] can be applied for their characterization. SSMs are typically stable for several days [17-19] and have been used e.g. as models of cell surfaces to study cell adhesion processes [20], or in biosensor applications [21].

The Langmuir-Blodgett (LB)-technique is the oldest method to transfer lipid layers onto a solid substrate [22]. To produce a LB-film, a hydrophilic substrate (e.g. mica, glass) is vertically raised from the aqueous phase through a monolayer film at the air-water-interface while keeping the surface pressure constant. The lipid monolayer adheres on the solid support. A second monolayer can be transferred by a second vertically dip of the solid support so that a lipid bilayer is formed. However, this second transfer via the LB-technique can only be used for certain phospholipids.

The Langmuir-Schäfer (LS)-technique is more suited for this purpose [23]. In this case, a horizontally oriented hydrophobic substrate is lowered until it touches the monolayer at the air-water-interface. The transfer of the monolayer occurs by the break-through of the water surface. The transferred bilayer is stable if it is kept in aqueous solution. A lipid bilayer can be formed on a hydrophilic substrate by combination of the LB- and LS-technique.

Another conventional method to prepare SSMs is the spreading and fusion of lipid vesicles on pretreated hydrophilic solid substrates like glass, mica or quartz [18, 24-26]. This membrane formation technique was first described in 1984 by Brian and McConnell [27, 28]. The lipid layers are attached to the solid substrate typically via ionic or *Van der Waals* interactions.

The self-assembly of lipids, leading to a hydrophobic monolayer, also enables the formation of lipid bilayers on solid supports. Sulphur-bearing alkanethiols or thiolipids [29, 30] chemisorb on clean gold surfaces in a self-assembly process [31] and act as hydrophobic monolayer substrates for the formation of hybrid bilayers. Monolayers of alkanethiols on gold are probably the most widely used and best characterized self-assembly films to date. Lipid vesicle spreading or alternatively a Langmuir-Schäfer transfer complement the self-assembled monolayer (SAM) by a second lipid monolayer, resulting in a stable, solvent-free lipid bilayer [32]. The fixation of the first monolayer to the solid substrate results in a robustness and stability of several days not provided by black lipid membranes [18, 33].

However, the close proximity of the artificial membrane to the solid support does not provide a sufficiently thick water reservoir to allow integration of complex transmembrane spanning proteins and to avoid denaturation of protein subunits. This problem can be overcome by separating the membrane from the solid substrate by ultrathin hydrophilic polymer supports [34], such as polymer cushions [35] and tethers [36], which improve both the mobility and functionality of proteins.

1.2.4 Freestanding black lipid membranes

Freestanding lipid bilayers, also known as black lipid membranes (BLMs), are favorite model membranes for electrophysiologists interested in current flow across a bilayer. Two techniques, still used today, have been developed in the 1960s and early 70s. Both make use of a setup made of two Teflon half-chambers separated by a very small hole.

In the first case, BLMs are formed by dissolving lipids in a non-volatile hydrocarbon solvent (e.g. *n*-decane) and painting a lipid droplet across the small aperture (0.1-2 mm in diameter) in a Teflon wall, which separates two aqueous compartments. This technique was established and first published by Müller and Rudin in 1963 [37]. Optical inspection of BLMs shows interference colors immediately after painting. Over time, the organic solvent thins out and collects at the perimeter of the aperture, leaving behind a lipid layer which at its thinnest part is a 5-7 nm thick lipid bilayer. This lipid bilayer film across the center appears in a homogeneous black color [38]. The decrease of their reflectance to a black color upon thinning has given them their name - black lipid membranes.

A serious problem of BLMs formed by the Müller-Rudin technique, is the presence of the organic solvent which has a marked effect on the properties of lipid bilayers and inserted proteins. White et al. showed that the use of squalene as solvent enables solvent-free bilayers to be formed by the conventional Müller-Rudin technique [39]. This effect is associated with a very low solubility of squalene in the bilayer, which leads to its entire displacement into the meniscus surrounding the membrane.

The second technique, first described by Montal and Müller in 1972 [40], makes use of the apposition of two individual monolayers of phospholipids that always form at the water surface after evaporation of their volatile organic solvent (e.g. chloroform). When raising the water level of both chambers beyond the small hole in the Teflon wall, the two lipid monolayers get in contact through the hydrophobic fatty acid parts to form a lipid bilayer.

A great advantage of this system is that asymmetric bilayers can be formed and that they are essentially solvent-free.

The electrical properties of a BLM are readily measured by employing electrodes in the two buffered compartments. It is possible to incorporate membrane proteins and to record voltage-dependent ion fluxes. However, a BLM formed in the conventional manner is an extremely fragile structure with a limited lifetime that last not longer than 8 hours [38] although a number of improvements have been made to prolong the lifetime and mechanical stability by use of a variety of chemical additives [41]. The preparation of solid-supported BLMs (e.g. tethered BLMs or metal-supported BLMs), gel-supported BLMs and S-layer-supported BLMs enabled the application of BLMs as biosensor devices [41, 42].

1.2.5 Lipid bilayers suspending microfabricated apertures

In recent years, the formation of highly insulating lipid bilayers suspending single apertures in macromachined supports has been favored since these membrane systems exhibiting membrane resistances in the GΩ regime, have opened a range of possibilities in developing chip-based planar biosensors which are amenable to electrophysiological and surface-sensitive analytical techniques.

There exists a broad variety of used supports varying in material (polycarbonate filters, silicon, glass or Teflon) and aperture sizes in the micrometer range (0.7-800 µm). Osborn and Yager reported on the formation of planar solvent-free lipid bilayers by the LB-transfer of monolayers to micromachined apertures in silicon [43]. Fertig et al. covered an aperture in a planar glass substrate with lipid bilayers and cells [44-46]. The formation of lipid bilayers covering a pore with a diameter between 2-800 µm was reported by Mayer et al. [47].

Lipid membranes suspending single apertures manufactured in diverse substrates were prepared with various techniques ranging from monolayer transfer to spreading and fusion of unilamellar vesicles. Most of the techniques for lipid bilayer formation were already described in the preceding chapters. Typical long-term stabilities of pore-suspending lipid bilayers suited for single channel recordings were reported to be in the order of several hours [43-45, 48-56]. Their suitability as ion channel sensor devices was tested by recording channel activity of antibiotic peptides like gramicidin. But the pore-suspending lipid bilayers have not really overcome the long-term stability problem of freestanding black lipid membranes exhibiting stabilities in the same order.

With regard to the automation and parallelization of recordings in membrane-based high-throughput screening assays, highly ordered pore arrays consisting of hundreds of pores are desired as supports for pore-suspending lipid bilayers. Already in 1978, Mountz and Tien formed pigmented lipid membranes in microporous filters [57]. Favero et al. formed mixed hybrid lipid bilayers on randomly distributed pores in polycarbonate filters and performed single channel recordings [53, 54]. Just recently, Mayer et al. prepared lipid bilayers suspending three pores of equal diameter (120 µm) in amorphous Teflon [47]. But till now, there is a lack in pore-suspending lipid bilayers based on highly ordered pore arrays in the nano- and micrometer range and in their characterization concerning stability and membrane-specific parameters.

1.3 Membrane channels

Membrane channels comprising gated ion channels and pores are crucial components of living cells [58]. They provide one of the major avenues of communication across cell membranes. As opposed to carriers which diffuse across the bilayer, ion channels and pores maintain a fixed position as the transported molecules pass through them and therefore exhibit distinct conductance states in electrical recordings. Ion channels handle ions and small molecules, whereas water-filled pores can also transport larger molecules [59, 60]. The patch-clamp technique has allowed the activity of individual channels to be measured [38, 61-68], and recombinant DNA technology has revealed fascinating details on channel structure.

An ion channel is usually composed of merely a few protein molecules, sometimes of only one. It consists of two main functional units: the ′gate′ and the ′pore′. The pore is the pathway of penetrating ions through the membrane, and the gate is the mechanism to switch on and off the ion flux. This arrangement allows ions to flow through the channel at rates up to 100 million ions per second when it is open [69].

In general, ion channels are categorized into three types in terms of the biological signals for the gating. The first category are voltage-dependent channels. The voltage-dependent potassium and sodium channel, which respond to voltage changes in neural cells with opening the channels are among this category. The second class of channels are ligand-gated (receptor-operated) channels, which are activated by contact with their specific ligands. The nicotinic acetylcholine receptor ion channel ranks among this type of ion channels. The third kind of channels are mechanosensitive channels that are controlled by the extension of the cell membrane. Channels of this type are located in stress receptors such as muscle spindle or are involved in the control of osmotic pressure in cells [60].

Furthermore, ion channels can show selectivity in the ions to which they are permeable [70]. Some of them permit only particular ions to pass through, such as sodium, calcium or chloride ions; others are selective for broader groups of ions, such as monovalent cations, or cations in general.

1.3.1 Ion channel formation by self-assembly of antibiotic peptides

The ability of antibiotic peptides to form ion channels in membranes has been an active area of investigation since the seminal observations on alamethicin by Müller and Rudin in 1968 [71]. The motivations to study these molecules are diverse and include the development of antibacterial and antiviral agents.

Gramicidin and alamethicin are typical small peptide antibiotics that form ion channels in membranes. These two peptides are found to be prototypic of two quite different modes of membrane channel formation.

1.3.1.1 Gramicidin

Gramicidin is a peptide antibiotic produced by *Bacillus brevis* and toxic to gram-positive bacteria. The natural occuring mixture of gramicidin A, B, C contains about 80 % gramicidin A and is called gramicidin D. Gramicidin is a linear hydrophobic pentadecapeptide formed by an alternating sequence of *D*- and *L*-amino acids. The common primary sequence of gramicidin is as follows:

HCO-*L*-Val-Gly-*L*-Ala-*D*-Leu-*L*-Ala^{5}-*D*-Val-*L*-Val-*D*-Val-*L*-Trp-*D*-Leu^{10}-*L*-X-*D*-Leu-
L-Trp-*D*-Leu-*L*-Trp-$NHCH_2CH_2OH$,

where X is tryptophan in gramicidin A, phenylalanine in gramicidin B and tyrosine in gramicidin C. The amino acid residues are all non-polar, the N-terminus is formylated and the C-terminus is coupled to ethanolamine, so that the molecule is highly non-polar and therefore very lipid-soluble.

The alternating *D*- and *L*-amino acids allow the formation of a single-stranded right-handed β-helix with 6.3 residues per turn [59]. The hydrophobic side chains point away from the axis and are oriented towards the lipid. The interior of the helix is an open cylindrical pore lined with polar carbonyl groups. Each gramicidin molecule can span one monolayer of a lipid membrane. Ion channels spanning the entire bilayer are formed by two gramicidin monomers each diffusing in one monolayer of the lipid bilayer. In a conducting dimer, the two monomers are placed head-to-head with their N-termini in near contact leading to a symmetrical structure, as is shown in Fig. 2.

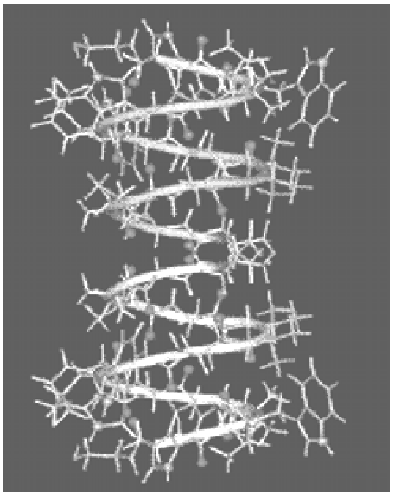

FIGURE 2: Solid-state NMR derived structure of a gramicidin A ion channel. Two gramicidin monomers are placed head-to-head with their N-termini in near contact forming a helical dimer [72].

Six intermolecular H-bridges between the amino termini of two gramicidin monomers cause the formation of a helical dimer acting as an ion channel with a pore diameter of approximately 4 Å and a pore length of 25-30 Å [70, 73, 74]. The absence of a net dipole and any charged amino acids may explain the lack of voltage dependence in gramicidin.

The biological function of gramicidin in transcriptional regulation [74] appears to be unrelated to its most interesting biophysical activity: it readily enters lipid bilayers to form ion channels permeable to monovalent cations, first recorded by Hladky and Haydon in 1970 [70, 75, 76].

Because of their relatively simple structure, gramicidin channels have been and still are frequently used as model system for transmembrane ion permeation. Interactions with ions and water molecules in the channel probably occur mainly at the peptide bond carbonyl groups, which are exposed to the inside of the β-helix [74].

1.3.1.2 Alamethicin

Alamethicin, produced by the fungus *Trichoderma viride*, is the best known member of the class of fungal antibiotics known as peptaibols. Presumably, its antibiotic effect results from forming channels in the bacterial plasma membrane. It is a 20 amino acid peptide rich in hydrophobic amino acids, in particular α-amino isobutyric acid (Aib). The primary sequence of alamethicin is as follows:

$$\text{Ac-Aib-Pro-Aib-Ala-Aib}^{5}\text{-Ala-Gln-Aib-Val-Aib}^{10}\text{-Gly-Leu-Aib-Pro-Val}^{15}\text{-}$$
$$\text{Aib-Aib-Glu-Gln-Phol.}$$

The N-terminus of the peptide is blocked and the C-terminal residue is *L*-phenylalaninol (Phol). Such peptaibol peptides which contain several Aib residues have a strong propensity to form helices. X-ray diffraction studies of alamethicin crystals show that each molecule is largely a single α-helix with a bend at the proline residue at position 14 [62, 77].

Alamethicin is capable of forming voltage-gated channels of very high conductance in lipid membranes. The voltage sensitivity of alamethicin channel formation has given rise to much speculation. The alamethicin α-helix exhibits a dipole moment of around 75 Debye. This dipole moment is related to the alignment of the dipole moments of each individual peptide bond in its α-helical conformation leading to a positive N-terminal end and a negative C-terminal end [78]. In the absence of an electric field, the alamethicin monomers lie on the surface of the membrane (Fig. 3*A*). Applying a potential across the membrane leads to an orientation of the peptide dipoles along the electric field and thus pulls the monomers into the membrane and orients them with their N-termini to the negative side (Fig. 3*B*) [62, 74, 77, 79-81]. The orientated alamethicin monomers self-assemble to bundles in lipid bilayers (Fig. 3*C*) in the presence of a transmembrane potential [81].

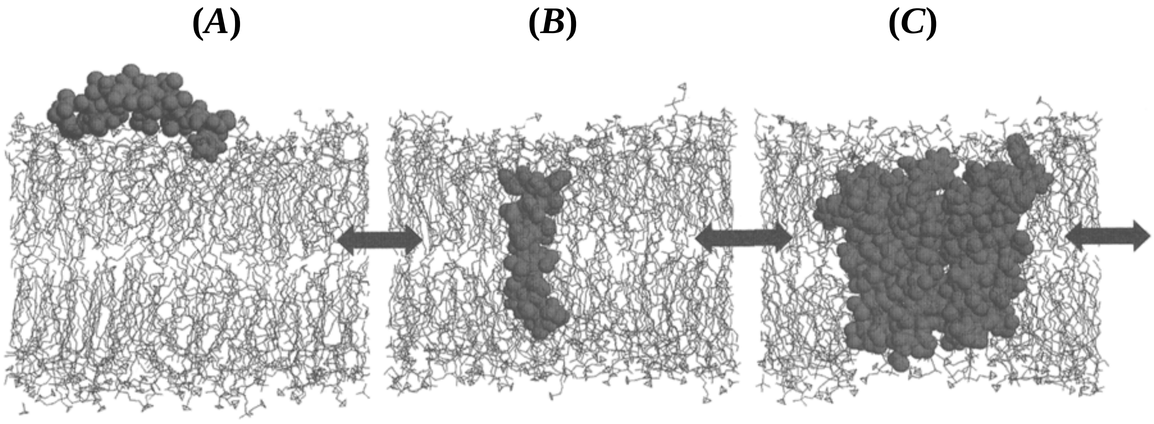

FIGURE 3: Summary of alamethicin molecular dynamics simulations: (*A*) Single alamethicin molecule at the surface of a 1-palmitoyl-2-oleoyl-*sn*-glycero-3-phosphocholine (POPC) bilayer. (*B*) Single alamethicin molecule spanning a POPC bilayer. (*C*) Alamethicin helix bundle consisting of seven monomers. In each case alamethicin is shown in space-filling format, the POPC molecules are presented in bonds format, and the water molecules are omitted for clarity (adapted from [69, 82]).

Usually alamethicin shows multilevel conductances that are thought to come from the different association numbers of alamethicin molecules (up to 10 or 11 monomers) forming the bundle [80]. The conductance changes up or down due to the uptake or release of peptide monomers from the conducting bundle [82-84].

1.3.2 Ion channel formation by self-assembly of Vpu transmembrane domains

Vpu is an example, where fragments of a protein exhibit ion channel activity. When these short peptide fragments are assayed in planar lipid bilayers they show many of the properties associated with the parent structure [85]. A sequence of 20-23 amino acids of high hydrophobicity is sufficient to define a transmembrane segment, if this is in an α-helical conformation. For a β-sheet conformation, less than half of this number would be required, if the β-strands are not tilted [59, 60].

1.3.2.1 Structure and function of full-length Vpu and its transmembrane fragment

Part of the genome of the human immunodeficiency virus type 1 (HIV-1) encodes for Vpu, a small 81 amino acid integral membrane protein that forms cation-selective ion channels [86, 87]. Since the virus needs the protein for amplification rather than strict survival it is also defined as an accessory protein. Vpu associates with Golgi and endoplasmatic reticulum membranes but has not been detected in the viral envelope nor in the plasma membrane of cells.

Vpu comprises a highly hydrophobic N-terminal helical transmembrane (TM) domain encompassing residues 8-25 and a large hydrophilic phosphorylated cytoplasmatic C-terminal domain (Fig. 4) [86-90]. These two distinct structural domains of Vpu exhibit independent functionalities: whilst the latter domain is involved in the degradation of the virus receptor CD4 in the endoplasmatic reticulum, the former domain enhances viral release/secretion from the cell surface [88, 90]. Recent studies showed that the cytoplasmatic domain encompassing two shorter amphipathic in-plane helices [85, 91], furthermore regulates the lifetime of the TM channel in the conductive state [85].

The scheme in Fig. 4 illustrates the incorporation of full-length Vpu and its transmembrane domain in a lipid bilayer.

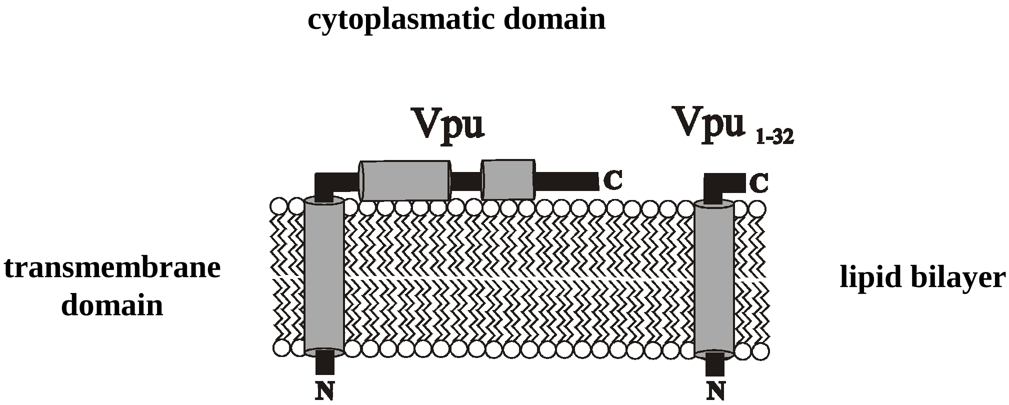

FIGURE 4: Schematic diagram of the structure of full-length Vpu and its transmembrane domain (Vpu$_{1\text{-}32}$) indicating its topology relative to the lipid bilayer. Vpu consists of an N-terminal membrane spanning helical domain and two C-terminal helical domains that lie parallel to the membrane plane. (Modified from [85]).

Reconstitution of synthetic Vpu fragments in lipid bilayers identified an ion channel activity for a sequence corresponding to the helical TM domain of Vpu forming a water-filled bundle of an undetermined number of monomers in membranes [85, 88, 92]. The synthetic oligopeptide Vpu$_{1\text{-}32}$ corresponding to the N-terminal 32 amino acids of Vpu, exhibits a molecular weight of 3544 g mol^{-1} and the following primary sequence [88]:

Met-Gln-Pro-Ile-Pro-Ile-Val-Ala-Ile-Val^{10}-Ala-Leu-Val-Val-Ala-Ile-Ile-Ile-
Ala-Ile^{20}-Val-Val-Trp-Ser-Ile-Val-Ile-Ile-Glu-Tyr^{30}-Arg-Lys.

1.3.2.2 Inhibition of ion channel activity

A lot of ion channels show sensitivity against specific antagonists (or agonists), such as tetrodotoxin for the sodium channel, and thus are major targets for the development of new drugs. Amiloride derivatives have been shown to block channel activity and the enhancement of virus-like particle budding caused by Vpu and might thus be identified as potential antagonists [88].

2 AIM OF THIS THESIS

Approximately one third of all proteins of an organism comprising pores, ion channels, receptors, and enzymes are membrane associated. These proteins require a lipid bilayer for proper function, which makes it difficult to handle them. However, membrane proteins, and in particular ion channels and receptor proteins, are main drug targets, and thus, they have received widespread recognition for their application in biosensors, drug discovery, and protein/ligand screening. Therefore, appropriate model membrane systems were designed with the vision of mimicking the cell membrane. They should exhibit the key features found in natural membranes: fluidity, long-term and mechanical stability, gigaohmic electrical resistance, water on both sides and incorporation of proteins. However, as yet neither of the existing membrane systems combines all features attributed to a cell membrane.

The aim of this work was to obtain a new artificial membrane system that is on the one hand attached to a solid support so that it can be applied in chip technology with the future perspective to conduct high-throughput screening (HTS) assays based on electrochemical or sensitive surface analysis tools. On the other hand this membrane system should exhibit such high membrane resistances that it is suited for single ion channel measurements.

A new strategy based on lipid membranes suspending millions of pores of a porous matrix was followed. These pore-suspending lipid bilayers represent a hybrid between a solid supported membrane (SSM) and a freestanding lipid bilayer (BLM) combining the merits of both.

The suitability of pore-suspending lipid bilayers as biosensor devices was analyzed with the ion channels gramicidin, alamethicin as well as Vpu, a viral transmembrane protein encoded by HIV, exhibiting characteristic conductance states.

3 ANALYTICAL AND PREPARATIVE METHODS

3.1 Analytical methods

3.1.1 Scanning electron microscopy

Scanning electron microscopy (SEM) is one of the best known and most widely used surface analytical techniques. SEM, accompanied by X-ray analysis, is considered a relatively rapid, inexpensive, and basically non-destructive method for surface analysis. High resolution images of surface topography are produced using a highly focused, scanning (primary) electron beam in vacuum.

3.1.1.1 Principle of scanning electron microscopy

Primary electrons enter the surface of interest with an energy of 0.5-30 keV, and generate low energy secondary electrons that are released by the specimen. The intensity of these secondary electrons is largely governed by the surface topography of the sample. An image of the sample surface can thus be constructed by measuring the secondary electron intensity as a function of the position of the scanning primary electron beam. The primary electron beam can be focused to very small spots (< 10 nm) so that a large lateral resolution is obtained in order to generate magnifications in the range of 85- to 50000-fold, or sometimes greater. In addition to low energy secondary electrons, backscattered electrons and X-rays are also generated by primary electron bombardment. The intensity of backscattered electrons can be correlated to the atomic number of the element within the sampling volume. Hence, some qualitative elemental information can be obtained. The analysis of characteristic X-rays emitted from the sample gives more quantitative elemental information [93, 94].

3.1.1.2 Scanning electron microscopy setup

Surface images of porous alumina and silicon substrates were recorded by scanning electron microscopy with a Joel JSM 6300 F and a ZEISS DSM 950 scanning microscope. The non-conductive alumina substrates were covered with a 25-40 nm thick gold layer depending on the pore sizes to render them conductive. The silicon substrate is a semiconductor, but was also covered with a 100 nm thick gold layer to be further used as substrate for bilayer immobilization. The substrates were mounted into the specimen chamber that was evacuated to approximately 10^{-6} hPa. The SEM images were conducted with a 10-15 keV electron beam.

3.1.2 Electrical impedance spectroscopy

Electrochemical impedance spectroscopy (EIS) is a valuable, powerful technique to investigate the electrical properties of electrochemical systems and processes, and is therefore widely used in different research fields such as corrosion, characterization of thin films and coatings, electrode kinetics, semiconductors, batteries, fuel cells and many more. In the last decade, EIS gained growing importance in the fields of biophysics and biosensor technologies [19]. It enables the characterization of lipid membranes and the analysis of the activity and functionality of peptides incorporated into solid supported membranes [95, 96]. The reason for this popularity is the high information content of EIS. It provides a more thorough understanding of an electrochemical system than any other electrochemical technique.

3.1.2.1 Principle of impedance spectroscopy

In principle, there are two different methods to obtain impedance spectra: measurements in the frequency or in the time domain. The most common method, mainly used by commercially available devices, is the frequency domain method or harmonic analysis. A sinusoidally varying AC potential $V(\omega, t)$ with an amplitude typically in the range of V_0 = 5-10 mV is applied to the electrochemical system and the resulting current response $I(\omega, t)$ is measured. Impedance spectra are obtained by sequential measurements of $V(\omega, t)$ and $I(\omega, t)$ for each single frequency that contributes to the spectrum. The amplitude of the applied signal is chosen to be small in order to maintain a pseudo-linear response of the system. In a linear (or pseudo-linear) system, the current response to a sinusoidal potential will be also sinusoidal at the same frequency, but shifted in phase and different in amplitude.

3.1.2.2 Review of AC circuits

A sinusoidal voltage can be expressed as:

$$V(\omega,\ t)\ =\ V_0 \sin(\omega t) \qquad \textbf{(Eq-2)}$$

or in complex notation as:

$$V(\omega,\ t)\ =\ V_0\ e^{i\omega t}, \qquad \textbf{(Eq-3)}$$

where $V(\omega, t)$ is the voltage at time t, V_0 the voltage amplitude, and ω the radial frequency, related to the frequency f according to:

$$\omega = 2\pi f. \qquad \textbf{(Eq-4)}$$

One frequently wishes to consider the relationship between two related sinusoidal signals, such as the current $I(\omega, t)$ and the voltage $V(\omega, t)$. They generally will not be in phase; thus their vectors will be separated by a phase shift $\varphi(\omega)$. The current can be expressed as [97, 98]:

$$I(\omega,\ t)\ =\ I_0(\omega)\ \sin(\omega t\ +\ \varphi(\omega)) \qquad \textbf{(Eq-5)}$$

or in complex notation as:

$$I(\omega,\ t)\ =\ I_0\left(\omega\right)\ e^{i((\omega t\text{-}\varphi(\omega))},\qquad \textbf{(Eq-6)}$$

where $I(\omega, t)$ is the current at time t, $I_0(\omega)$ the current amplitude and $\varphi(\omega)$ the phase shift between voltage and current.

3.1.2.3 The impedance *Z*

The applied potential and the resulting current are both frequency-dependent variables. An expression analogous to Ohm´s law for a DC circuit calculates the frequency-dependent impedance of the system as the ratio of voltage and current. The impedance $Z(\omega)$ can be represented in polar coordinates as:

$$Z(\omega)\ =\ \frac{V(\omega,\ t)}{I(\omega,\ t)}\ =\ \frac{V_0\ e^{i\omega t}}{I_0\left(\omega\right)\ e^{i((\omega t\text{-}\varphi(\omega))}}\ =\ \left|Z(\omega)\right|\ e^{i\varphi(\omega)},\qquad \textbf{(Eq-7)}$$

where $|Z(\omega)|$ is the absolute magnitude of the impedance and $\varphi(\omega)$ is the phase.
The quantity $Z(\omega)$ can also be given in its complex form:

$$Z(\omega)\ =\ \left(Z^{\mathrm{Re}}(\omega)\ +\ i\ Z^{\mathrm{Im}}(\omega)\right),\qquad \textbf{(Eq-8)}$$

where $Z^{\mathrm{Re}}(\omega)$ is the real part and $Z^{\mathrm{Im}}(\omega)$ is the imaginary part of the impedance. The absolute magnitude of the impedance $|Z(\omega)|$, which is the length of the vector (see Fig. 5) can be expressed as:

$$\left|Z(\omega)\right|\ =\ \sqrt{\left(Z^{\mathrm{Re}}(\omega)\right)^2+\ \left(Z^{\mathrm{Im}}(\omega)\right)^2}\ ,\qquad \textbf{(Eq-9)}$$

and the phase angle $\varphi(\omega)$ is defined as:

$$\varphi(\omega)\ =\ \arctan\left(\frac{Z^{\mathrm{Im}}(\omega)}{Z^{\mathrm{Re}}(\omega)}\right).\qquad \textbf{(Eq-10)}$$

3.1.2.4 Forms of data presentation

As the frequency-dependent impedance $Z(\omega)$ is a complex quantity, the data presentation leads to a 3-dimensional curve. In this work, the impedance is expressed in 2-dimensional presentations.

In the so called Bode plot, the logarithm of the absolute magnitude $|Z(\omega)|$ and the phase shift $\varphi(\omega)$ of the impedance are plotted versus the logarithm of the frequency (see Fig. 5*B*) [99]. In a Bode plot, a pure resistance results in a horizontal line and a constant phase shift of $\varphi(\omega) = 0°$, while a pure capacitance leads to a straight line of slope -1 and a constant phase shift of $\varphi(\omega) = -90°$. The simulated impedance data in Fig. 5 are calculated according to an equivalent circuit representing a lipid bilayer. The circuit is composed of a parallel circuit of a resistance R_2 and a capacitance C in series to a resistance R_1 (Fig. 5*A*). At high ($f > 10^4$ Hz) and low ($f < 1$ Hz) frequencies, the electrical behavior of the simulated system (Fig. 5*A*) is resistor-like and the phase angle is nearly zero. R_1 and R_2 can be extracted in these frequency-independent domains. At intermediate frequencies, the imaginary component of the impedance increases. The capacitance C can be calculated from:

$$\log|Z| = -\log(2\pi fC) \qquad \textbf{(Eq-11)}$$

in the frequency regime between 1-10^4 Hz.

(*A*)

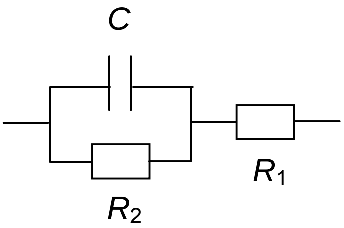

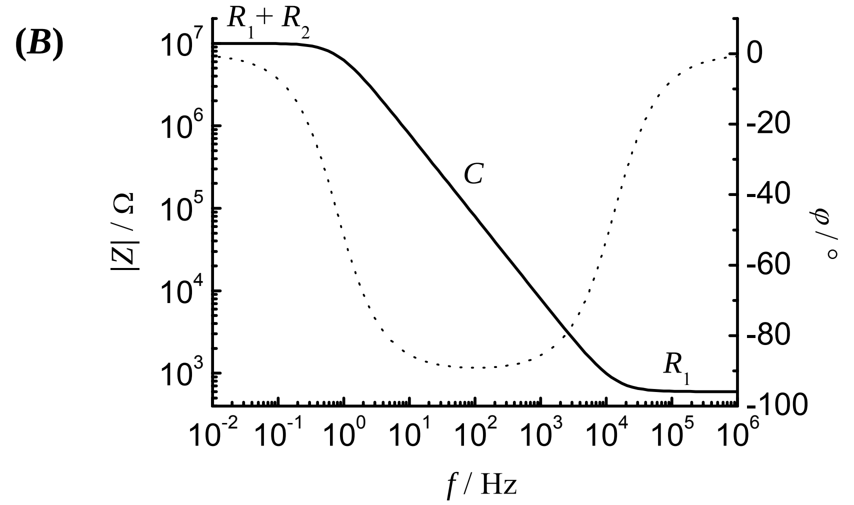

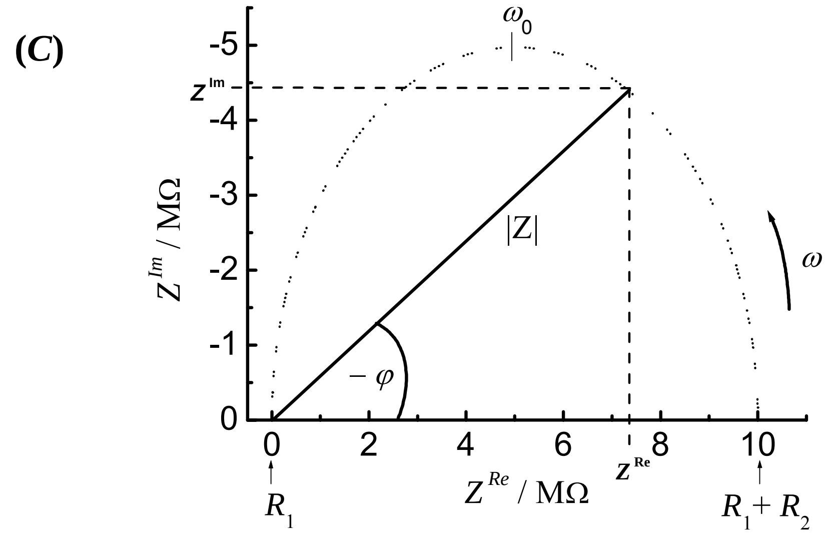

FIGURE 5: (*A*) Electrical circuit composed of a parallel *RC*-element (R_2 and *C*) in series to an Ohmic resistance R_1. R_1 = 600 Ω; R_2 = 10 MΩ; *C* = 1 μF/cm^2. (*B*) Bode Plot and (*C*) Nyquist Plot for the electrochemical system, presented in (*A*).

The Nyquist plot (Fig. 5*C*) displays the real part of the impedance Z^{Re} along the abscissa and the imaginary part Z^{Im} along the ordinate for different values of ω. The course of the frequency from high to low frequencies is indicated by the direction of the arrow. Fig. 5*C* shows a semi-ellipse typical for the selected electrical circuit. The parameters R_1, R_2 and *C* can be determined from the diagram. The semi-ellipse touches with its leftmost end the real axis in R_1 at large frequencies, whereas its rightmost end touches the real axis in $R_1 + R_2$ at low frequencies ($\omega \rightarrow 0$) [97, 99]. The minimum of the imaginary component, corresponding to the top of the semicircle ($\omega_{0;\ \varphi = \max}$), can be used to calculate the capacitance C with

$$\omega_0 = \frac{1}{R_2 C}, \qquad \textbf{(Eq-12)}$$

if R_2 is known.

3.1.2.5 Equivalent circuits modeling

Impedance data can be fitted with an equivalent circuit comprising circuit elements, that are related to the physical processes of the system under investigation. In many cases, ideal circuit elements, such as resistors and capacitors can be applied. Mostly, however, distributed circuit elements are required in addition to the ideal circuit elements to describe the impedance response of a real system adequately. Two of the most important limitations are geometrical restrictions due to the finite size of the system and structural inhomogeneities. Typical circuit elements that are used in equivalent circuits for the evaluation of impedance data are summarized in Table 1.

TABLE 1: Summary of different discrete and distributed elements used in the equivalent circuit analysis of biological impedance data.

circuit element	**symbol**	**impedance $Z(\omega)$**	**phase shift $\varphi(\omega)$**
ohmic resistor	R	R	0
capacitor	C	$(i\omega C)^{-1}$	$-\ \pi/2$
inductor	L	$i\omega L$	$+\ \pi/2$
constant phase element	CPE	$A^{-1}(i\omega)^{-n}$	$-n\ \pi/2;\ 0\ \leq n \leq 1$
Warburg impedance	σ	$\sigma(1\text{-}i)\omega^{-1/2}$	frequency dependent

The procedure of an EIS experiment can be described by the flow diagram shown in Fig. 6 [100]. The EIS measurement of the system under study is accompanied by theoretical considerations on an appropriate physical model of the system. From the physical model an equivalent circuit is derived, which is fitted to the measured impedance spectrum [19]. Because EIS generates detailed information, sophisticated approaches are required to interpret the data and extract meaningful results.

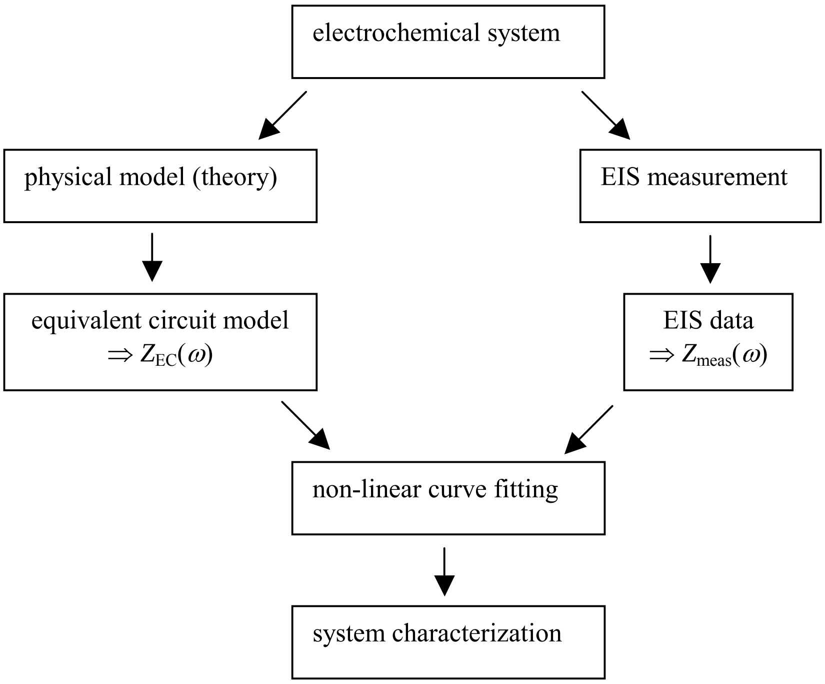
electrochemical system
physical model (theory)
EIS measurement
equivalent circuit model ⇒ $Z_{EC}(\omega)$
EIS data ⇒ $Z_{meas}(\omega)$
non-linear curve fitting
system characterization

FIGURE 6: Flow diagram for the different steps in an EIS experiment.

3.1.2.6 Impedance setup

The core component is the Impedance Gain/Phase Analyzer SI 1260 combined with the 1296 Dielectric Interface (Solartron Instruments, Farnborough, UK) controlled by a personal computer via an interface. The absolute values of the impedance $|Z(\omega)|$ and phase angle $\varphi(\omega)$ between voltage and current were recorded within a frequency range of 10^{-2}-10^{6} Hz, with equally spaced data points on a logarithmic scale and with five data points per decade. All data were obtained at zero offset potential applying a small sinusoidal AC voltage of 30 mV. At low frequencies ($f < 1$ Hz) accurate measurements were possible up to 20 GΩ.

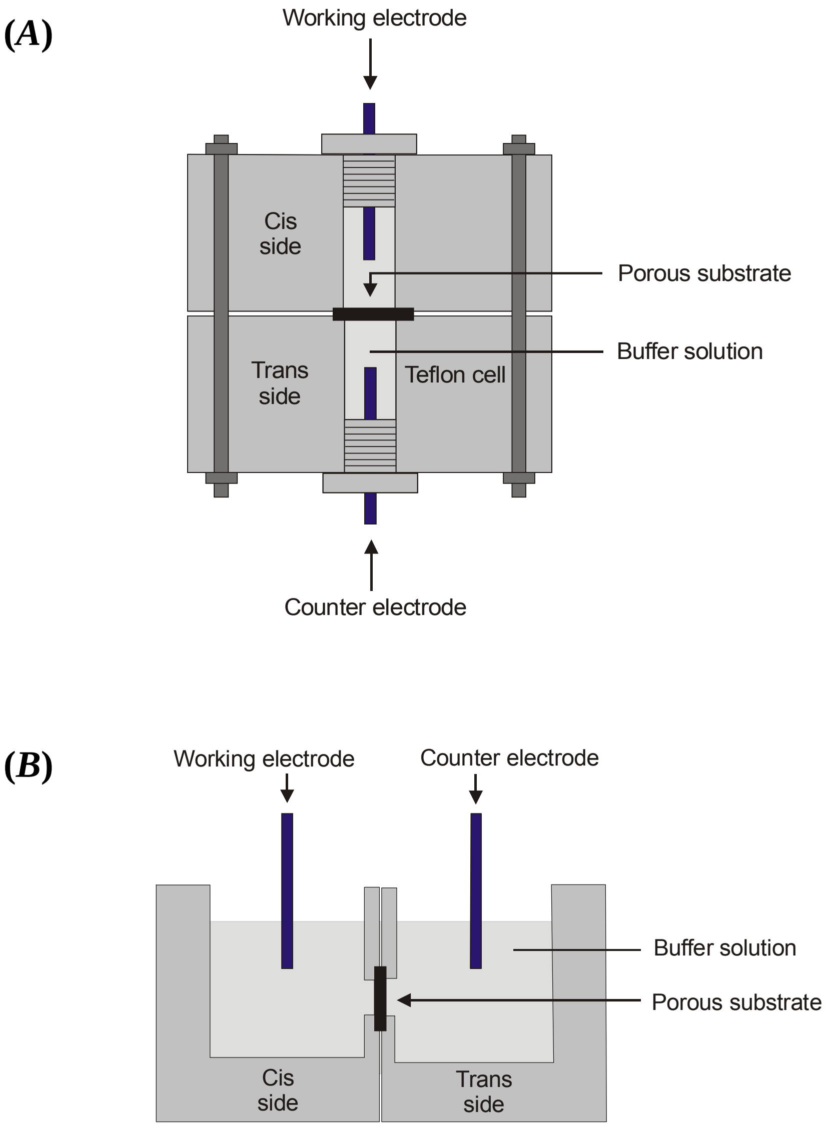
(A)
Working electrode
Cis side
Porous substrate
Buffer solution
Trans side
Teflon cell
Counter electrode
(B)
Working electrode
Counter electrode
Buffer solution
Porous substrate
Cis side
Trans side

FIGURE 7: (*A*/*B*) Schematic drawings of two different Teflon cells used for impedance analysis and single channel recordings. In (*A*) the porous substrate is placed horizontally into the cell, while in (*B*) it is positioned vertically. The volume of a compartment is 2 ml in (*A*) and 6 ml in (*B*). Ag/AgCl as well as platinized platinum wires were used as electrodes for electrochemical measurements.

EIS measurements were carried out using two different Teflon cells as schematically depicted in Fig. 7. The cells consist of two identical compartments separated by the porous substrate with an area of $A = 7\ \mathrm{mm}^2$ sealed by an O-ring. Platinized platinum and Ag/AgCl wires, respectively, immersed in the electrolyte solution on both sides, are connected to the impedance analyzer and serve as working (*cis* compartment) and counter electrode (*trans* compartment). No significant differences in impedance spectra using those two types of electrodes were observed in the frequency range. Electrochemical impedance measurements were performed in 0.1 M Na_2SO_4, 0.5 M KCl and buffer solutions, respectively.

Impedance data were recorded with the Solartron Impedance Measurement Software (Version 3.5.0) and analyzed using the software package Zview 2.6b with Calc-Modulus data weighting.

3.1.3 Fluorescence intensity recordings

The diffusion of the water-soluble, membrane-impermeable fluorescent dye 5,6-carboxyfluorescein (CF) through the porous alumina substrate was followed before and after the formation of lipid membranes by means of fluorescence intensity recordings. For the experiments, porous alumina substrates with pore sizes of 280 nm were vertically mounted into the Teflon cell separating two aqueous compartments (Fig. 7*B*). Carboxyfluorescein was added to the buffer solution (10 mM Tris/HCl, pH 7.0) of the *cis* compartment from an aqueous stock solution leading to a final concentration of 2 mM. Both compartments were softly stirred to accelerate the diffusion of CF through, on the one hand, the membrane-suspended porous alumina substrate and on the other hand, through the porous substrate without a lipid bilayer. The increase in fluorescence in the *trans* compartment that is proportional to the amount of CF diffused from the *cis* to the *trans* compartment was monitored using an Aminco-Bowman Series 2 luminescence spectrometer from SLM-Aminco (Rochester/NY, USA) equipped with a continuous wave 150 W xenon lamp at excitation and emission wavelengths of 495 and 515 nm, respectively.

3.1.4 Single channel recordings

3.1.4.1 Principle of voltage-clamping

The voltage-clamp technique was first invented by Marmont and Cole (1949) and greatly developed by Hodgkin and Huxley in 1952. The basis of the voltage-clamp may be understood by considering the simplified equivalent circuit of a cell membrane shown in Fig. 8.

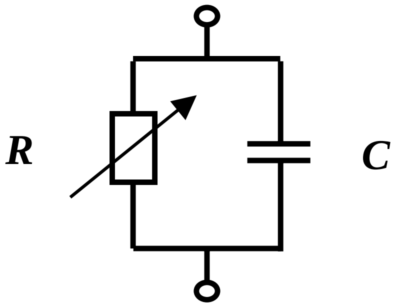

FIGURE 8: Electrical analogue of the cell membrane.

C displays the membrane capacitance while the channels that allow ionic current I_i to flow through the membrane are represented by the variable resistor *R*. The current I_m flowing through the circuit will be the sum of the ionic current I_i and a capacitive current I_c:

$$I_m = I_i + I_c. \qquad \textbf{(Eq-13)}$$

The capacitive current is defined as:

$$I_c = C_m \frac{dV}{dt}. \qquad \textbf{(Eq-14)}$$

In voltage-clamp experiments the voltage is usually forced to change in a square step fashion, being changed as rapidly as possible from one level to another. Under these conditions, short spikes of capacitive current flow at the edges of the pulse, but when the voltage is constant, d*V*/d*t* is zero and thus, the capacitive current I_c is zero.

3.1.4.2 Current measurement circuitry

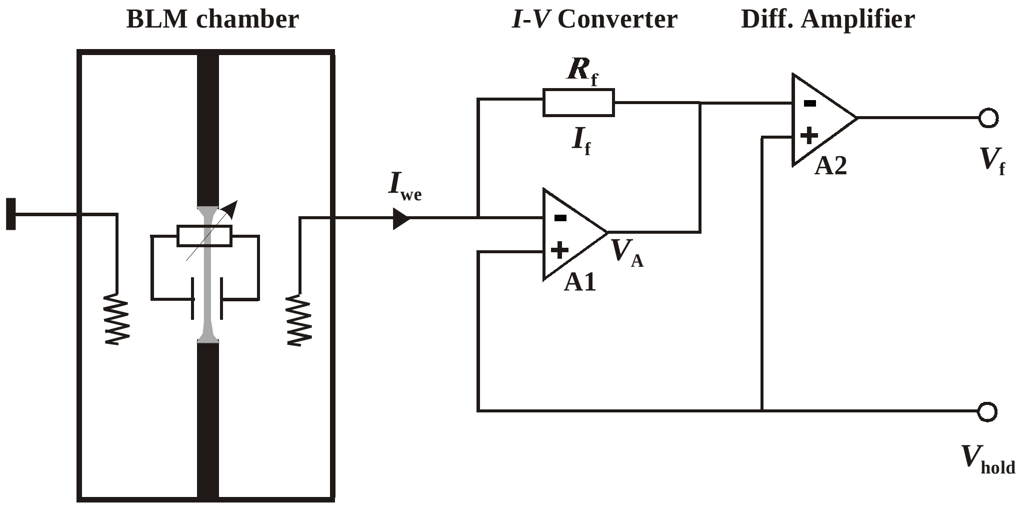

FIGURE 9: Simplified electrical circuit of the headstage as used in a voltage-clamp experiment.

Fig. 9 shows one possible arrangement for a voltage-clamp experiment. The crucial first component is the headstage, a sensitive current-to-voltage converter that receives its input directly from the working electrode, converting small (picoampere to nanoampere) currents I_{we} into voltage signals. The most important property of an *I*-*V* converter for single channel recordings is its ultra low noise level. It is important to maintain this low noise level in the converter´s circuitry because there are many types of channels whose currents are near the limit of resolution of the recording system.

In the commonly used type of headstage, as shown in Fig. 9, an operational amplifier (A1) in a closed loop inverting configuration is used with a high resistive feedback element. The resistor R_f is used to feed part of the output signal back to the input of the operational amplifier.

The working electrode is connected to the inverting and the command voltage V_{hold} to the non-inverting input. The amplifier A1 passes current through its feedback resistor R_f to make the voltage of the inverting input (V_-) the same as V_{hold}. The output voltage of the operational amplifier V_A changes in response to differences in the voltages V_+ and V_- at the inputs according to:

$$V_A = A\,(V_+ - V_-). \qquad \textbf{(Eq-15)}$$

A few microvolts potential difference between the inputs of A1 is sufficient to cause the output to change by several volts, which means that the proportionality constant (or open loop gain) A is very large, typically in the order of 10^7.

An ideal operational amplifier has a very high input impedance (> 10^{12} Ω) and thus, the following equation holds:

$$-I_{\mathrm{we}} = I_{\mathrm{f}} = \frac{(V_{\mathrm{A}} - V_{\mathrm{hold}})}{R_{\mathrm{f}}} = \frac{V_{\mathrm{f}}}{R_{\mathrm{f}}} \, . \qquad \textbf{(Eq-16)}$$

The differential amplifier A2 (resistors omitted) subtracts V_{hold} from the output voltage V_{A} of the current-to-voltage amplifier A1 leading to the voltage $V_{\mathrm{f}} = I_{\mathrm{f}} R_{\mathrm{f}}$. V_{f} is proportional to I_{f} and hence, I_{we} can be calculated from the obtained voltage V_{f}.

For single channel recordings, R_{f} is usually fixed to a large value such as 10 GΩ to obtain a large output voltage V_{A}. There is inevitably some stray capacitance C_{f} associated with the feedback resistor, usually around 0.1 pF. A change in current through R_{f} will thus produce an exponential change in V_{A} with a time constant τ equal to $R_{\mathrm{f}}C_{\mathrm{f}}$, limiting the time resolution of the *I*-*V* converter. The frequency response correction circuit (boost circuit) compensates for time constants τ up to 2.5 ms and extends the bandwidth to 10 kHz [61, 63-65, 101, 102]. Subsequent amplifiers following the headstage are used to scale the gain and remove voltage offsets.

3.1.4.3 Channel recording setup

Single channel recordings were carried out in both Teflon cells depicted in Figs. 7*A*/*B*, equipped with two Ag/AgCl electrodes in the *cis* and *trans* compartment, which were connected to an Axopatch 200B patch-clamp amplifier (Axon Instruments, Forster City, CA, USA) in resistive feedback configuration. The *trans* compartment was connected to ground and all potentials in the *cis* compartment are given relative to ground. Data were filtered with a lowpass cutoff filter of 1 kHz. The analog output signal was digitized by an A/D converter (Digidata 1322A, Axon Instruments). Currents were recorded at room temperature using pClamp 8.0 software (Axon Instruments) with a sampling rate of 5 kHz, while applying holding potentials V_{hold} ranging between -150 and +150 mV. To avoid electrostatic interference during measurements, the electrochemical cell was placed in a Faraday cage set on a mechanically isolated support [61].

Channel recordings of gramicidin

Gramicidin single channel experiments were performed in symmetrical non-buffered solutions of 0.5 M KCl, LiCl and CsCl. Gramicidin D monomers were incorporated into the lipid bilayer by adding the peptide dissolved in ethanol (10^{-6} M) to the electrolyte solution on both sides resulting in a nominal peptide concentration of approximately 10^{-8} M.

Channel recordings of synthetic Vpu$_{1\text{-}32}$

Vpu channel recordings were carried out in symmetrical buffer solutions composed of 5 mM Hepes, 0.5 M KCl (pH 7.4). After formation of stable lipid bilayers, Vpu$_{1\text{-}32}$ was added to the *cis* compartment from a 10^{-6} M stock solution in trifluoroethanol (TFE) leading to a final concentration of approximately 10^{-9} M.

Channel recordings of alamethicin

Alamethicin channel recordings were conducted in symmetrical non-buffered 0.5 M KCl solutions. Alamethicin monomers were added to the *cis* side of the membrane after bilayer formation from a 10^{-5} M stock solution in ethanol leading to a final concentration of approximately 10^{-7} M.

3.2 Preparative methods

3.2.1 Fabrication of porous substrates

Electrochemically grown pores in metals and semiconductors have been studied for about 50 years now [103]. However, only in the last 10 years, intense research efforts have resulted in preparing ordered arrays of pores with pore diameters varying from a few nanometers to some tens of micrometers. Basically two conditions must be fulfilled for electrochemical pore growth: the pore walls must be passivated against dissolution and the pore tips must be in a condition that promotes dissolution [104].

3.2.1.1 Porous alumina

For more than 40 years, porous oxide growth on aluminum under anodic bias in various electrolytes has been subject of investigations [103, 105-107]. Porous alumina exhibits a homogeneous morphology of parallel pores, which grow perpendicular to the surface with a narrow distribution of pore diameters and interpore spacings [108].

The surface of aluminum is occupied with a thin native oxide layer by exposure to air or in aqueous media. This oxide layer emerges due to the following reaction:

$$2\ Al + 3\ H_2O \rightarrow Al_2O_3 + 3\ H_2, \qquad \Delta G^0 = -864.6\ kJ/mol. \qquad \textbf{(R-1)}$$

Since the reactants get separated by the growing aluminum oxide layer, the reaction stops at a certain oxide thickness (passivation). The charge transport through the oxide layer can be maintained by applying a potential to the aluminum.

Anodization of aluminum in acidic electrolytes

Anodization of aluminum in acidic electrolytes is governed by the drift of anions and cations in the applied electric field through the already formed oxide layer and the reactions at the two interfaces: at the oxide/electrolyte interface, protons are reduced and at the metal/oxide interface Al is oxidized to Al^{3+}, which either reacts on site with O^{2-}/OH^- ions to Al_2O_3 or drifts along the electric field through the oxide layer to the oxide/electrolyte interface, where it is ejected into the electrolyte (Fig. 10). Reaction (R-2) describes the anodic oxidation of aluminum:

$$2\ Al + 3\ H_2O \rightarrow Al_2O_3 + 6\ H^+ + 6\ e^-. \qquad \textbf{(R-2)}$$

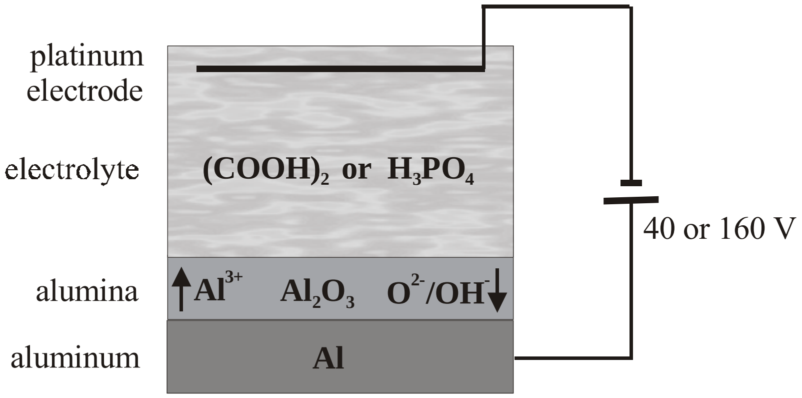

FIGURE 10: Formation of porous alumina by anodization of aluminum in acidic electrolytes that weakly dissolve alumina.

While six electrons per unit Al_2O_3 are injected into the metal, the current flow in solution is carried by released protons. These react with the electrons at the cathode:

$$6\ H^+ + 6\ e^- \rightarrow 3\ H_2\ . \qquad \textbf{(R-3)}$$

The kind of alumina formed under anodic bias depends on the solubility of Al_2O_3 in the electrolyte:

- If the formed alumina is not soluble in the electrolyte, a thin uniform non-porous alumina film will grow rapidly. Its thickness depends only on the applied potential with a growth rate between 1.2-1.4 nm/V [109]. Typical electrolytes for the so called barrier oxide formation are boric, citric or tartaric acid, which have little or no ability to dissolve alumina. Coatings of this type possess unique properties and have been used extensively in electrolytic capacitors and rectifiers.
- If Al_2O_3 is weakly dissolvable in the electrolyte, porous alumina can be formed by anodization. The porous layer thickness is generally a function of current and time according to Faraday´s law, although the final thickness of the aluminum oxide obtained is naturally reduced by dissolution which is most pronounced at and near the outer surface of the oxide layer. Pores are typically formed in sulfuric, chromic, oxalic and phosphoric acid with different pore diameters. The pore depth and diameter depend on different anodization parameters as discussed below [110, 111].

- If Al_2O_3 is moderately dissolvable, electropolishing or pitting occurs. For electropolishing a mixture of perchloric acid and ethanol can be utilized. The oxide is dissolved about as fast as it forms with the result that, at the end of electropolishing treatment, only a very thin oxide film remains. This simultaneous formation and rapid dissolution of oxide smoothes the surface and produces a bright highly reflective surface.
- If Al_2O_3 and aluminum are highly dissolvable in the electrolyte, then the whole bulk aluminum will dissolve [111].

Schematic drawings characterizing the process of pore formation are depicted in Fig. 11. In addition, Fig. 12 shows a typical *I-t* curve recorded during the formation of porous alumina by electrochemical anodization of aluminum in 0.3 M oxalic acid at 2 °C, applying a potential of 40 V. There are essentially four different stages of the pore formation process.

Formation of porous alumina under potentiostatic conditions starts immediately after switching on the anodic bias with the formation of an almost planar barrier oxide up to a thickness determined by the applied voltage at which the oxide becomes insulating against ionic conduction. This first step is accompanied by a large current that rapidly reduces during the formation of the initial barrier oxide (stage 1).

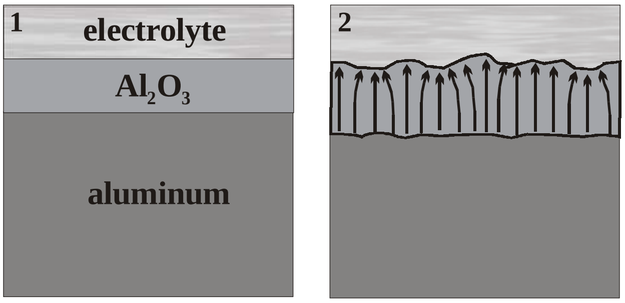

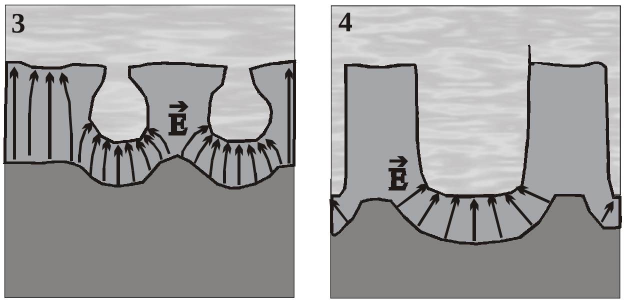

FIGURE 11: Stages of pore growth in anodic alumina [110]: (1) Growth of barrier oxide. (2) Development of pits. (3) Initial pore formation. (4) Pore growth at equilibrium.

If Al_2O_3 is weakly dissolvable, like in oxalic acid, inhomogeneities of the alumina thickness will occur. On locally thinner sites the Al-O bonds will be polarized due to the electric field $\vec{E}$ and field-enhanced dissolution will take place (stage 2). Besides oxide dissolution the increased electrical field enhances the ion drift and thus enables an accelerated oxide growth. As a result, the initially formed pits are not smoothed like in barrier oxide formation, but their growth is enforced. Pores nucleate and start to grow randomly. The increased ion migration results in a current increase (stage 3) until the entire substrate surface is covered with pores limiting each other in horizontal expansion. Further anodization results in propagation of individual paths (′pores′) through the oxide layer. The lateral distribution of the electric field along the pore is inhomogeneous. The maximum field is concentrated at the pore tip and decreases towards the pore walls [110]. Due to competition between the pores, the current starts to decrease until a stable pore growth is eventually reached (stage 4) [108, 110], which is characterized by a balance between field-enhanced oxide dissolution at the oxide/electrolyte interface at the pore bottoms and formation of oxide at the metal/oxide interface due to migration of O^{2-}/OH^- ions through the barrier oxide layer [108, 110].

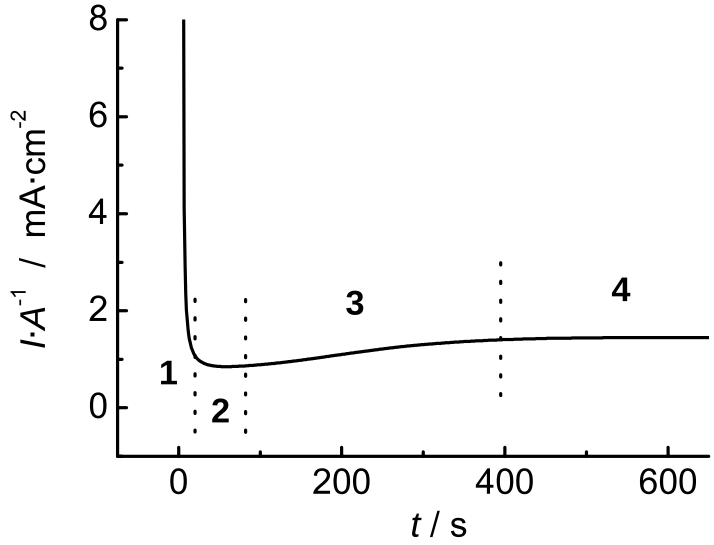

FIGURE 12: Typical *I-t* curve of the electrochemical anodization of aluminum in 0.3 M oxalic acid at 2 °C and an applied potential of 40 V.

Anodization parameters

Porous alumina formation depends on different parameters (anodization voltage, time and temperature) that define the properties of the substrate (pore diameter, pore depth, interpore distance). The interpore distance is defined as center-to-center distance between neighboring pores.

- Anodization voltage: The voltage has a major effect on the pore diameter and the interpore distance, i.e. both are proportional to the applied potential. Nielsch et al. determined a proportionality constant k of 2.5 nm/V [112]. Li et al. were able to vary the interpore distance in porous alumina between 50 and 420 nm [113]. Nielsch et al. calculated pore diameters of 31 nm for porous alumina anodized in 0.3 M oxalic acid applying a potential of 40 V and of 158 nm for porous substrates etched in 0.1 M phosphoric acid while applying 160 V [112].
- Anodization time: The pore depth linearly depends on the anodization time. In case of oxalic acid and an anodization voltage of 40 V, the pore growth is reported to be 1-2 µm/h whereas in case of phosphoric acid and a voltage of 160 V, the pore growth is referred to be 4-5 µm/h [113-115].

- Anodization temperature: A low anodization temperature of 2 °C was chosen in order to achieve low pore growth rates. Low growth rates favor the process of self-organization leading to hexagonally ordered porous alumina.

Formation of hexagonally ordered alumina pores

Although the pores start growing at the upper surface exposed to the electrolyte at almost random positions and have a broad size distribution, nearly perfectly ordered densely packed hexagonal structures can be observed at the bottom of the oxide layer. In 1995, Masuda explained the self-organized arrangement of neighboring pores in ordered hexagonal arrays by a moderate repulsive interaction between the pores during growth which favors energetically the densest package of pores [116]. Mechanical stress due to volume expansion during aluminum oxidation has been proposed by Jessensky and Parkhutik [108, 110] to be the origin of these repulsive forces. The pore density in ordered pore arrays was found to be typically about 20 % lower than at the upper alumina surface, indicating that part of the pores stop growing either shortly after their nucleation or during the self-organization process [108]. The primarily decrease in current in stage 4 of the pore formation process indicates that some initially formed pores stop growing.

For the fabrication of hexagonally ordered pores throughout the entire substrate, a two-step anodization process can be used. Porous alumina formed in the first anodization step is selectively removed by immersion in a 60 °C hot aqueous solution of phosphoric and chromic acid [103]. The remaining texture of the Al surface acts as mask [117, 118]. Due to this prestructured surface, an ordered formation of pores already at the initial stages of the second anodization step is achieved [119].

Dissolution of aluminum

In order to obtain continuously open porous alumina, it is necessary to remove the remaining aluminum from the oxide layer. The samples are either incubated in a saturated $HgCl_2$- or acidulated $CuCl_2$ solution. The aluminum dissolution can be described by the following reactions:

$2\ Al + 3\ HgCl_2 \rightarrow 2\ AlCl_3 + 3\ Hg$ **(R-4)**

$2\ Al + 3\ CuCl_2 \rightarrow 2\ AlCl_3 + 3\ Cu$ **(R-5)**

Pore bottom opening

After dissolution of the remaining aluminum, the lower surface of the alumina substrate is still covered with the initially formed barrier oxide, which can be dissolved by chemical etching in oxalic or phosphoric acid solutions at 30 °C. This etching process also leads to some pore widening [113, 117, 118].

Experimental procedures for formation of porous alumina

Pretreatment of the aluminum samples

High purity aluminum foils (99.999 %; 20 × 20 × 0.5 mm) obtained from Goodfellow were cleaned in acetone and isopropanol. Prior to anodizing, the aluminum foils were annealed under a nitrogen atmosphere at 500 °C for 3 hours to increase the grain boundaries of the polycrystalline aluminum.

Electropolishing

Then, the aluminum foils were electropolished 3 times in a mixture composed of sulphuric acid, phosphoric acid and water (2:2:1, *v/v/v*) at 20 V, 70 °C for 40 seconds in order to reduce the surface roughness [115]. After each step, the samples were thoroughly rinsed with water.

Anodization of aluminum in acidic solutions

The aim was to produce highly ordered porous alumina. For this purpose, the aluminum foils were mounted on a copper plate serving as anode and exposed to the acidic solution in a thermally isolated electrochemical cell. A platinum grid served as cathode. During anodization the electrolyte was vigorously stirred. A detailed description of the etching device is given by Jessensky [114].

Porous structures were obtained by anodizing the electropolished aluminum foils in acidic solutions. Anodization was conducted under constant cell potential using either aqueous oxalic (0.3 M) or phosphoric acid (5 wt %) as electrolyte.

- Highly ordered porous alumina after anodization in phosphoric acid solution

  In the case of phosphoric acid, ordered porous alumina was obtained in a one-step anodization process. Aluminum was anodized at T = 2 °C and V = 160 V for 2 days resulting in ordered pores at the bottom of the porous layer, while the upper surface exhibits a rather non-ordered pore structure.
- Highly ordered porous alumina after anodization in oxalic acid solution

  In the case of oxalic acid as electrolyte, hexagonally ordered pores on both sides of the porous membrane were obtained by a two-step anodization process. First, aluminum was anodized in 0.3 M oxalic acid at T = 2 °C and V = 40 V for 3 hours. Second, the oxide layer was removed by wet chemical etching in a mixture of phosphoric acid (6 wt %) and chromium(VI) oxide (1.8 wt %) at 60 °C for at least 4 hours [113, 117, 118]. The remaining pattern on the aluminum substrate serves as a mask for the second anodization process using the same parameters as in the first step. The anodization is conducted 4 days. Pores that are formed in the second anodization step are hexagonally ordered.

Dissolution of aluminum

After anodization, the remaining aluminum was removed by incubating the substrate in a saturated $HgCl_2$- or acidulated $CuCl_2$-solution at room temperature resulting in a porous alumina membrane with closed pores at the lower surface (pore bottoms).

Pore bottom opening

To remove the barrier oxide layer, the porous membrane was chemically etched at 30 °C in 5 wt % phosphoric or 0.3 M oxalic acid solution. The pore bottom opening was followed time-resolved at room temperature by means of impedance spectroscopy. For this purpose, the porous alumina substrate was mounted into the Teflon cell depicted in Fig. 7*B*.

3.2.1.2 Macroporous silicon

Macroporous silicon has been pioneered in the early 90s by Lehmann and Föll [120]. Macropore formation in silicon is anisotropic and occurs preferentially along the (100)-, (010)- and (001)-directions of single crystalline silicon [121]. Very regular pore arrays with pore diameters of 0.7-3.5 µm and with extremely large aspect ratios (ratio between pore length and pore diameter) have been obtained in the n-Si/HF system after photolithographic prepatterning.

Anodization of n-type silicon of (100)-orientation in hydrofluoric acid

Macropore formation is enabled by silicon dissolution that occurs in hydrofluoric acid under anodic polarizations. The exact dissolution chemistry of n-type silicon is still in question, although it is generally accepted that holes are required in the initial oxidation steps for macropore formation. Holes, which initiate the dissolution process are minority charge carriers in n-type silicon and will always refer to a defect electron. The concentration of holes is very low in n-type silicon at equilibrium. This means that for n-type silicon, significant dissolution occurs only under illumination, high potentials or other hole generating mechanisms.

The dissolution of one silicon atom is induced by two generated holes [120]. Reaction (R-6) describes the anodic oxidation of silicon:

$$\mathrm{Si} + 2\,\mathrm{h}^+ + 6\,\mathrm{F}^- \rightarrow \mathrm{SiF}_6^{2-} + 2\,\mathrm{e}^-, \qquad \textbf{(R-6)}$$

and reaction (R-7) the cathodic reduction of protons to hydrogen:

$$6\,\mathrm{H}^+ + 2\,\mathrm{e}^- \rightarrow \mathrm{H}_2 + 4\,\mathrm{H}^+, \qquad \textbf{(R-7)}$$

leading to the overall reaction [122, 123]:

$$\mathrm{Si} + 2\,\mathrm{h}^+ + 6\,\mathrm{HF} \rightarrow \mathrm{SiF}_6^{2-} + \mathrm{H}_2 + 4\,\mathrm{H}^+. \qquad \textbf{(R-8)}$$

The decomposition of a silicon crystal proceeds preferentially at weakly coordinated sites, such as kink sites (present in steps on the surface or at the intersection of dislocations), where Si atoms have two or three dangling bonds exposed to hydrofluoric acid solution.

Pore initiation and passivation of pore walls

If a polished, illuminated n-type silicon wafer of (100)-orientation is anodized in aqueous HF, the topmost few micrometers of the wafer surface exposed to the electrolyte, are etched homogeneously until tiny etch pits appear, which develop into stable pores. If a silicon atom is removed from an atomically flat surface, an atomic-size dip remains. These small dips in the n-type silicon anode bend the electric field lines in a way that the concave surface regions become more efficient in collecting holes than the convex or flat ones. Since hole transfer from the electrode to the electrolyte dissolves the material, these regions are etched preferentially and the pores start to grow.

The number of etch pits that are formed in the first seconds of anodization on a polished n-type silicon wafer is in the order of 10^{10} cm^{-2}. But only 10^{6} of these etch pits survive and become pore tips [104]. After this initiation and ripening period, pore growth becomes stable and a pattern of randomly distributed pores penetrates the wafer without a further significant change in the number of pores (Fig. 13).

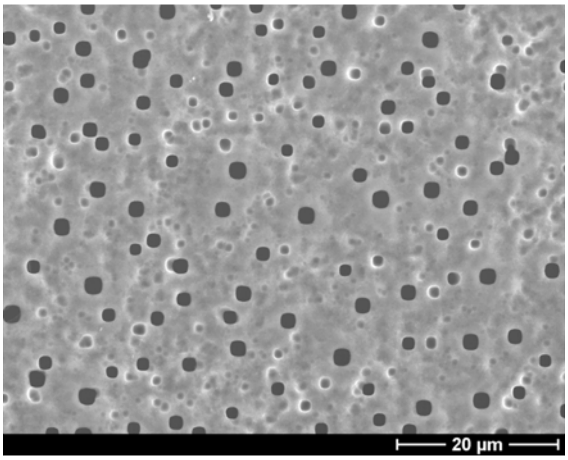

FIGURE 13: Scanning electron microscopy image of the upper surface of a low-doped n-type silicon wafer of (100)-orientation with randomly distributed pores of different pore sizes.

During the anodization process, holes diffuse from the wafer backside to the etch front and are consumed at the pore tips. This promotes the dissolution of the silicon almost exclusively at the pore tips due to the enhanced electrical field in the space charge layer leading to further pore growth perpendicular to the (100)-surface with very high aspect ratio.

The pore walls become depleted of holes and therefore are passivated against dissolution. The silicon remaining between the pores retains its original crystallinity, indicating that pore formation occurs by a direct dissolution of the bulk material, and not by some redeposition or restructuring process.

Highly ordered pore growth in n-type silicon

The understanding of pore growth led to the idea of producing an ordered rather than a random array of pores by using artificial pattern of etch pits formed prior to anodization. Homogeneous pattern of artificial pits can be generated by standard photolithography of an oxide film and subsequent alkaline etching, which leads to well known inverted pyramids, as shown in Fig. 14. Anodization of such a textured wafer leads to a highly ordered array of cylindrical macropores (see below in chapter 4.1.2).

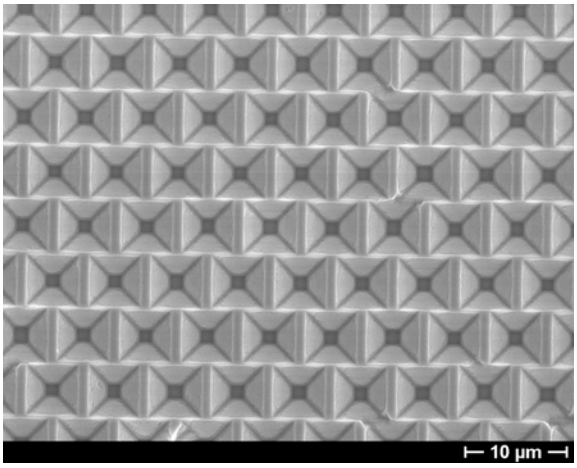

FIGURE 14: Scanning electron microscopy micrograph (top view) of an artificial pattern of etch pits in n-type silicon.

Etch parameters

There exist a lot of parameters, which influence the etch process and thus the properties of porous silicon, e.g. anodization time, applied voltage, photocurrent, masking, doping density, crystal orientation and site of the minority carrier generation. In the following, the most important parameters are explained:

- Anodization time: The pore depth is a linear function of the anodization time. This means that even for differences of one order of magnitude in voltage, current or doping, the average etch rates were found to be around 0.5 µm/min. In order to ensure mechanical stability of the silicon substrate, macroporous silicon with a pore depth of at least 50 µm were etched.
- Photocurrent: The pore diameter is proportional to the square root of the photocurrent that is in turn dependent on the illumination intensity. If the current density is varied during the etching process, the diameter of the pores will vary accordingly. Silicon macropores exhibit pore diameters in the range of 0.7-3.5 µm.
- Masking of the silicon surface: With masking techniques (e.g. photolithography) the pattern of pores is controllable within the limits given by the doping density. A mask with hexagonally ordered pits with a distance of 1.5 µm is frequently used.
- Applied voltage: For low voltages (< 1 V) no pore formation occurs. For higher voltages, pores will grow if minority carriers are available in the bulk silicon.

Dissolution of non-porous silicon by wet chemical etching

A macroporous silicon structure with continuous pores is created by selective dissolution of the non-porous backside ot the silicon wafer. The silicon can be dissolved by an anisotropic etch process in aqueous KOH. The proposed electrochemical reactions are still in question in literature [124]:

$$4\,H_2O + 4\,e^- \rightarrow 4\,OH^- + 2\,H_2 \qquad \text{(reduction)}, \qquad \textbf{(R-9)}$$

$$Si + 2\,OH^- \rightarrow Si(OH)_2^{2+} + 4\,e^- \qquad \text{(oxidation)}, \qquad \textbf{(R-10)}$$

$Si(OH)_2^{2+} + 4\,OH^- \rightarrow SiO_2(OH)_2^{2-} + 2\,H_2O.$ **(R-11)**

These reactions can be summarized to an overall reaction:

$Si + 2\,OH^- + 2\,H_2O \rightarrow SiO_2(OH)_2^{2-} + 2\,H_2.$ **(R-12)**

The KOH etch rate is strongly effected by the crystallographic orientation of the silicon. For silicon of (100)-orientation, the etch rate is reported to be 1-3 µm/min using 20-30 wt % KOH and a temperature of 80-100 °C [125].

Etch stop layers can be used to drastically slow down the etch rate, providing a stopping point of absolute accuracy. SiO_2 is often used as etch stop for KOH. Its Si/SiO_2-selectivity is around 1000/1. The etch rate of SiO_2 in KOH is reported to be 2.0 nm/min.

Experimental procedures for formation of highly ordered macroporous silicon

Hexagonally ordered silicon macropore arrays with pore diameters of 1 µm were produced using photolithography followed by anodization in hydrofluoric acid. The starting material consisted of single crystalline low-doped n-type silicon wafers (doping density < 10^{15} cm^{-3}; phosphorus doped) of (100)-orientation with a resistivity of 0.5 Ω cm and a size of (20 × 20 × 0.35) mm.

Anodization of silicon in hydrofluoric acid

Cylindrical macropores were grown by photo-electrochemical anodization in HF (c_{HF} = 4 wt %; T = 10 °C; V = 2.7 V) starting from prepatterned silicon wafers with inverted pyramids acting as initiation spots [126]. The silicon sample was inserted in the anodization cell with its front side exposed to aqueous HF, while the backside was illuminated by radiation from a 100 W tungsten lamp to generate holes in the valence band of silicon. The sample was anodically biased by a transparent backside Ohmic contact. A platinum wire immersed in the HF solution served as cathode. The solution was stirred slightly during anodization to remove hydrogen bubbles from the sample surface. A detailed description of the electrochemical cell is given by Lehmann et al. [120].

Pore bottom opening

A porous silicon structure with continuous open pores is prepared by selective dissolution of the non-porous silicon backside. After the electrochemical anodization process, a protective SiO_2-film of about 30 nm covering the entire silicon structure was formed by thermal oxidation at 800 °C in an oxygen atmosphere for 3 hours. The SiO_2-layer was then selectively removed from the backside of the silicon wafer by HF, and the silicon dissolved by an anisotropic KOH etching process in 25 wt % KOH at $T = 90$ °C. SiO_2 at the pore walls acts as etch stop for KOH. After this procedure, the pore bottoms were still covered with SiO_2, which was eventually removed by a second HF-dip.

3.2.2 Functionalization of porous substrate surfaces

The functionalization of porous surfaces with a gold layer enables the chemisorption of self-assembled monolayers of thiol compounds.

3.2.2.1 Deposition of a thin gold layer

Gold coating of the lower surface of porous alumina was achieved by sputtering titanium (5-10 nm) as an adhesive layer followed by a gold layer (25 and 40 nm, respectively) using a sputter coater with a thickness control unit (Cressington Sputter Coater 108 auto, Cressington mtm 20, Elektronen-Optik-Service GmbH, Dortmund, Germany). The selective functionalization only of the top surface of the pore walls without filling the pore interior, was ensured by vertical deposition of the metal layers. The thickness of the titanium and gold layers, respectively was properly adjusted according to the pore size, also to ensure that the pores are not filled with metal. The lower surface of the macroporous silicon substrate was coated with a 100 nm gold layer without titanium as adhesive layer.

3.2.2.2 Self-assembled monolayers on gold-covered porous substrates

The gold-coated porous surfaces were functionalized by incubating the porous alumina or silicon substrates in a 1 mM ethanolic solution of either 1,2-dipalmitoyl-*sn*-glycero-3-phosphothioethanol (DPPTE) or 1-octadecanethiol (ODT) at room temperature for at least 12 hours, which renders the gold-coated surface hydrophobic. Before use, the functionalized substrates were thoroughly rinsed with ethanol and dried under a stream of nitrogen.

In order to perform vesicle spreading experiments via electrostatic attractions, gold-covered porous alumina substrates were incubated in either a 1 mM ethanolic solution of 11-mercapto-undecanoic acid (MUDA) or a 1 mM aqueous solution of 3-mercapto-propionic acid (MPA) at room temperature for 12 hours and thoroughly rinsed with ethanol and buffer solution before use.

3.2.3 Formation of pore-suspending lipid bilayers by the painting technique

The painting technique, established by Müller and Rudin (1963) [37] for the formation of freestanding black lipid membranes (BLMs) was taken up by Florin and Gaub (1993) [127] for the formation of painted supported lipid membranes (PSMs). A 50 nm thin gold layer was deposited on a prism by thermal evaporation. The gold-covered surface was rendered hydrophobic by chemisorption of a self-assembled monolayer of hexadecylmercaptane (HDM). The PSMs were formed in a self-assembly process from a drop of an organic phospholipid solution on the self-assembled HDM-monolayer covering the gold surface. The thinning out process of the lipid solvent droplet occurs spontaneously and depends sensitively on the nature of the lipid.

3.2.3.1 Formation of nano-BLMs and micro-BLMs

The painting technique was applied to produce pore-suspending lipid bilayers on porous materials. Before the formation of nano-BLMs and micro-BLMs, the surface area surrounding the hole in the Teflon wall was primed with a phospholipid solution. A solution of 1,2-diphytanoyl-*sn*-glycero-3-phosphocholine in pentane (5 % (*wt*/*v*)) was applied to the orifice and then dried in a stream of nitrogen. Then, the substrate was either horizontally placed in the Teflon cell as depicted in Fig. 7*A* or vertically placed in the cell as presented in Fig. 7*B*. The *cis* and *trans* compartments were filled with electrolyte. 10 µl of a DPhPC solution in *n*-decane (1 % (*wt*/*v*)) were painted over the DPPTE- or ODT-functionalized surface oriented to the *cis* side.

3.2.3.2 Formation of porous matrix-supported BLMs

The surface surrounding the hole in the Teflon wall was preprimed as described in chapter 3.2.3.1. After mounting the porous substrate into the Teflon cell, porous matrix-supported BLMs were prepared on porous alumina and macroporous silicon substrates with pore diameters of 280 nm and 1 µm, respectively. The lower surface of the substrate was not coated with a gold layer and not selectively functionalized. Instead, lipid bilayers were directly prepared by painting 10 µl of DPhPC dissolved in *n*-decane (1 % (*wt*/*v*)) across the lower surface of the substrate.

3.2.4 Formation of pore-suspending lipid bilayers by vesicle spreading and fusion

Planar lipid bilayers were formed by successive adhesion, spreading and fusion of large unilamellar vesicles onto porous alumina based on the one hand on the chemisorption of thiol compounds on gold surfaces and on the other hand on electrostatic attractions between positively charged vesicles and negatively charged substrate surfaces.

Vesicle spreading is an alternative method to prepare membrane-like structures on solid supports and was first described by McConnell et al. (1986) on glass supports [128]. When vesicles hit a suitable solid support, they may adsorb and spread to form a lipid bilayer [26, 129-132]. Once attached, the vesicle begins to flatten from the edges towards the center. The outer flattened areas expand and spread, resulting into a partially flattened vesicle. The underlying mechanisms for vesicle spreading are discussed controversially in literature. Jass et al. [26] reported that the vesicle collapses to form two bilayers, one on top of the other, formed as disks of about the same size. The uppermost bilayer moves from the lower one to unoccupied areas on the surface. This movement can occur by two mechanisms, rolling or sliding, in both cases resulting in a single lipid bilayer structure. The sliding/rolling results in temporary accumulation of lipidic material at the edges of a disk. The edge-to-edge contacts between flattened vesicles, stacked membranes or adjacent single bilayer structures are a prerequisite for the fusion to homogeneous bilayers.

3.2.4.1 Formation of pore-suspending lipid bilayers by spreading and fusion of thiolipid-containing vesicles

1,2-Dipalmitoyl-*sn*-glycero-3-phosphothioethanol (DPPTE), 1,2-diphytanoyl-*sn*-glycero-3-phosphocholine (DPhPC), 1,2-dioleoyl-*sn*-glycero-3-phosphocholine (DOPC) and cholesterol were mixed in appropriate molar proportions from stock solutions in chloroform, dried for 1 hour on the bottom of glass tubes by a stream of nitrogen and desiccated under vacuum for 3 hours. Each glass tube contains 1 mg of lipids. Before use, the lipid mixtures were rehydrated at T = 55 °C for 30 minutes by addition of 1 ml buffer solution (10 mM Tris, 100 mM Na_2SO_4, pH 7.4) and vortexed at least 3 times in the meantime leading to a suspension of multilamellar vesicles with a concentration of 1 mg/ml. It was fundamental for all preparation steps to ensure that the temperature is kept above the main phase transition temperature of the lipid mixture. Multilamellar vesicles were converted into large unilamellar vesicles with nominal vesicle diameters of 100 nm by the extrusion method using a miniextruder (LiposoFast ®, Avestin) with Armatis polycarbonate membranes of 100 nm in pore size [133].

Highly ordered porous alumina substrates exhibiting pore diameters of 55 nm and a porosity of 60 % were coated with a thin 25 nm gold layer on the lower surface ensuring a selective functionalization. Vesicle spreading experiments were performed directly in the Teflon cell by incubating the gold-coated lower surface with a vesicle suspension in a final concentration of 0.25 mg/ml at temperatures T from room temperature up to 60 °C.

The vesicles prepared by the extrusion method exhibited diameters around 100 nm exceeding the alumina pore size to ensure that they are excluded from the pores interior. After incubation the substrates were rinsed with buffer solution several times to remove vesicles attached to the lipid bilayer and from solution. Impedance spectra characterizing the lipid bilayer formation were recorded in 10 mM Tris, 100 mM Na_2SO_4 (pH 7.4) in time intervals.

3.2.4.2 Formation of pore-suspending lipid bilayers by spreading and fusion of positively charged DODAB vesicles to negatively charged porous substrate surfaces

Large unilamellar vesicles composed of positively charged *N*,*N*-dioctadecyl-*N*,*N*-dimethyl ammonium bromide (DODAB) were prepared at 55 °C (above the main phase-transition temperature of the lipid) in 10 mM Na_2SO_4, 10 mM Tris/H_2SO_4 (pH 8.6) according to the extrusion method using polycarbonate membranes with a nominal pore diameter of 100 nm (see chapter 3.2.4.1).

The MPA- or MUDA-functionalized porous surface, which was negatively charged at pH 8.6 due to the deprotonated carboxylic acid group exposed to the buffer solution, was incubated with the DODAB vesicle suspension with a final concentration of 0.5 mg/ml for 3 hours at 55 °C. Vesicle spreading and fusion to pore-suspending lipid bilayers was supposed to be promoted by electrostatic attractions between the positively charged vesicle and the negatively charged substrate surface.

4 RESULTS

4.1 Characterization of the porous substrates

Porous alumina and silicon substrates are supposed to be ideally suited as supports for highly insulating lipid bilayers, if they exhibit special desired structural and electrical properties. By means of impedance spectroscopy and scanning electron microscopy the electrical and structural properties of these porous materials were analyzed.

4.1.1 Porous alumina

Porous alumina substrates were produced by anodization either in 0.3 M oxalic or 5 wt % phosphoric acid solution. After anodization of the aluminum foils, porous alumina embedded in aluminum is obtained (Fig. 15*A*). The pore bottoms are completely covered with an oxide layer termed barrier oxide that is formed in the initial stages of the anodization.

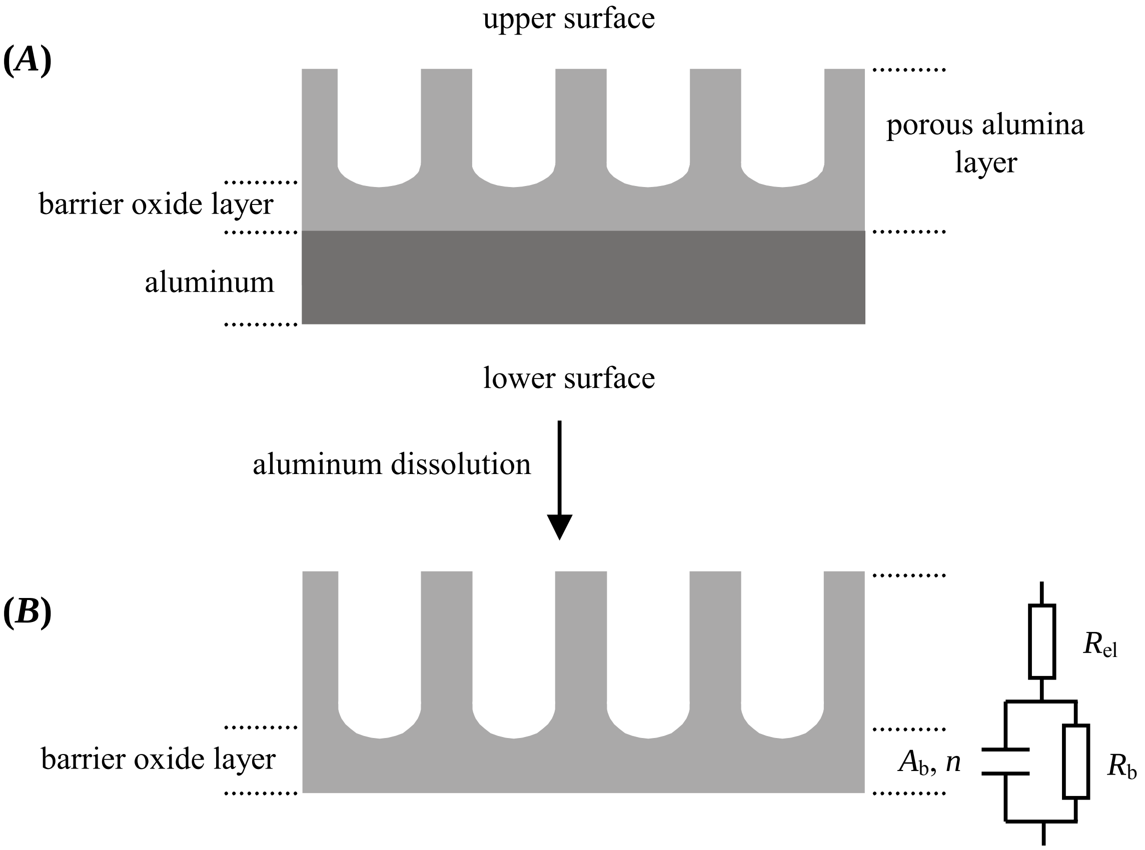
upper surface
(A)
porous alumina layer
barrier oxide layer
aluminum
lower surface
aluminum dissolution
(B)
barrier oxide layer
R_{el}
A_b, n
R_b

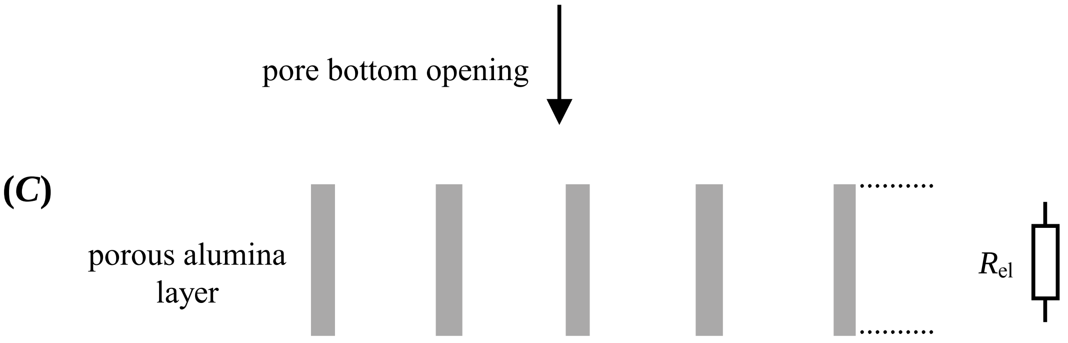

FIGURE 15: Different stages of the formation of sieve-like alumina substrates. (*A*) After anodization. (*B*) After aluminum dissolution. (*C*) After pore bottom opening. In addition, two corresponding equivalent circuits are presented: In (*B*), an equivalent circuit composed of a parallel circuit of a constant phase element (A_b, n) and a resistance R_b representing the barrier oxide layer in series to an Ohmic resistance R_{el} representing the electrolyte solution is depicted. In (*C*), the circuit only consists of a simple Ohmic resistance R_{el}.

To obtain a sieve-like alumina structure, the aluminum has to be removed (Fig. 15*B*). This was achieved by oxidizing and completely dissolving it in either $HgCl_2$- or acidulated $CuCl_2$-solution, which took approximately 20 minutes up to 3 hours. The aluminum dissolution was followed by visual inspection and was assumed to be completed if the porous substrate was free of metallic aluminum. Scanning electron microscopy (SEM) images of the lower surface of the porous alumina clearly demonstrate that dissolution of aluminum in a saturated $HgCl_2$-solution takes longer but is much gentler than dissolution in $CuCl_2$-solution, which is a faster process but may result in a complete decomposition of the substrate.

4.1.1.1 Impedance analysis of the pore opening process of porous alumina

The barrier oxide layer needs to be fully removed to obtain a sieve-like structure, in which all pores are open on both sides (Fig. 15*C*). This is achieved by chemically dissolving alumina in acidic solutions. The opening process was followed by impedance spectroscopy. Two different solutions were used, 0.3 M oxalic acid and 5 wt % phosphoric acid solution. A simplified equivalent circuit representing the entire porous alumina layer is composed of three elements (Fig. 15*B*) [134, 135]: A parallel circuit of a constant phase element (A_b, n) and a resistance R_b representing the electrical behavior of the barrier oxide layer, in series to the resistance of the electrolyte R_{el} representing the electrical behaviour of the water-filled porous structure and the bulk electrolyte [136].

In Fig. 16*A*, typical impedance spectra of a porous alumina substrate obtained by anodization in phosphoric acid solution followed by removing aluminum and the barrier oxide at the lower surface of the pores by oxalic acid treatment are depicted.

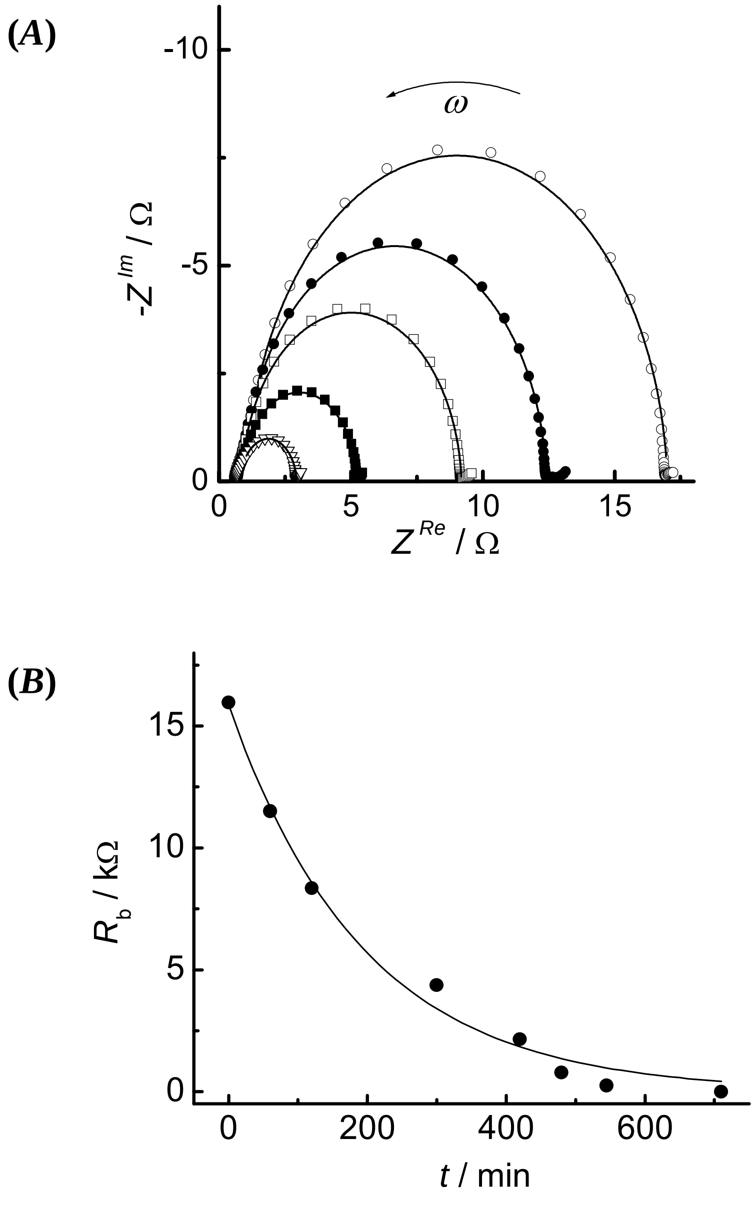

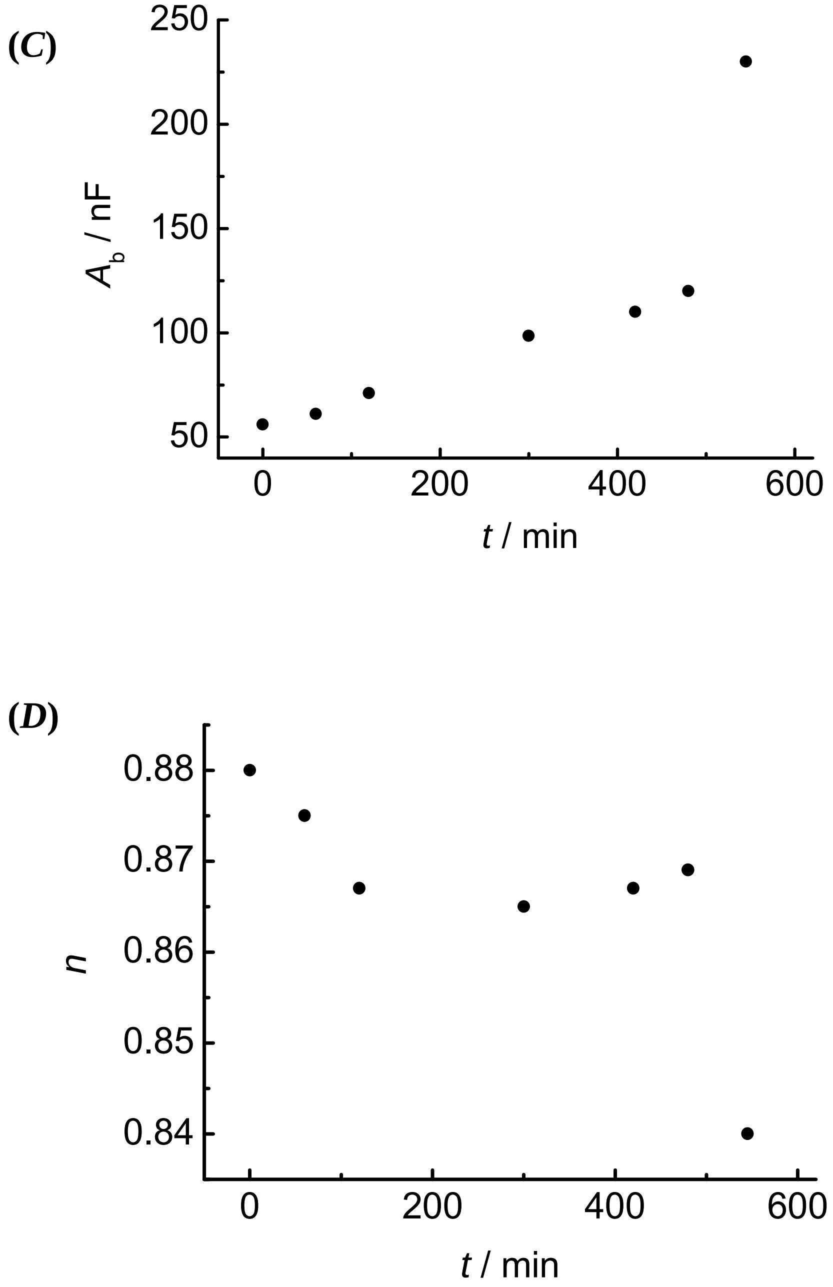

FIGURE 16: (*A*) Impedance spectra in a frequency range of 10^{-1}-10^{6} Hz of a porous alumina substrate obtained by anodization of an aluminum foil in 5 wt % phosphoric acid solution before and after several time periods in 0.3 M oxalic acid solution: (○) 0 min, (●) 60 min, (□) 120 min, (■) 300 min, and (∇) 420 min. The solid lines are the results of the fitting procedure with the equivalent circuit shown in Fig. 15*B*. The electrical parameters R_b, A_b, n were extracted from impedance data of the pore opening process. (*B*) Time course of the resistance R_b which empirically follows a monoexponential decay (solid line) with a decay time τ of (195 ± 14) min. (*C*) Time course of the constant phase element A_b. (*D*) Time course of n.

The impedance spectra are characterized by a typical semi-ellipse and can be modeled by the equivalent circuit depicted in Fig. 15*B*. Fitting the parameters of the equivalent circuit to the data results in very good agreement between data and fit. R_b, A_b and n can be readily extracted from the time-resolved impedance spectra. While incubating the porous alumina membrane in the acidic solution, R_b considerably decreases (Fig. 16*B*) indicating a decrease in barrier oxide thickness at the lower surface. The time course empirically follows a monoexponential decay with a decay time τ of (195 ± 14) min. During the dissolution process, A_b increases starting from a value of 56 nF until it disappears at the end of dissolution when all pores are open. The time course of the constant phase element A_b is displayed in Fig. 16*C*. For n, a slight decrease is observed from 0.88 to 0.84 (Fig. 16*D*), which is still close to 1 implying that the parameter A_b can, as a first approximation, be viewed as the capacitive behavior of the barrier oxide layer. After (710 ± 150) min the electrical parameters of the barrier oxide layer, R_b and A_b, cannot be detected anymore indicative of its complete dissolution. The impedance spectrum is only characterized by the Ohmic resistance R_{el} of the electrolyte in the pores and the bulk electrolyte (Fig. 15*C*) and the capacitance of the platinized platinum counter electrode, which becomes discernable at low frequencies. The fact that only the resistance of the bulk electrolyte is detected by impedance analysis shows that the current solely flows through the pores, while the alumina columns are not detected by impedance spectroscopy. Thus, by impedance spectroscopy it is possible to determine whether all pores are open or not.

The time period till the barrier oxide layer is completely dissolved depends on the porous alumina type and the used acidic solution. Removal of the barrier oxide layer of porous alumina obtained from anodizing in phosphoric acid solution exhibits a decay time τ of (23 ± 4) min in phosphoric acid and of (195 ± 14) min in oxalic acid solution, while τ is (2.2 ± 0.3) min in phosphoric acid and (95 ± 17) min in oxalic acid solution when starting with porous membranes that were anodized in oxalic acid solution. The decay time τ of the monoexponential decay and the corresponding time periods required for completely opening of the pores are summarized in Table 2.

TABLE 2: Decay times τ and time periods of pore bottom opening of porous alumina in different acidic solutions.

etch process **pore bottom opening**	**τ / min**	**time period */ min**
oxalic acid oxalic acid	95 ± 17	340 ±70
oxalic acid phosphoric acid	2.2 ± 0.3	14 ± 3
phosphoric acid phosphoric acid	23 ± 4	60 ± 12
phosphoric acid oxalic acid	195 ± 14	710 ± 150

*) The time period is defined as the time until the impedance spectrum only shows the electrolyte resistance indicating that all pore bottoms are dissolved.

From the obtained data, it was concluded that the most convenient and time-saving method is to anodize aluminum in 5 wt % phosphoric acid solution followed by aluminum dissolution in saturated $HgCl_2$ followed by pore bottom opening again in 5 wt % phosphoric acid solution.

4.1.1.2 Characterization of porous alumina by scanning electron microscopy

As oxalic and phosphoric acid dissolve aluminum oxide in general, the barrier oxide layer at the lower surface is not selectively dissolved and as a result the procedure also leads to a widening of the pores. Thus, scanning electron microscopy was performed to fully characterize the substrates.

Two scanning electron microscopy images of the lower surface of different porous alumina substrates and one side view after a thin gold layer was sputtered on the surface are shown in Fig. 17. Porous alumina substrates obtained after 48 hours of anodization in phosphoric acid solution followed by aluminum dissolution in saturated $HgCl_2$ and pore bottom opening in phosphoric acid solution exhibit a mean pore size distribution of (280 ± 45) nm and a thickness of (195 ± 30) μm (Fig. 17*A*), which translates to a pore growth rate of 4-5 μm/h. Hence, the pore size is increased from (150 ± 25) nm, extracted from scanning electron microscopy images before pore bottom opening, by (130 ± 20) nm due to the pore bottom opening process.

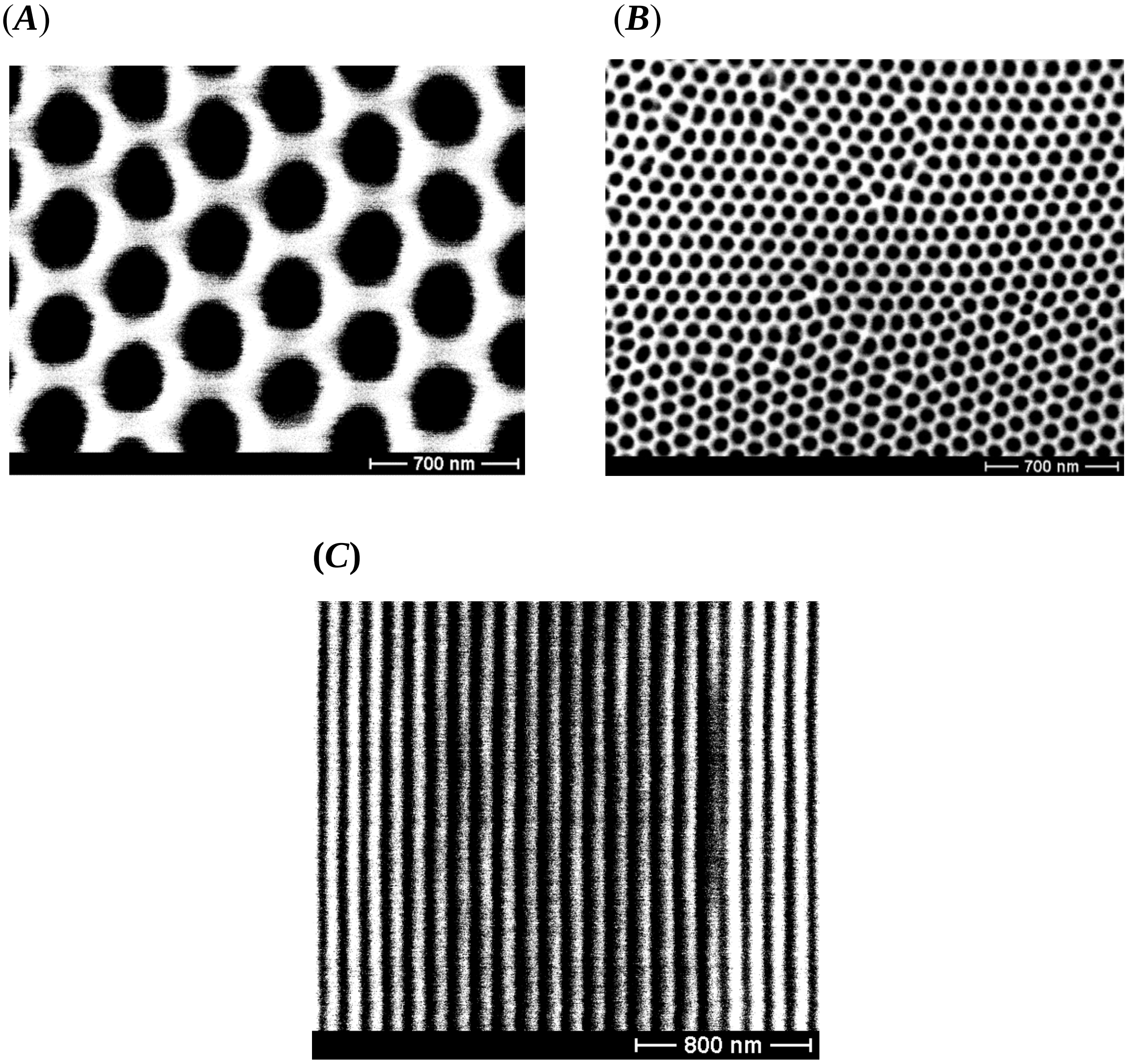

FIGURE 17: SEM micrographs (two bottom views and one side view) of highly ordered porous alumina layers anodized under different conditions. Anodization was conducted (*A*) in 5 wt % phosphoric acid at T = 2 °C and V = 160 V and (*B*) in 0.3 M oxalic acid at T = 2 °C and V = 40 V. The determined pore diameters are (*A*) (280 ± 45) nm and (*B*) (55 ± 8) nm. (*C*) Side view of hexagonally ordered porous alumina etched in 0.3 M oxalic acid solution.

A surface porosity of (33 ± 4) % was calculated by pixel analysis from the SEM images, which is in good agreement with the results of Gösele and coworkers [112, 113, 117, 118].

Porous alumina obtained by anodizing in oxalic acid solution for 96 hours followed by aluminum dissolution in saturated $HgCl_2$ and pore bottom opening in phosphoric acid solution leads to a pore size distribution of (55 ± 8) nm, a thickness of (150 ± 20) µm and a surface porosity of (60 ± 8) % (Fig. 17*B*). The growth rate is calculated to be 1-2 µm/h. In Fig. 17*C*, the side view of a hexagonally ordered porous alumina substrate after anodization in oxalic acid solution is shown. It is obvious that the pores grow homogeneously perpendicular to the surface and form almost perfect cylinders.

4.1.2 Macroporous silicon

As for porous alumina, the suitability of macroporous silicon substrates as supports for lipid bilayers was analyzed.

4.1.2.1 Electrochemical characterization of macroporous silicon

Highly ordered silicon macropore arrays with pore diameters of 1 µm were produced using photolithography followed by anodization in hydrofluoric acid [124]. After the etch process, the porous silicon structure was still covered with a non-porous silicon layer at the lower surface of the wafer, which is removed by anisotropic dissolution in KOH. As the preparation of macroporous silicon substrates was completely conducted at the MPI of Microstructure Physics in Halle (Saale), no impedance recordings of the pore bottom opening process were performed.

However, the electrochemical characteristics of continuously open porous silicon substrates with and without gold-coverage were investigated by means of impedance spectroscopy. In both cases - without and with a 100 nm thin gold layer on the lower surface of the porous matrix - only the Ohmic resistance of the electrolyte R_{el} was detected, which indicates that the current solely flows through the pores as already observed for sieve-like porous alumina substrates. The functionalization of the lower surface with gold did not change the electrochemical behavior of the substrate.

4.1.2.2 Characterization of macroporous silicon by scanning electron microscopy

Scanning electron microscopy (SEM) images of the upper and lower surface as well as a side view of the prepared porous silicon substrates were taken (Fig. 18). Fig. 18*A* shows the upper surface after electrochemical etching with square-shaped pores with an etch length of around 1.0-1.2 µm. The lower surface of the macroporous silicon substrate (Fig. 18*B*) with a 100 nm gold layer exhibits pores with diameters of (1.0 ± 0.1) µm. In contrast to the initial square-shaped photolithographically formed pore nuclei at the upper surface of the silicon wafer (Fig. 14), the opened pores at the lower surface are rather circular. The pores are almost perfectly hexagonally ordered. Only very few disorders occur. A typical disorder can be observed in the bottom right corner of the SEM image, marked by an arrow, in Fig. 18*B*, where one single pore is missing. The size of the surrounding pores is partially modified.

A surface porosity of (22 ± 3) % was calculated by pixel analysis from the SEM image. In Fig. 18*C*, an image of the lower surface of macroporous silicon is depicted after incomplete pore bottom opening by the anisotropic KOH etching process. The pores in the upper left quarter are still covered with a thin oxide film.

The side view of a macroporous silicon substrate, where the non-porous lower surface of the silicon substrate has not yet been removed (Fig. 18*D*), reveals that the pores grow perpendicular to the substrate surface. This almost perfect pore growth of each individual pore is not only a consequence of the lithographic pattern, but also of the orientation of the silicon single crystal. Each pore grows with the same velocity, and the thickness of the porous substrate is determined by the anodization time and is typically adjusted between 50-200 µm to ensure mechanical stability of the substrate.

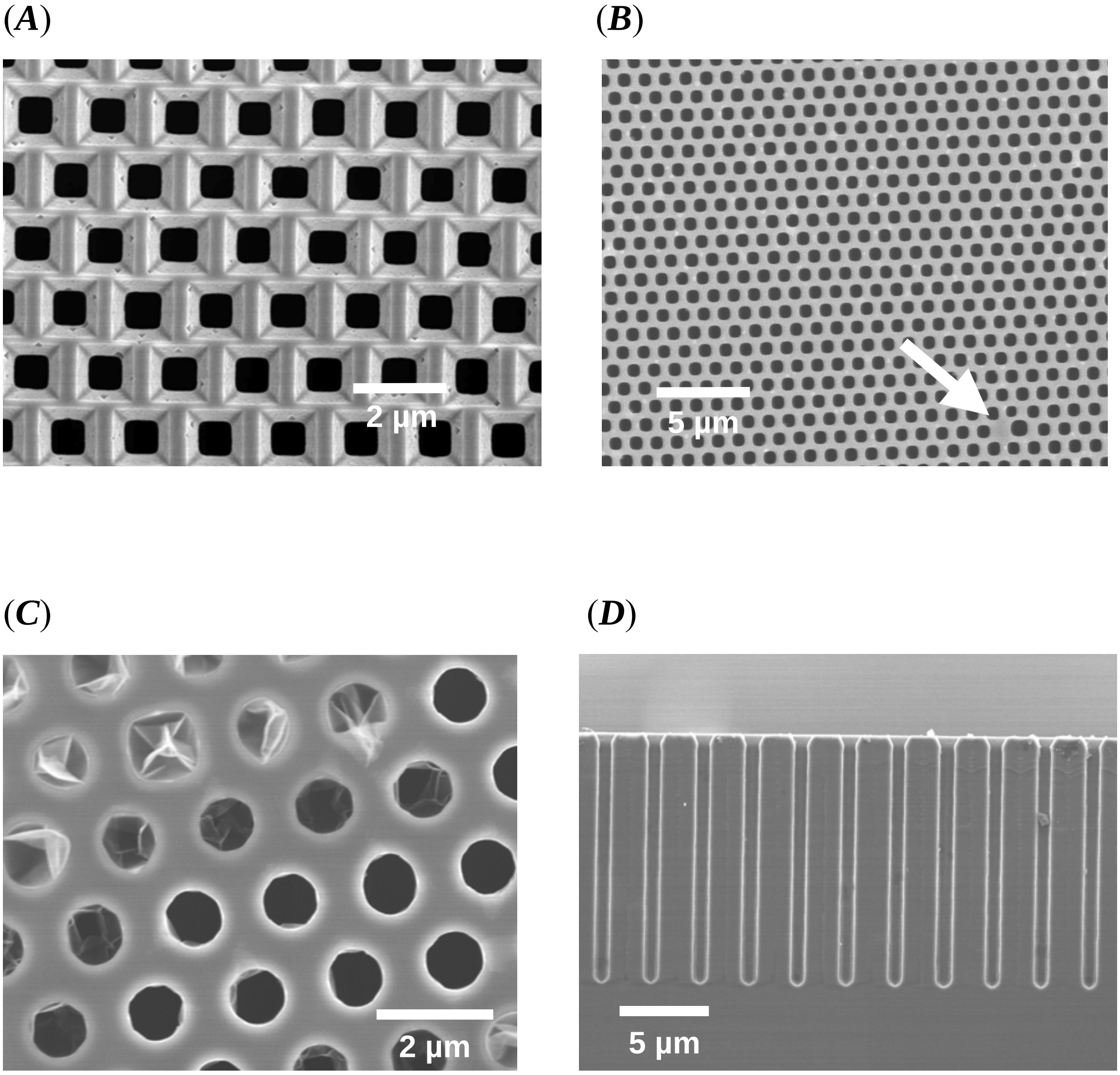

FIGURE 18: Scanning electron microscopy micrographs of hexagonally ordered macroporous silicon substrates are presented in (*A*) top, (*B,C*) bottom and (*D*) side view. Photo-electrochemical etching was conducted in 4 wt % hydrofluoric acid at T = 10 °C and V = 2.7 V. The pore diameter was calculated to be (1.0 ± 0.1) µm with a surface porosity of (22 ± 3) % calculated by pixel analysis. (*C*) After incomplete pore bottom opening, still a few pores are covered with a thin oxide film.

Impedance data as well as scanning electron microscopy images revealed the suitability of porous alumina and silicon substrates as supports for lipid bilayer immobilization. The substrates are electrically inert, smooth and exhibit a hexagonally ordered pore structure with pore diameters in the nano- and micrometer range.

4.2 Formation of pore-suspending lipid bilayers by the painting technique

4.2.1 Formation and stability of nano-BLMs based on porous alumina

Porous alumina substrates with pore diameters of 55 and 280 nm were available as supports for lipid bilayer deposition. The formation of highly insulating pore-suspending lipid bilayers suited for single channel recordings was demonstrated using both porous alumina substrates differing in pore size. Membrane specific parameters such as the membrane capacitance and resistance were extracted from impedance data and exhibited similar values for these two different pore sizes.

In order to explain the membrane formation process in more detail, only porous alumina substrates with pore sizes of 280 nm were chosen for two reasons: The most convenient and time-saving method for the preparation of porous alumina substrates is to anodize aluminum in phosphoric acid solution followed by aluminum dissolution in saturated $HgCl_2$ and pore bottom opening in phosphoric acid solution. Furthermore, it is assumed that the peptide insertion into lipid bilayers suspending pores is facilitated using larger pore diameters. Thus, all bilayer preparations discussed in this chapter are based on porous alumina substrates with pore diameters of 280 nm, though the same results were in principle obtained for porous substrates with pore diameters of 55 nm.

Prior to bilayer deposition, the lower surface of the hexagonally ordered porous alumina substrate was covered with an ultrathin titanium layer (5 nm) as adhesive layer and a thin gold layer (40 nm), which allows for chemisorption of thiol compounds. Either the phospholipid 1,2-dipalmitoyl-*sn*-glycero-3-phosphothioethanol (DPPTE) or the alkanethiol 1-octadecanethiol (ODT) were self-assembled on the gold surface rendering it hydrophobic. After incubation with the thiol compound, the functionalized alumina substrate was investigated by impedance spectroscopy. Impedance analysis revealed that the self-assembled monolayer did not alter the impedance behavior. Only the Ohmic resistance of the electrolyte R_{el} was detected (Fig. 19, ■). This result corroborates that the current only flows through the pores and changes on top of the alumina pore columns cannot be detected. As the resistance R_{el} does not change after monolayer formation it can also be concluded that all pores are still filled with electrolyte even though the surface is more hydrophobic on the functionalized side and that the inner walls of the pores are not covered with gold and a hydrophobic monolayer as that would prevent pore filling with an aqueous solution.

Both thiol compounds form self-assembled monolayers (SAMs) on flat [137] and porous gold-coated surfaces [53, 138]. Since the alkanethiol ODT forms rather rigid and crystalline monolayers, the phospholipid DPPTE was preferred due to its lipidic character in order to create hybrid bilayers better mimicking the properties of cell membranes.

The following membrane preparations were all performed with self-assembled DPPTE-monolayers on gold-covered porous substrates. The phospholipid DPhPC dissolved in *n*-decane was spread on the functionalized porous alumina substrates resulting in a hydrophobic droplet with a thickness of several micrometers.

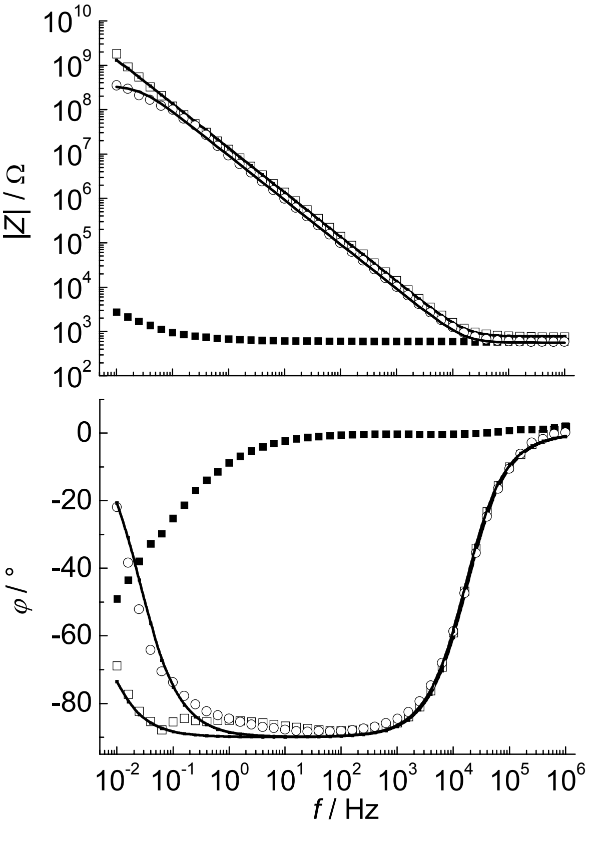

FIGURE 19: Impedance spectra of gold-covered porous alumina substrates functionalized with a DPPTE-monolayer before (■) and after (□, O) spreading of a lipid droplet across the porous alumina substrate. (□) depicts an impedance spectrum obtained 1 day after formation of a nano-BLM, (O) shows an impedance spectrum of a different nano-BLM preparation, 3 days after its formation. The solid lines are the results of the fitting procedure using the equivalent circuit shown in Fig. 20: (□) C_m = 11.7 nF, R_m = 4.7 GΩ; (O) C_m = 17.2 nF, and R_m = 0.35 GΩ.

The formation of pore-suspending lipid bilayers, which we termed nano-BLMs, was followed by means of impedance spectroscopy in a frequency regime of 10^{-2}-10^{6} Hz. In Fig. 19, impedance spectra of functionalized porous alumina substrates before (closed symbols) and after addition (open symbols) of the lipid droplet are shown. Both impedance spectra (□, ○) after addition of the lipid droplet clearly indicate the formation of an insulating layer across the porous matrix. Control experiments, in which porous substrates were not functionalized with a DPPTE-monolayer, revealed that the insulating layer is only formed in the presence of a hydrophobic monolayer. The impedance spectrum (□) was recorded 1 day after formation of the nano-BLM and was used for single channel measurements of gramicidin after impedance analysis (see chapter 4.4.2.1). To extract membrane specific parameters from the impedance data, the simplest equivalent circuit to model the electrical behavior of a lipid bilayer was used, which is depicted in Fig. 20. It is composed of a parallel *RC*-element (R_m and C_m) representing the electrical behavior of a lipid bilayer in series to the Ohmic resistance R_{el} representing the electrolyte solution in the pores and the bulk. The obtained impedance spectrum is characterized by the electrolyte resistance R_{el} in the high frequency regime ($5 \cdot 10^{4}$-10^{6} Hz) and the capacitance C_m at frequencies below $5 \cdot 10^{4}$ Hz. At frequencies below $3 \cdot 10^{-1}$ Hz a second Ohmic resistance is discernable, which is attributed to the membrane resistance R_m. Fitting the parameters of the equivalent circuit shown in Fig. 20 to the data presented in Fig. 19 results in good agreement between data and fit with a membrane capacitance of $C_m = 11.7$ nF and a membrane resistance of $R_m = 4.7$ GΩ.

While for all treated impedance data with this model, C_m is well defined in the spectrum with a fitting error of about 1-3 %, the fit error of R_m depends on its absolute value. For membrane resistances larger than 1 GΩ, the Ohmic resistance is only determined within the frequency range of 10^{-2}-10^{-1} Hz resulting in a fit error of about 20 %, while below 1 GΩ the fit error is less than 12 %. The impedance spectrum (○) in Fig. 19 represents a different membrane preparation and was monitored 3 days after nano-BLM formation. Even after 3 days, the impedance spectrum clearly indicates the existence of an insulating nano-BLM with a membrane capacitance of $C_m = 17.2$ nF and a membrane resistance of $R_m = 0.35$ GΩ. Owing to the lower membrane resistance, the ohmic contribution is readily discernible at frequencies below 1 Hz. For more than fifteen membrane preparations, membrane capacitances with a mean value of (14.9 ± 3.3) nF were obtained.

For the membrane resistance such value cannot be given easily. Though each successful membrane preparation led to the formation of a nano-BLM with the characteristic membrane capacitance, the membrane resistance varied in the range of 10^6-10^{10} Ω. Nano-BLMs with initial membrane resistances exceeding 1 GΩ were evaluated as successful preparations. Taking into account this limitation, one out of six preparations was suited to perform single ion channel recordings.

To calculate an area-related capacitance value, the active area has to be determined. Since the current exclusively flows through the pores, only the porous area must be taken into account. One can roughly estimate the active porous area from the total solution exposed area ($A = 7\ \mathrm{mm}^2$) and the porosity of the porous material. Taking the porosity of 33 % for an alumina substrate anodized in phosphoric acid solution into account, an active area of $A = 2.3\ \mathrm{mm}^2$ is calculated. Thus, the mean capacitance of $C_\mathrm{m} = (14.9 \pm 3.3)$ nF translates into a specific membrane capacitance of $C_\mathrm{m}^\mathrm{A} = (0.65 \pm 0.14)\ \mu\mathrm{F/cm}^2$. C_m^A is defined as $C_\mathrm{m} A^{-1}$. This value agrees well with those obtained for classical black lipid membranes.

From the capacitance and resistance values, it is assumed that single lipid bilayers have been formed across the pores. A scheme of such a self-assembled nano-BLM is presented in Fig. 20:

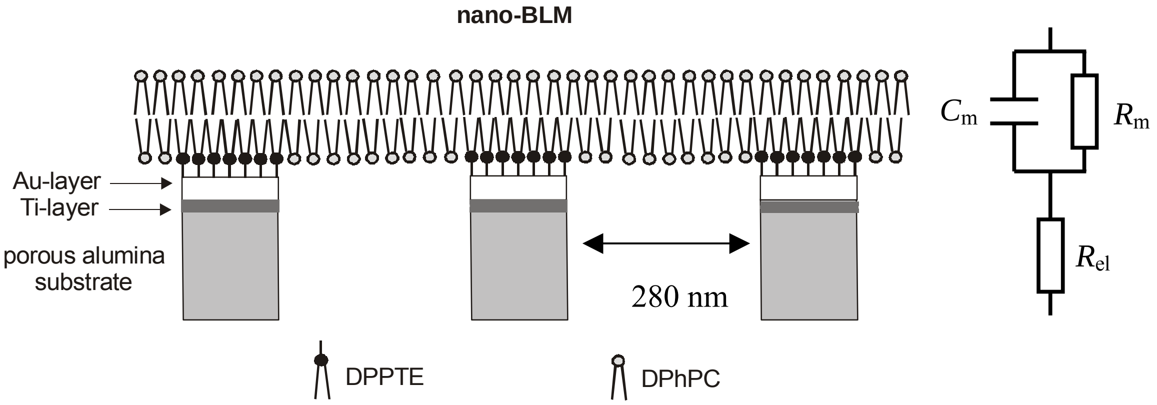

FIGURE 20: Schematic representation of a nano-BLM formed by DPhPC onto a self-assembled DPPTE-monolayer chemisorbed on a gold-covered surface of a porous alumina substrate etched in phosphoric acid solution. The figure is not drawn to scale. This membrane system can be electrically described by an equivalent circuit composed of a parallel *RC*-element (R_m and C_m) representing the electrical behavior of a lipid bilayer in series to an Ohmic resistance R_el representing the electrolyte solution.

Why did we call these pore-suspending lipid bilayers nano-BLMs? The term ′nano′ derives from the pore size of the porous substrate in the nanometer range. The term ′BLM′ is used because each membrane suspending a pore can be seen as freestanding BLM separated from each other by hybrid lipid bilayers consisting of the fixed DPPTE-monolayer supplemented to a bilayer by a DPhPC-monolayer (Fig. 20).

4.2.1.1 Thinning out process of the solvent

Directly after applying the lipid droplet onto the functionalized porous surface the obtained capacitance values are typically smaller than the final ones. By continuously recording impedance spectra, changes in the electrical parameters of the formed layer can be followed time-resolved. A typical time-resolved change in capacitance is depicted in Fig. 21.

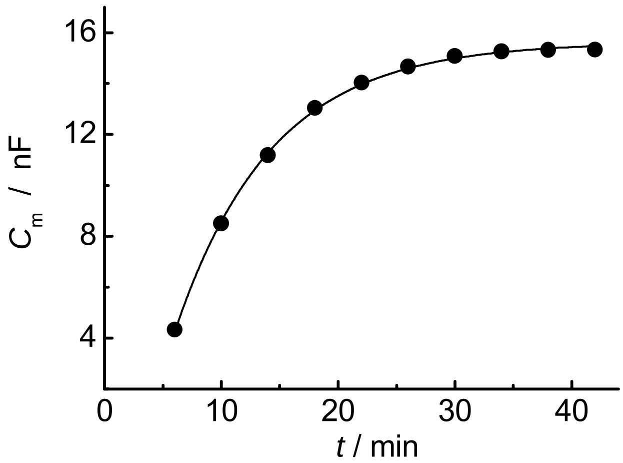

FIGURE 21: Time-dependent increase in capacitance C_m after painting a lipid droplet across the porous matrix. The membrane capacitance C_m increases from 4.3 nF to a final value of 15.3 nF. The solid line is the result of an asymptotical fit to the data and serves as a guide for the eye.

The bilayer formation process starts at a capacitance of 4.3 nF and increases until it levels off at a stable capacitance value of 15.3 nF. The increase in capacitance can be attributed to a thinning process of the bilayer [139] and was observed for all successful membrane preparations. The thinning process takes approximately 10-35 minutes until a stable and constant membrane capacitance is reached.

4.2.1.2 Long-term stability of nano-BLMs followed by impedance spectroscopy

For the specific membrane resistance maximum values of up to $1.6 \cdot 10^8$ Ω cm^2 were obtained for nano-BLMs bathed in 0.5 M KCl solution. The achieved membrane resistances of nano-BLMs are similar to those of traditional BLMs and are obviously sufficient to perform single channel recordings. However, the suitability of classical BLMs in biosensor applications is limited, as the BLM ruptures at a certain point, i.e. owing to mechanical distortion, in one single event leading to the loss of membrane resistance at all. To prove, if the nano-BLM ruptures like a classical BLM or in a completely different manner, the change in membrane resistance was investigated time-resolved by means of impedance spectroscopy.

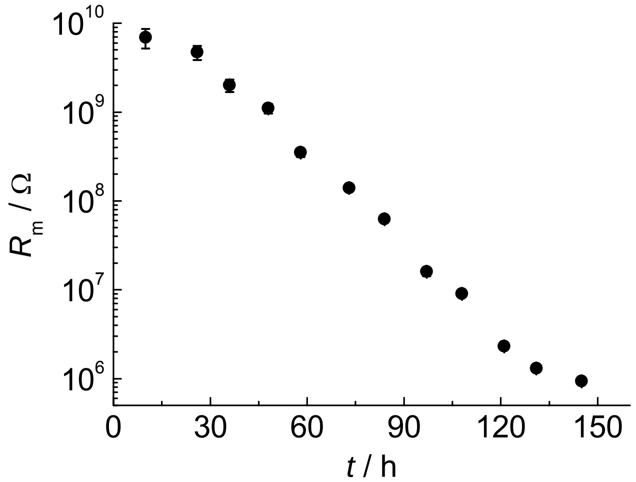

FIGURE 22: Time course of the membrane resistance R_m obtained by electrochemical impedance analysis of a nano-BLM in a frequency range of 10^{-2}-10^6 Hz. The membrane resistance was extracted from the impedance data by fitting the parameters of the equivalent circuit shown in Fig. 20 to the data. Error bars indicate the error of the fit parameter R_m.

In Fig. 22, R_m as a function of time is shown. In the first 48 hours after membrane formation, R_m drops from 7 GΩ to 1 GΩ. During this time period, the membrane is well suited for single channel measurements. Then, the membrane resistance further decreases leading to membrane resistances of around 150 MΩ after 72 hours, 16 MΩ after 96 hours and 2 MΩ after 120 hours. After 132 hours the membrane resistance has been lowered to 1 MΩ. From a statistical analysis (n = 5), the stability of nano-BLMs with membrane resistances larger than 1 GΩ was calculated to be (1.5 ± 0.5) days, (2.5 ± 1) days for those with resistances larger than 100 MΩ, (3.5 ± 1) for those larger than 10 MΩ, and (4.5 ± 1.5) days for those larger than 1 MΩ. After (5 ± 1.5) days the membrane resistance was decreased to values below 1 MΩ.

The continuous decrease in membrane resistance obtained for nano-BLMs differs significantly from the expected behavior of a single membrane spanning an aperture, which typically ruptures in one single step as observed for classical BLMs. Each membrane suspending a pore can rupture individually, which implies that each membrane is decoupled from the others and thus, ruptures separately, what would result in a continuously decreasing membrane resistance.

In conclusion, nano-BLMs exhibit an extraordinary long-term stability compared to classical BLMs. The porous substrate serving as membrane-stabilizing support plays an important factor for this purpose.

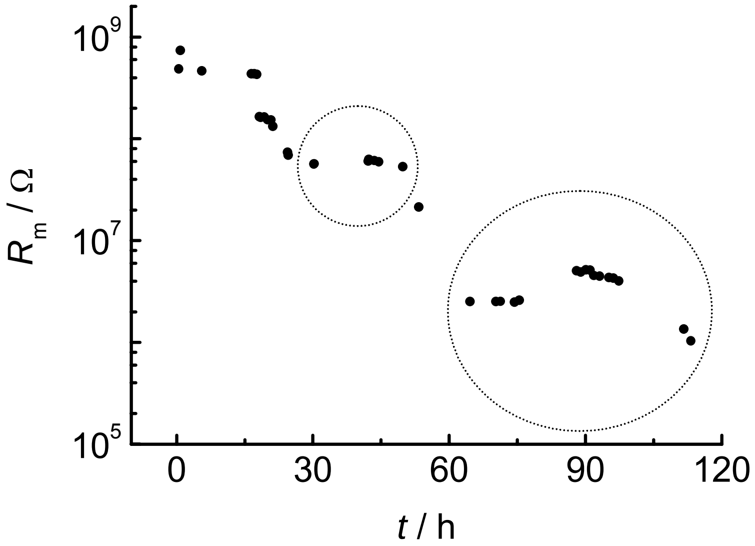

FIGURE 23: Time course of the membrane resistance R_m obtained by electrochemical impedance analysis of a nano-BLM in a frequency range of 10^{-2}-10^6 Hz. The circles mark the observed increases in membrane resistance R_m, indicating a “self-healing” process of the membrane.

Notably, in some cases it occurred during the time course of the experiment that the membrane resistance increased again, which indicates that a self-healing process might occur within the membrane (Fig. 23). This implies that nano-BLMs underlie permanent fluctuations affecting the resistance of the membrane.

4.2.1.3 Long-term stability of nano-BLMs investigated by fluorescence intensity recordings

In order to further prove the idea of the high long-term stability of nano-BLMs, the diffusion of the membrane-impermeable dye 5,6-carboxyfluorescein (CF) was studied across porous substrates with and without nano-BLMs by fluorescence intensity recordings. An intact lipid bilayer is impermeable for polar and charged molecules and would thus inhibit the passage of CF.

The porous alumina substrate with pore sizes of 280 nm was vertically placed between the two aqueous compartments of the Teflon cell depicted in Fig. 7*B*. The fluorescent dye 5,6-carboxyfluorescein was added to the buffer solution (10 mM Tris, pH 7.4) of the *cis* compartment to a final concentration of 2 mM. The diffusion of CF through the formed nano-BLM was measured as an increase in fluorescence in the *trans* compartment.

Emission spectra of the fluorescent buffer solution were recorded using an excitation wavelength of λ_{ex} = 495 nm. The maximal fluorescence intensity was obtained from the maximum in the emission spectra at a wavelength of λ_{em} = 515 nm. Fig. 24 shows emission spectra recorded in time intervals of the diffusion of CF through the alumina pores without a lipid bilayer suspending the pores. The experiment was started with the addition of the fluorescent dye CF to the *cis* compartment accompanied by recording of a first emission spectrum of the buffer solution in the *trans* compartment (◀). The fluorescence intensity in the *cis* compartment was defined to be 1 at time t = 0. Fluorescence spectra recorded after 4 h (○), 10 h (■), 22 h (△), 70 h (●) and 118 h (✯) show an increase in fluorescence intensity up to a value of 0.46 after 118 h, which is close to the maximal value of 0.5 in case of a homogeneously distributed fluorophore in both compartments with equal volumes.

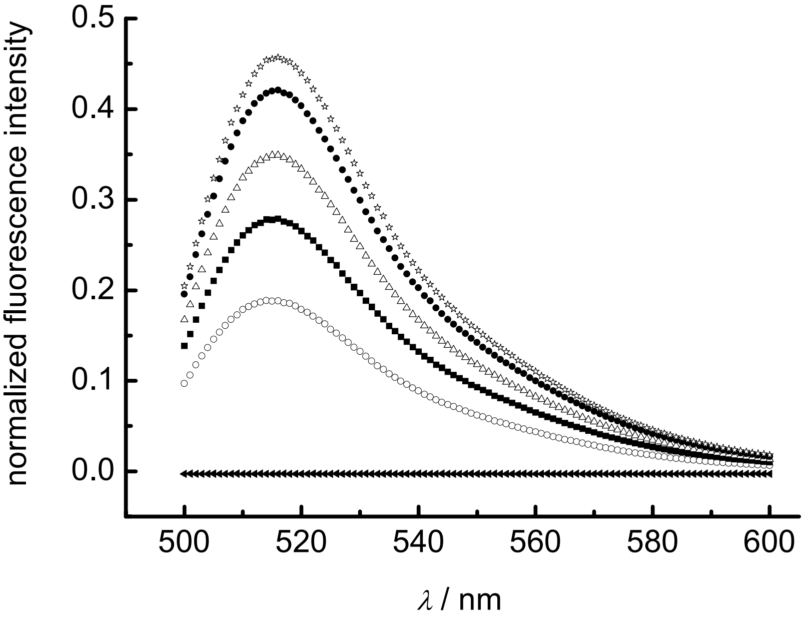

FIGURE 24: Emission spectra of the fluorescent dye 5,6-carboxyfluorescein, taken from the *trans* compartment without a nano-BLM suspending the pores with pore sizes of 280 nm (λ_{ex} = 495 nm). The emission spectra were recorded at the beginning of the experiment (◀), after 4 h, 10 h (■), 22 h (△), 70 h (●) and 118 h (✯).

The recordings of the fluorescence intensity in the *trans* compartment that was separated from the *cis* compartment by a nano-BLM also displayed an increase in fluorescence to a value of 0.41 after 118 h, but the time course of fluorescence intensity increase differed significantly from that obtained for the diffusion experiment across the porous subtstrate lacking the nano-BLM.

The time courses of the diffusion of CF through porous alumina with (○) and without (◆) a pore-suspending lipid bilayer investigated by fluorescence intensity recordings are compared in Fig. 25. It is obvious that the diffusion of the membrane-impermeable dye CF is hindered, but not completely inhibited by the nano-BLM suspending the porous matrix (○). After 10 h only a small amount of CF passed the nano-BLM accompanied by a small fluorescence intensity of 0.01 in the *trans* compartment, indicating that the membrane is still intact and almost all pores are covered with a lipid bilayer. A fluorescence intensity of 0.14 after 70 hours shows that the quality of the membrane slightly decreases over time. However, the small increase in fluorescence to a value of 0.2 after 94 hours points out that not the whole membrane has ruptured, but only parts of it, which then allows the passage of CF. In contrast, the unhindered diffusion through the alumina pores without a nano-BLM (◆) resulted in a considerable fluorescence intensity increase to 0.28 already after 10 h. The time course of fluorescence intensity obtained from recordings without a pore-suspending bilayer describes a typical saturation curve. The free diffusion of CF from the *cis* to the *trans* compartment without a porous substrate separating the two chambers is already complete after few hours depending on the size of the hole in the Teflon wall. Apparently, porous alumina substrates slow down the diffusion process due to theirs small pore sizes and their pore length of around 200 µm.

The slow, but continuous increase in fluorescence intensity over time supports again the hypothesis that each membrane, spanning a single pore, ruptures individually without that the whole nano-BLM collapses at once.

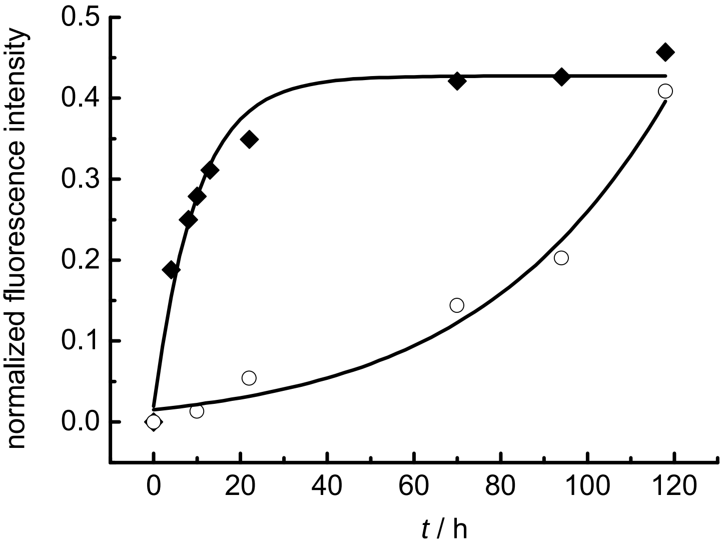

FIGURE 25: Time courses of the diffusion of the water-soluble, membrane-impermeable dye 5,6-carboxyfluorescein recorded in the *trans* chamber, which is separated from the *cis* chamber by porous alumina with (O) and without (◆) a pore-suspending lipid bilayer, as fluorescence increase. The solid lines are the results of an asymptotical fit to (◆) and an exponential growth fit to (O), respectively, and serve as a guide for the eye.

4.2.2 Formation and stability of micro-BLMs based on macroporous silicon

The question arose whether lipid bilayers suspending pores with pore sizes in the micrometer range could also be formed by the painting technique already established for the formation of nano-BLMs. For this purpose, macroporous silicon substrates with pore diameters of 1 µm were chosen as supports. The formed lipid bilayers suspending silicon macropores were termed micro-BLM due to the larger pore size in the micrometer range. Expect for the pore size, micro-BLMs resemble nano-BLMs. A schematical model of a micro-BLM is presented in Fig. 26.

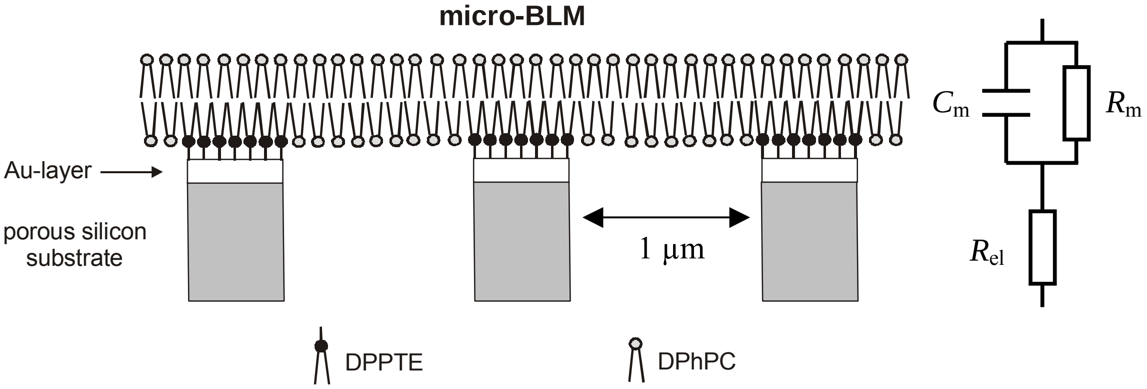

FIGURE 26: Micro-BLM composed of DPhPC and a DPPTE-submonolayer chemisorbed on the gold-covered surface of the porous silicon substrate. The lipid bilayer supported on the macroporous silicon substrate is not drawn to scale. The corresponding equivalent circuit was yet described for modeling the electrical parameters of a nano-BLM.

4.2.2.1 Formation of micro-BLMs

For micro-BLM formation, the gold-coated lower surface of the macroporous silicon substrate was functionalized with a self-assembled DPPTE-monolayer rendering the surface hydrophobic. Impedance analysis revealed that the self-assembled DPPTE-monolayer does not change the impedance behavior of the system (Fig. 27, ■). Subsequently the phospholipid DPhPC dissolved in *n*-decane was spread on the selectively functionalized porous substrate. Over time, the initially formed hydrophobic lipid droplet with a thickness of several micrometers thinned out to form a planar lipid bilayer completing the self-assembled DPPTE-submonolayer patches.

The formation of micro-BLMs was followed by means of impedance spectroscopy in a frequency regime of 10^{-2}-10^{6} Hz (Fig. 27). For very large membrane resistances impedance measurements down to 10^{-3} Hz were carried out. The impedance spectra depicted in Fig. 27 were taken before (closed symbols), 49 and 70 hours (open symbols) after micro-BLM formation, respectively. Both spectra (□, ○) clearly indicate the formation of an insulating layer on the porous matrix. To model the impedance spectra and extract membrane specific parameters, the same equivalent circuit as used for electrical characterization of nano-BLMs was utilized. This circuit, depicted in Fig. 26, is composed of a parallel $R_m C_m$-element in series to an Ohmic resistance R_{el}. The results of the fitting routine are shown as solid lines in Fig. 27 and indicate an excellent agreement between data and fit. Membrane capacitances of C_m = 6.9 nF (□) and 7.6 nF (○), respectively with fitting errors of less than 1 % were obtained. For nine independent membrane preparations, a mean membrane capacitance of (9.7 ± 3.3) nF was calculated. Since the current exclusively flows through the pores, only the active porous area has to be taken into account for the calculation of the specific membrane capacitance C_m^A. Taking the active area of A = 1.54 mm^2 into account, which can be calculated from the total area exposed to the buffer solution (A = 7 mm^2) and a porosity of 22 %, the mean capacitance of C_m = (9.7 ± 3.3) nF translates into a specific membrane capacitance of C_m^A = (0.63 ± 0.21) µF/cm^2.

The membrane resistance R_m is determined in the very low frequency regime. It becomes more or less discernible depending on its absolute value. If R_m is larger than 10 GΩ, the fitting error exceeds 10 %. For example, for the impedance spectra shown in Fig. 27, R_m was calculated to be 23.1 GΩ (□) with a fitting error of 32 %, while the fitting error for a membrane resistance of R_m = 1.5 GΩ (○) is only 4.5 %.

The largest membrane resistance obtained by impedance analysis in a frequency range of 10^{-3}-10^{6} Hz was 118 GΩ with a fitting error of 46 %. This value translates into a specific membrane resistance of R_m^A = 1.82 GΩ cm^2.

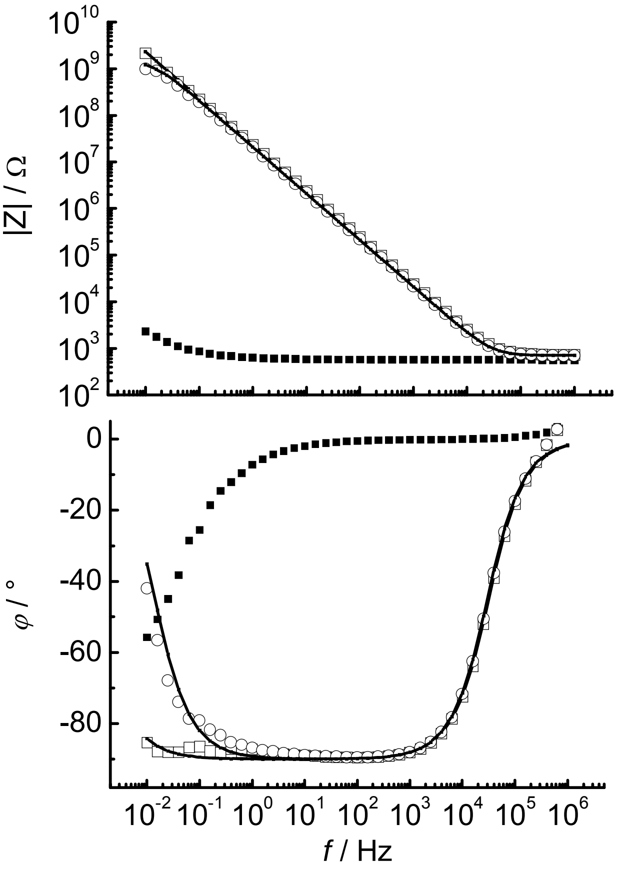

FIGURE 27: Impedance spectra of gold-covered porous silicon substrates functionalized with a DPPTE-monolayer before (■) and after (□, ○) spreading of a lipid droplet across the porous silicon substrate. (□) shows an impedance spectrum obtained 49 hours after formation of a micro-BLM, (○) depicts an impedance spectrum of the same bilayer preparation after 70 hours. The solid lines are the results of the fitting procedure using the equivalent circuit shown in Fig. 26: (□) C_m = 6.9 nF, R_m = 23.1 GΩ; (○) C_m = 7.6 nF, R_m = 1.5 GΩ.

4.2.2.2 Long-term stability of micro-BLMs

The long-term stability of micro-BLMs, as expressed in terms of the membrane resistance was investigated by means of impedance spectroscopy in order to elucidate how the membrane stability is affected by the pore diameter of the porous substrate. A mean stability of micro-BLMs with membrane resistances exceeding 1 GΩ was calculated to be (29 ± 17) hours (*n* = 3). In Fig. 28, the time course of the membrane resistance R_m for a micro-BLM with a very high long-term stability is shown. One hour after membrane formation, the micro-BLM exhibits a resistance of 37 GΩ. The value decreases over time leading to a membrane resistance of 5.4 GΩ after 24 hours, 2.3 GΩ after 50 hours and 1.5 GΩ after 70 hours.

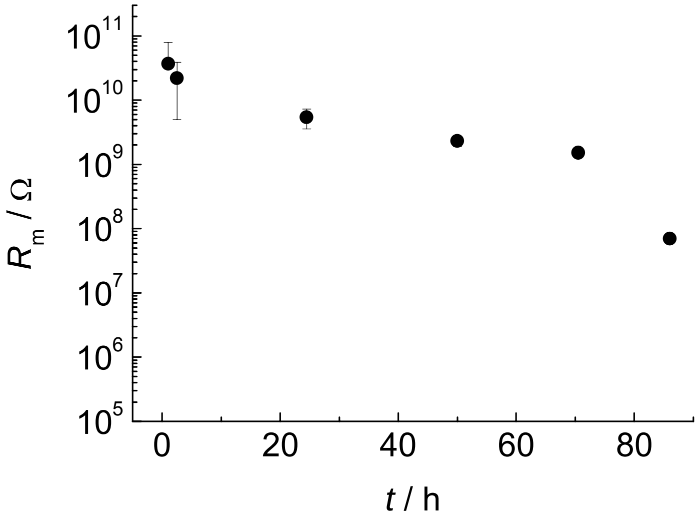

FIGURE 28: Time course of the membrane resistance R_m obtained by electrochemical impedance analysis of a micro-BLM in a frequency range of 10^{-2}-10^{6} Hz. The membrane resistance was obtained by fitting the parameters of the equivalent circuit shown in Fig. 26 to the impedance data. Error bars indicate the error of the fit parameter R_m.

The stability of the membrane with resistances in the gigaohm regime lasting around 1 day is slightly lower than that of nano-BLMs lasting around 1.5 days. In general, the porous substrate stabilizes the membrane and enhances its long-term stability. The stability is, however, a function of the pore size. It slightly decreases with increasing pore size.

As reported for nano-BLMs, the membrane resistances decrease continuously and not abruptly in one single step confirming the idea that each membrane suspending a pore can rupture individually.

4.2.3 Formation and stability of porous matrix-supported BLMs based on porous substrates

Nano-BLMs as well as micro-BLMs were formed according to the painting technique on the functionalized lower surface of porous substrates. Self-assembled monolayers of either DPPTE or ODT on the gold-coated porous surface were a prerequisite for this type of lipid bilayer formation.

The question arose, whether it is possible to form membranes on porous supports without a preceding functionalization of the surface to address the following points:

- Does the partial fixation of the membrane due to chemisorption of the thiolipid DPPTE on the gold-covered surface influence the stability of the membrane?
- Is each membrane-suspended pore decoupled from the others due to the DPPTE-submonolayer?
- Does DPPTE hinder the lateral mobility of integrated ion channels?

4.2.3.1 Formation of porous matrix-supported BLMs

In the case of porous alumina with pore sizes of 280 nm the formation of lipid bilayers without gold- and DPPTE-coating failed. Lipid bilayers were only formed in the case of macroporous silicon substrates by spreading DPhPC in *n*-decane onto the porous matrix. These pore-suspending lipid bilayers are called porous matrix-supported BLMs. A conceivable arrangement of such a membrane, termed porous matrix-supported BLM, is schematically shown in Fig. 29.

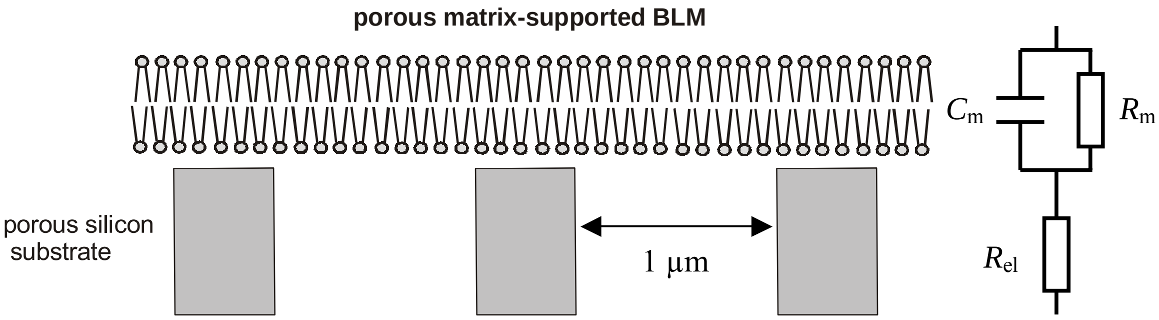

FIGURE 29: Suggested schematical representation of a porous matrix-supported BLM composed of DPhPC. The lipid bilayer suspending the macroporous silicon substrate is not drawn to scale. The corresponding equivalent circuit was yet used for electrical characterization of nano- and micro-BLMs.

Impedance spectra again clearly indicate the formation of a pore-suspending lipid bilayer across the porous matrix. A good agreement between data and fit is achieved by using the equivalent circuit shown in Fig. 29. For four membrane preparations, a mean specific membrane capacitance of $C_m^A = (0.78 \pm 0.34)$ µF/cm^2 and membrane resistances in the GΩ regime were obtained. According to the impedance data highly insulating porous matrix-supported BLMs were formed. However, a detailed membrane structure cannot be provided. Matrix-supported BLMs cover the macroporous silicon substrate without any covalent linkage to the porous matrix. Some stablilization could be achieved by electrostatic interactions between the hydrophilic head groups of the phospholipids and the hydrophilic silicon matrix.

4.2.3.2 Stability of porous matrix-supported BLMs

A comparison between the membrane stabilities of micro-BLMs and porous matrix-supported BLMs should give information about the assembly of the pore-suspending lipid bilayers since both systems are based on macroporous silicon substrates with pore sizes of 1 µm and differ only in the functionalization of the surface. Thus, the time-dependent change in membrane resistance R_m as a measure of long-term stability was also investigated for porous matrix-supported BLMs.

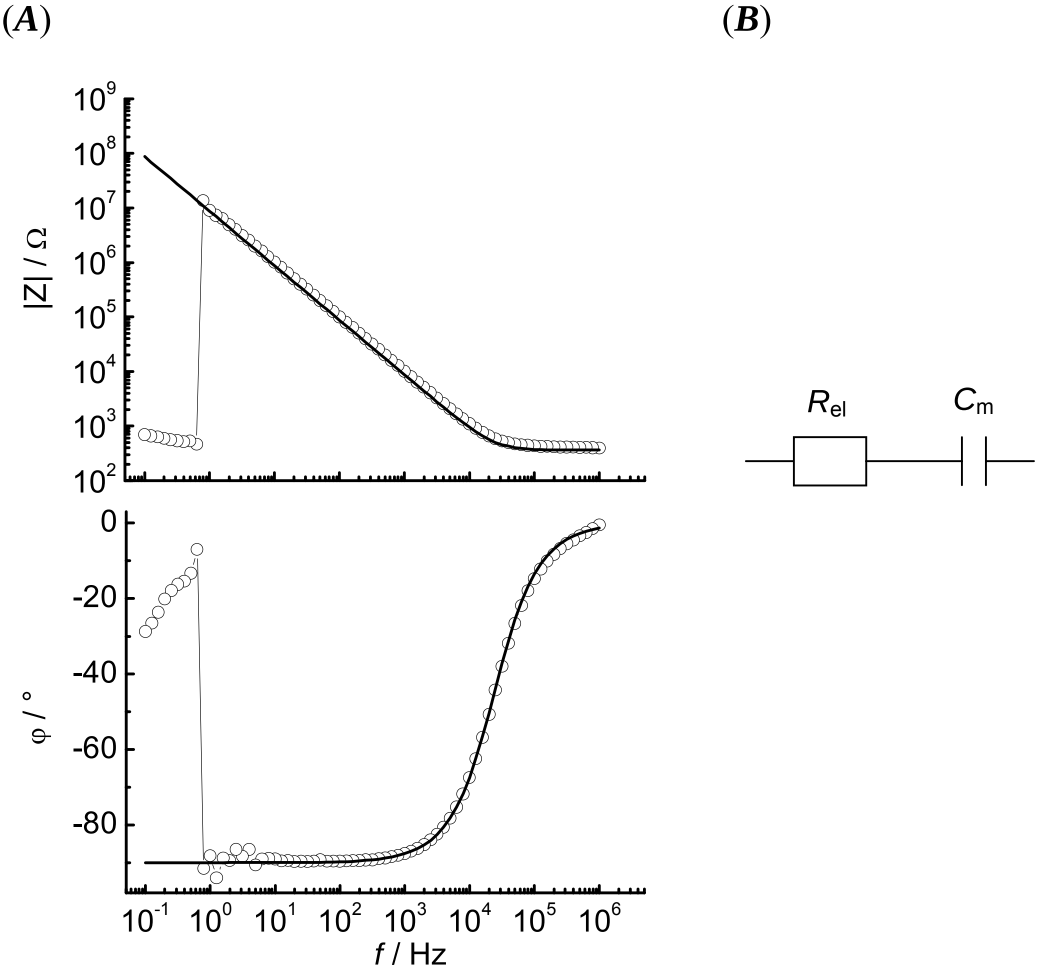

FIGURE 30: (*A*) Impedance spectrum of a porous matrix-supported BLM that ruptures during the time of the impedance recording. The solid line is the result of the fitting procedure with the equivalent circuit shown in (*B*). A membrane capacitance C_m of 18.3 nF was determined. (*B*) Equivalent circuit composed of the membrane capacitance C_m in series to the resistance R_{el} of the electrolyte.

Though the achieved membrane resistances were in principle in the same range as those obtained for micro-BLMs, a continuous time-dependent decrease in membrane resistance was not monitored. Instead, after a certain time a sudden drop in membrane resistance was observed indicative of a complete rupture of the membrane. This membrane collapse in one single event resembles that observed for conventional freestanding BLMs.

Such an event was observed during the recording of an impedance spectrum (Fig. 30*A*) indicated by the unexpected decrease in impedance leading to a spectrum that is characterized by the resistance of the electrolyte R_{el}. The result of the fitting procedure using the equivalent circuit shown in Fig. 30*B* composed of a membrane capacitance in series to the resistance of the electrolyte, displays a good accordance between data and fit. In this equivalent circuit, the membrane resistance was neglected as it was not anymore determined in the observed impedance spectra. The specific membrane capacitance of $C_m^A = 1.05\ \mu F/cm^2$ confirms the good quality of the membrane, although it ruptured thereafter.

In general, membrane resistances of porous matrix-supported BLMs suited for single channel recordings were found within a broad time interval ranging from only 10 minutes up to 27 hours.

4.3 Formation of pore-suspending lipid bilayers by vesicle spreading and fusion

4.3.1 Lipid bilayer formation via spreading of thiolipid-containing vesicles

Vesicle spreading and fusion experiments were performed on gold-coated porous alumina substrates in order to form solvent-free pore-suspending lipid bilayers. The solvent inclusion in case of nano- and micro-BLMs as a consequence of the preparation technique might influence the properties of the membrane and the functionality of incorporated membrane proteins.

4.3.1.1 Vesicle spreading and fusion on planar gold electrodes

Before performing vesicle spreading experiments on porous alumina substrates the suitability of three preselected lipid mixtures for spreading and fusion were analyzed on planar gold electrodes. For this purpose, thiolipid-containing vesicles that are known to chemisorb onto gold surfaces were used. According to the experiments of Drexler and Steinem [134, 140], who have already formed lipid bilayers with a lipid composition of DPPTE/DOPC (60/40 wt %) on planar gold electrodes and porous alumina, this lipid mixture and two variations (DPPTE/DPhPC (60/40 wt %) and DPPTE/DPhPC/

cholesterol (40/30/30 wt %)) were chosen. Planar gold electrodes were incubated with vesicle suspensions composed of these lipid mixtures with nominal diameters of 100 nm in order to form defect-free solid supported lipid membranes.

A lipid bilayer, immobilized on a polarizable electrode such as a gold electrode, can be described by an equivalent circuit depicted in Fig. 31*A*. The lipid bilayer is represented by a parallel R_mC_m-element which is in series to the resistance of the electrolyte R_{el}. In addition, a capacitance C_{Au} resulting from the electrochemical double layers at the interfaces must be taken into account. If the membrane resistance R_m exhibits values above 10 MΩ, they cannot be determined in the observed frequency regime between 10^{-1}-10^6 Hz. Then, the equivalent circuit presented in Fig. 31*A* is reduced to a serial connection of the electrolyte resistance R_{el} and the combined capacitance C_{Au+m} of the membrane and electrode capacitance as shown in Fig. 31*B*.

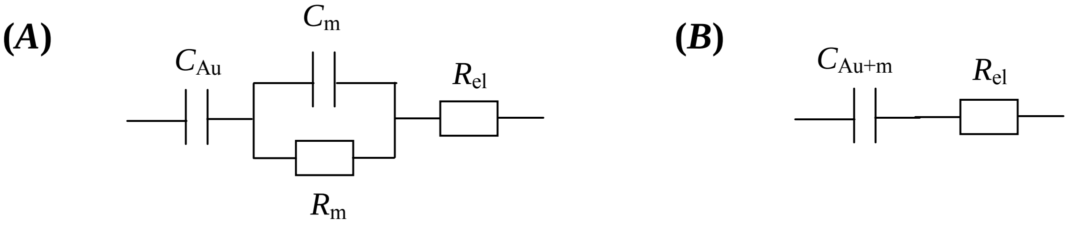

FIGURE 31: Equivalent circuits describing the electrical behavior of a lipid bilayer immobilized on a planar gold electrode. In (*A*), the parallel R_mC_m-element representing a lipid bilayer is in series to the resistance of the electrolyte R_{el} and the capacitance of the gold electrode C_{Au}. A simplified equivalent ciruit for the description of solid supported membranes with membrane resistances that cannot be detected in the observed frequency regime is displayed in (*B*). The capacitances C_{Au} and C_m merge to the capacitance C_{Au+m} as they cannot be distinguished. The combined capacitance C_{Au+m} is in series to the resistance of the electrolyte R_{el}.

Only the sum C_{Au+m} of the membrane and electrode capacitance in serial connection is determined:

$$C_{Au+m} = \frac{1}{\frac{1}{C_m} + \frac{1}{C_{Au}}}. \qquad \textbf{(Eq-17)}$$

The impedance spectra presented in Figs. 32*A*/*B* were both recorded 3 hours after incubation of a gold electrode with (*A*) DPPTE/DPhPC vesicles (60/40 wt %) and (*B*) DPPTE/DPhPC/cholesterol vesicles (40/30/30 wt %) of 100 nm in nominal vesicle size at $T = 55$ °C.

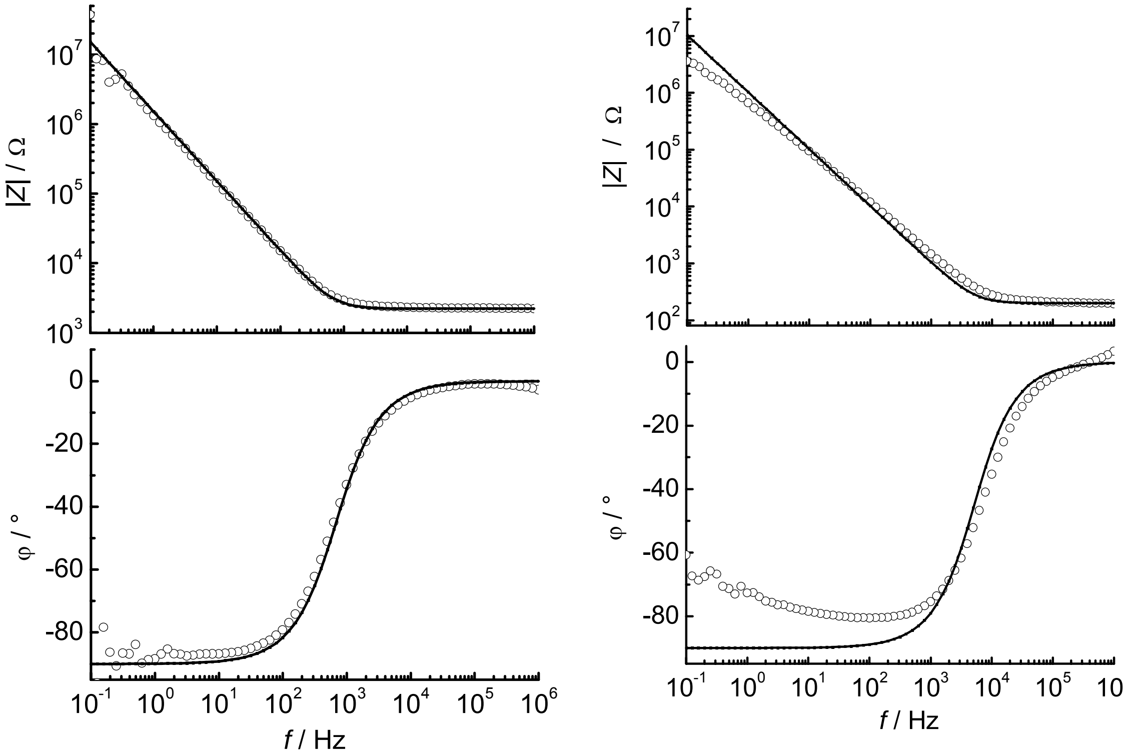

FIGURE 32: (*A*/*B*) Impedance spectra of planar gold electrodes with an area of $A = 0.13$ cm^2 recorded in 10 mM Tris, 100 mM Na_2SO_4, pH 7.4 3 hours after incubation with large unilamellar vesicles composed of (*A*) DPPTE/DPhPC (60/40 wt %) and (*B*) DPPTE/DPhPC/cholesterol (40/30/30 wt %) at a temperature of $T = 55$ °C. The solid lines are the results of the fitting procedure using the equivalent circuit shown in Fig. 31*B* composed of the combined capacitance $C_{\mathrm{Au+m}}$ in series to the resistance of the electrolyte R_{el}. (*A*) A capacitance of $C_{\mathrm{Au+m}} = 0.11$ µF was calculated that is almost similar to the dominating membrane capacitance C_{m}. C_{m} translates into a specific membrane capacitance of $C_{\mathrm{m}}^{\mathrm{A}} = 0.85$ µF/cm^2. (*B*) $C_{\mathrm{Au+m}} = 0.15$ µF, $C_{\mathrm{m}}^{\mathrm{A}} = 1.15$ µF/cm^2. In (*B*) there is limited accordance between data and fit, typical for this type of bilayer preparation.

A capacitance of $C_{\mathrm{Au+m}} = 0.11$ µF was determined for the impedance spectrum in Fig. 32*A* using the equivalent circuit depicted in Fig. 31*B*. The membrane capacitance of $C_{\mathrm{m}} = 0.11$ µF was calculated based on equation 17, assuming an electrode capacitance of $C_{\mathrm{Au}} = 30$ µF/cm^2 according to the Gouy-Chapman-Stern model [18, 97, 100]. As the membrane capacitance C_{m} is around 30 times smaller than the capacitance of the gold electrode C_{Au}, $C_{\mathrm{Au+m}}$ is dominated by the membrane capacitance C_{m}. Taking the area of A = 0.13 cm^2 into account, C_{m} translates into a specific membrane capacitance of C_{m}^{A} = 0.85 µF/cm^2 (n = 3). A specific membrane capacitances of C_{m}^{A} = 1.15 µF/cm^2 was calculated for the lipid bilayer formed by incubation of a planar gold electrode with DPPTE/DPhPC/cholesterol vesicles.

The results of the fitting procedure with the equivalent circuit displayed in Fig. 31*B* were not always in such a good accordance with the impedance data as depicted in Fig. 32*A*. Deviations from the fit as shown in Fig. 32*B*, particularly in the lower frequency regime, indicate that many lipid bilayers formed by spreading of thiolipid-containing vesicles on planar gold surfaces contained defects that influence the electrical behavior of the bilayer.

In general, specific membrane capacitances of 0.8-2.0 µF/cm^2 were obtained for the formed solid supported lipid membranes, which differ in lipid composition, indicating the suitability of the employed lipid mixtures for vesicle spreading and fusion on gold-coated porous alumina.

4.3.1.2 Vesicle spreading and fusion on porous alumina substrates

The three vesicle systems (system 1: DPPTE 60 wt %, DOPC 40 wt %; system 2: DPPTE 60 wt %, DPhPC 40 wt %; system 3: DPPTE 40 wt %, DPhPC 30 wt %, cholesterol 30 wt %) were transferred to gold-coated porous alumina substrates with pore sizes of 55 nm. Pore sizes of 55 nm were chosen in order to be able to reproduce the exact conditions as used for vesicle spreading experiments on planar gold surfaces. Nominal vesicle sizes of 100 nm in diameter ensure that the vesicles are excluded from the pore interior.

The incubation process of vesicle suspensions with nominal vesicle diameters of 100 nm resulted in a change in the impedance spectrum compared to the spectrum of the neat porous alumina taken prior the incubation process. As control experiments, porous alumina substrates were incubated in pure buffer solution at different temperatures T (RT-60 °C) for different time periods from 1 hour up to 1 day. Impedance spectra were taken continuously. No alteration of the impedance spectra was observed after incubation of the alumina substrates in buffer solution varying the temperature and incubation time.

These results indicate that the obtained changes in the impedance spectra after vesicle spreading can be attributed to the formation of a lipid bilayer on the porous matrix.

As an example, the impedance data obtained after incubating a gold-covered porous alumina substrate with DPPTE/DPhPC/cholesterol vesicles (40/30/30 wt %, 100 nm nominal vesicle size) is presented in Fig. 33, together with the results of fitting procedures using different equivalent circuits.

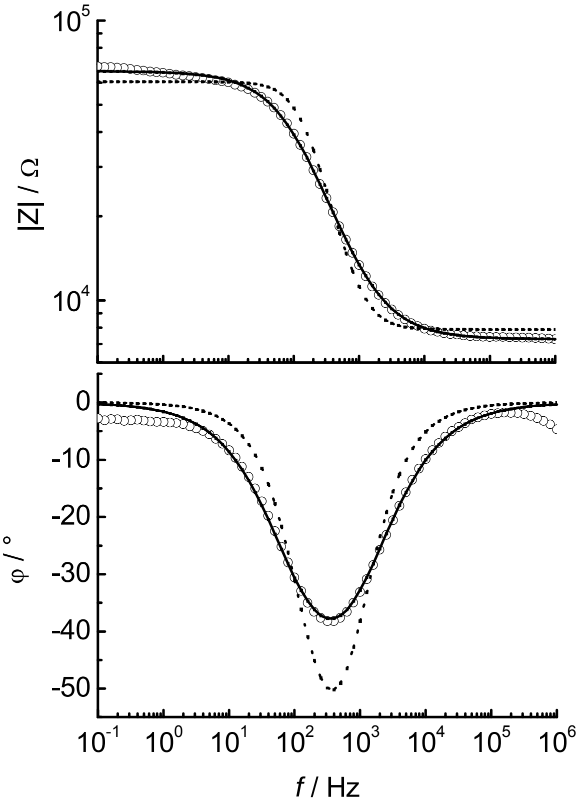

FIGURE 33: Impedance spectrum of a lipid bilayer (O) formed by vesicle spreading and fusion of DPPTE/DPhPC/cholesterol vesicles (40/30/30 wt %) on a highly ordered gold-covered porous alumina substrate with pore sizes of 55 nm. The dashed line is the result of the fitting procedure using the equivalent circuit *RRC*, shown in Fig. 34*A*, while the solid line is the result of the fitting procedure with the *RRCPE*-equivalent circuit presented in Fig. 34*B*. Based on the *RRCPE*-equivalent circuit a value of A_m = 0.14 µF with n = 0.76 and an overall resistance of R_o = 58.8 kΩ were obtained.

The standard fitting procedure with the *RRC*-equivalent circuit representing the electrical characteristics of an ideal lipid bilayer (Fig. 34*A*) is shown as dashed line in Fig. 33. As can be seen, there are obvious deviations between data and fit.

Inhomogeneities in the lipid bilayer might account for the deviation of the simple parallel *RC*-element representing the planar lipid bilayer, from the data. Lipid bilayer systems formed by vesicle spreading and fusion are often better described by distributed elements. Wiegand et al. used a more sophisticated model composed of three parallel *RC*-elements accounting for the inhomogeneities [18, 19]. Here, the capacitance C_m was replaced by a constant phase element (CPE) to attribute for the non-ideal behavior of the lipid bilayer immobilized on the porous support (Fig. 34*B*)

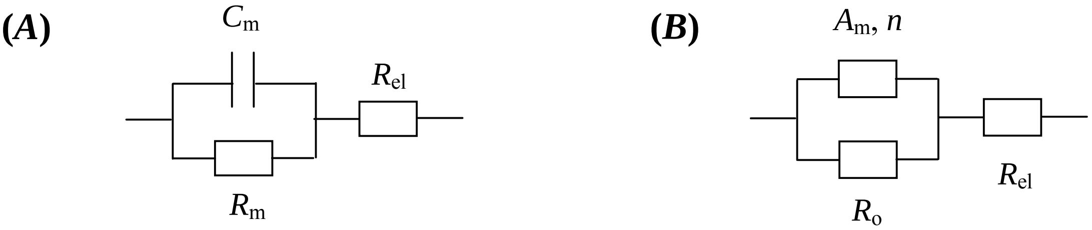

FIGURE 34: Equivalent circuits with ideal and distributed circuit elements describing the electrical behavior of a lipid bilayer. (*A*) *RRC*-equivalent circuit consisting of ideal circuit elements. (*B*) *RRCPE*-equivalent circuit consisting of a parallel connection of the constant phase element (A_m, n) and the overall resistance R_o in series to the resistance of the electrolyte R_{el}.

The result of the fitting procedure with the *RRCPE*-equivalent circuit (Fig. 34*B*) comprising a parallel connection of the constant phase element (A_m, n) as distributed circuit element instead of the membrane capacitance C_m and the overall resistance R_o, in series to the resistance of the electrolyte R_{el} is displayed as solid line in Fig. 33. The measured resistance is such small that it is not longer referred to as membrane resistance, but as overall resistance R_o.

Apparently there is a good accordance between data and fit. A capacitance of A_m = 0.14 µF with n = 0.76 was determined, differing by a factor of 6 from C_m = 22.51 nF resulting from fitting the parameters of the *RRC*-equivalent circuit.

Fig. 35 displays the impedance data of a lipid bilayer (○) formed by vesicle spreading on a gold-functionalized porous alumina surface over night at a temperature of T = 55 °C, and additionally the data of the neat porous alumina substrate (■). The alumina substrate was incubated in a vesicle suspension with a lipid composition consisting of 60 wt % DPPTE and 40 wt % DPhPC, exhibiting nominal vesicle sizes of 100 nm in diameter.

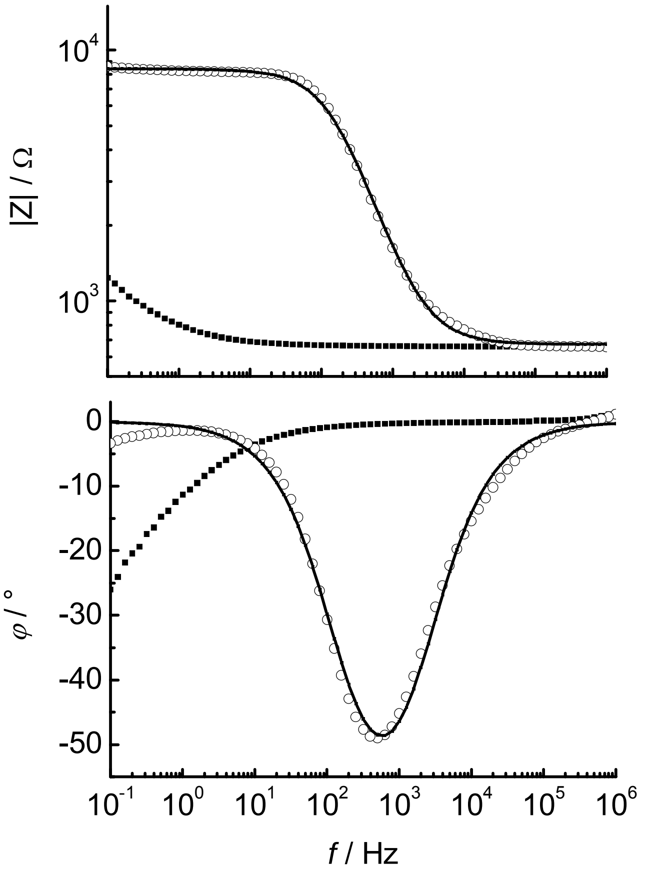

FIGURE 35: Impedance spectra of an ordered gold-covered porous alumina substrate before (■) and after (○) incubation with DPPTE/DPhPC unilamellar vesicles (60/40 wt %; 100 nm nominal diameter) at a temperature of $T = 55$ °C over night. The solid line is the result of the fitting procedure using the equivalent circuit shown in Fig. 34*B*: $A_m = 0.38$ µF; $n = 0.87$; $R_o = 7.8$ kΩ.

The fit of the parameters of the distributed *RRCPE*-equivalent circuit depicted in Fig. 34*B* to the impedance data resulted in good agreement between data and fit. R_o and A_m were readily extracted from the impedance spectrum and exhibited values of $R_o = 7.8$ kΩ and of $A_m = 0.38$ µF with $n = 0.87$. In this experiment, n is still close to 1 implying that the parameter A_m can still be viewed as the capacitive behavior of the lipid bilayer. As illustrated in detail in chapter 4.2.1 the total current flows through the pores covered with a lipid bilayer and not through the thick alumina pore columns. According to this theory, A_m translates into a specific membrane capacitance of $C_m^A = 9.1$ µF/cm^2

based on a porous area of A = 4.2 mm^2. This high specific membrane capacitance value confirms that the formed lipid bilayer was definitely not defect-free.

Variation of parameters

With the aim to achieve entire pore coverage with a defect-free pore-suspending lipid bilayer, several parameters were varied, e.g. lipid composition, incubation time, incubation temperature and active area.

- Three lipid mixtures were analyzed to find the optimal lipid composition to form pore-suspending lipid bilayers. The use of DPPTE/DPhPC instead of DPPTE/DOPC lipid mixtures of the same ratio favored the formation of pore-suspending lipid bilayers with respect to the pore coverage. After vesicle spreading and fusion, a pore coverage of 91.4 % was calculated for a DPPTE/DPhPC (60/40 wt %) lipid mixture while a DPPTE/DOPC (60/40 wt %) lipid mixture resulted only in a pore coverage of 62.0 % (see chapter 4.3.1.3). The addition of cholesterol to the lipid mixture leading to a lipid composition of (40/30/30) wt % of DPPTE/DPhPC/cholesterol resulted in no significant increase in pore coverage.

- The formation of pore-suspending lipid bilayers was followed time-resolved by impedance spectroscopy. It turned out, that an incubation time between 4-12 hours favors the formation of a homogeneous lipid bilayer containing fewer defects.

- Vesicle spreading was induced by heating the lipid mixture above the main phase transition temperature of the lipid mixture. A temperature of T = 55 °C was chosen for all lipid mixtures to ensure that all lipids are above their main phase transition temperature.

- The active area, limited by sealing rings, was first varied between A = 7.0 mm^2 and A = 1.2 mm^2. The probability to cover all pores with a lipid bilayer should be favored by using smaller active areas. But during the incubation process at a temperature of T = 55 °C air bubbles were formed, which negatively affected the formation of defect-free pore-suspending lipid bilayers, particularly in Teflon cells exposing the small area of A = 1.2 mm^2 to the vesicle suspension. Therefore, the larger area of

A = 7.0 mm^2 was advantageous though larger with respect to the bilayer formation process.

In summary, by vesicle spreading and fusion lipid bilayers can be formed on porous alumina substrates, which are, however, not defect-free. Moreover, at the current state, the preparations are not very reproducible. Only one out of ten preparations exhibited notable pore coverage exceeding 70 %.

4.3.1.3 Calculation of the pore coverage

The impedance spectra of pore-suspending lipid bilayers formed by vesicle spreading and fusion (Figs. 33/35) differ from those formed by the painting technique (Figs. 19/27). The determined overall resistance R_0 reaches values far away from gigaohmic membrane resistances.

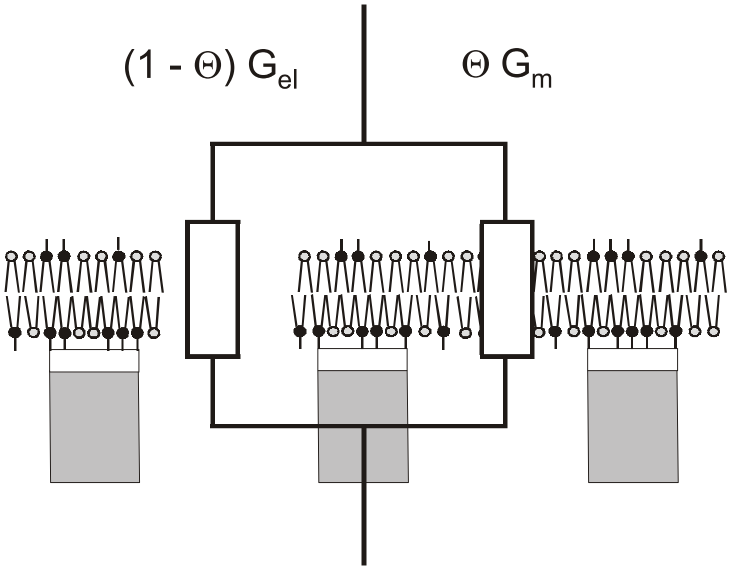

FIGURE 36: Schematic model for the calculation of the pore coverage of membrane-suspended porous alumina.

If only few pores of the porous substrate are uncovered, a large current flows through them, taking the line of the least resistance. More information about such a fractal system may be provided if the pore coverage by lipid bilayer patches is calculated. One part (Θ) of the porous alumina substrate is covered by a lipid bilayer while the other part ($1 - \Theta$) is uncovered. The overall conductance G of the system is composed of the single conductance of each uncovered pore represented by the conductance of the electrolyte G_{el}, and the conductance of the membrane-suspended pores G_{m}. The schematic model in Fig. 36 illustrates the following equation:

$$R_{\mathrm{o}} = \frac{1}{\Theta\, G_{\mathrm{m}} + \left(1 - \Theta\right) G_{\mathrm{el}}}\,. \qquad \textbf{(Eq-18)}$$

R_{m} is fixed to 1 GΩ, representing a typical resistance of an insulating bilayer, which corresponds to a membrane conductance of $G_{\mathrm{m}} = 1$ nS. R_{o} and R_{el} are acquired from impedance measurements. Transforming equation 18 into:

$$\Theta = \frac{1 - R_{\mathrm{o}} G_{\mathrm{el}}}{R_{\mathrm{o}}\left(G_{\mathrm{m}} - G_{\mathrm{el}}\right)} \qquad \textbf{(Eq-19)}$$

allows for a calculation of Θ, the pore coverage by a lipid bilayer.

The pore coverage Θ was calculated for various vesicle spreading experiments differing in the lipid composition. The best results of the pore coverage Θ are listed in Table 3, in addition with the corresponding specific membrane capacitance $C_{\mathrm{m}}^{\mathrm{A}}$, n, and the overall resistance $\mathrm{R_o}$. For various membrane preparations, the parameter A_{m} can be viewed as the capacitive behavior of the membrane, as a first approximation, since n is still close to 1, ranging between 0.87-0.76. Thus, A_{m} translates into $C_{\mathrm{m}}^{\mathrm{A}}$ taking the active porous area of $A = 4.2\ \mathrm{mm}^2$ into account.

TABLE 3: The pore coverage Θ, specific membrane capacitance C_m^A, *n*, and the overall resistance R_0 of pore-suspending lipid bilayers after spreading of different lipid mixtures (nominal vesicle size of 100 nm) are listed. The experiments were conducted in buffer solution (10 mM Tris, 100 mM Na_2SO_4, pH 7.4) at a temperature of $T = 55$ °C. The active porous area was $A = 4.2$ mm².

vesicle composition	**pore coverage** Θ	**capacitance** C_m^A	***n***	**resistance** R_0
DPPTE 60 wt % DOPC 40 wt %	62.0 %	7.9 µF/cm²	0.82	8.1 kΩ
DPPTE 60 wt % DPhPC 40 wt %	91.4 %	9.1 µF/cm²	0.87	7.8 kΩ
DPPTE 40 wt % DPhPC 30 wt % cholesterol 30 wt %	87.7 %	3.4 µF/cm²	0.76	58.8 kΩ

4.3.2 Formation of lipid bilayers based on porous alumina via electrostatic attractions

In addition to the spreading and fusion experiments of thiolipid-containing vesicles to planar lipid bilayers based on gold-covered porous alumina substrates via chemisorption, another technique was explored based on vesicle adsorption and spreading via electrostatic attractions.

The lower surface of the porous alumina substrate was modified by a thin gold layer, which was then functionalized via chemisorption with a monolayer of 3-mercaptopropionic acid (MPA) or 11-mercaptoundecanoic acid (MUDA) by incubation in 1 mM aqueous and ethanolic solution, respectively. At pH 8.6, the coated surface is negatively charged due to the deprotonated carboxylic acid group exposed to the buffer solution (10mM Tris, 10 mM Na_2SO_4, pH 8.6). The prefunctionalized surface was then incubated with LUVs composed of positively charged *N*,*N*-dioctadecyl-*N*,*N*-dimethyl ammonium bromide (DODAB) at a temperature of $T = 55$ °C. The hydrophilic negatively charged surface is supposed to interact with the positively charged vesicles and forces the adsorption and spreading of vesicles on the porous surface.

The fusion of DODAB vesicles to lipid bilayer structures on MPA-monolayers was visualized by Hennesthal et al. by means of scanning force microscopy (SFM) [141, 142].

However, by means of impedance spectroscopy, the formation of insulating DODAB lipid bilayers on the functionalized porous alumina substrates could not be followed. Impedance spectra did not change after incubation indicating that no insulating pore-suspending lipid bilayers were formed.

4.4 Ion channel recordings after peptide incorporation in pore-suspending lipid bilayers

4.4.1 Impedance analysis of gramicidin doped nano-BLMs

Functionality of nano-BLMs should be demonstrated by inserting channel-active peptides such as gramicidin or alamethicin. In particular, gramicidin is frequently used to support the idea of a single lipid bilayer as the peptide is only active if the membrane is as thin as one lipid bilayer. To investigate the influence of gramicidin on the electrical behavior of nano-BLMs the ion channel gramicidin was added to the electrolyte (0.1 M Na_2SO_4) on each side of the measuring chamber resulting in a final concentration of 10^{-8} M. By means of impedance spectroscopy as an integral method, peptide insertion and channel activity was followed. Here, a nano-BLM has been chosen that was not defect-free in order to be able to monitor the membrane resistance by impedance spectroscopy in the observed frequency range. Even though the nano-BLM was not defect-free, an increase in ion conductance was clearly observed (Fig. 37).

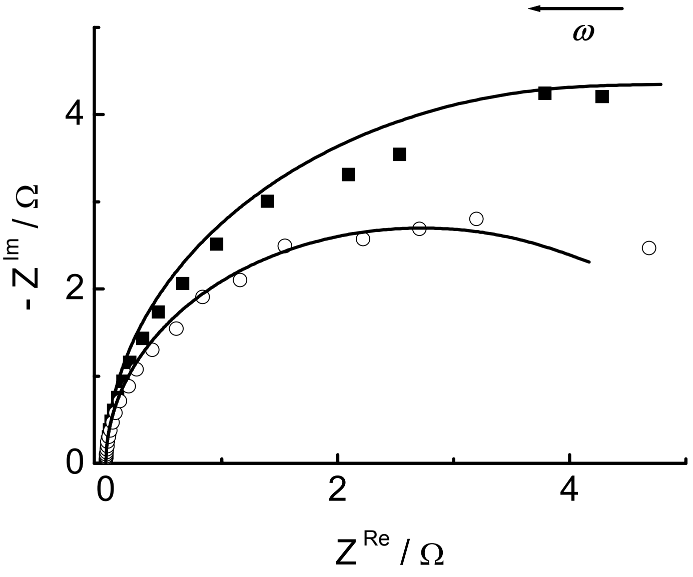

FIGURE 37: Impedance spectra of a nano-BLM bathed in 0.1 M Na_2SO_4 recorded in a frequency range of 10^{-1}-10^{6} Hz before (■) and after (○) gramicidin addition to the *cis* and *trans* compartment. The final gramicidin concentration was 10^{-8} M. After 10 minutes incubation time, the membrane resistance was dropped by more than $3 \cdot 10^{6}$ Ω from $R_m = 8.73 \cdot 10^{6}$ Ω to $R_m = 5.45 \cdot 10^{6}$ Ω. The solid lines are the results of the fitting procedure with the equivalent circuit shown in Fig. 20.

Within 10 minutes after addition of the peptide the membrane resistance was decreased from R_m = 8.73 MΩ to 5.45 MΩ. The membrane capacitance remained constant with a value of 13.1 nF.

4.4.2 Single channel recordings of ion channels integrated in pore-suspending lipid bilayers

Single channel events are characterized by discrete transitions (current steps) between a closed (C) and open (O) state.

4.4.2.1 Single channel recordings of gramicidin in nano-BLMs

If nano-BLMs have a high membrane resistance in the GΩ regime, they should be ideally suited for low-noise electrical recording of transmembrane ion currents. Here, the general functionality of nano-BLMs was demonstrated using gramicidin as a channel-forming peptide. For single channel measurements, nano-BLMs were bathed on either side in 0.5 M KCl. Application of a holding potential of 70 mV across the bilayer allowed the voltage-driven ion current induced by gramicidin upon its bilayer partition to be measured. A schematic representation of nano-BLMs before and after incorporation of gramicidin monomers is depicted in Fig. 38.

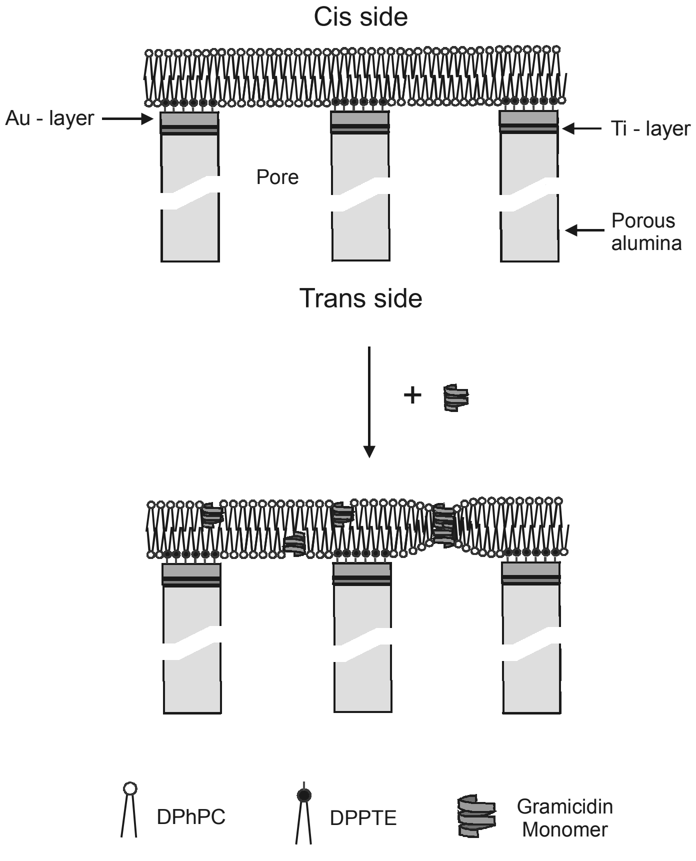

FIGURE 38: Schematic representation of the incorporation of gramicidin monomers in a nano-BLM and the formation of conducting dimers.

In most experiments, gramicidin was added to both, the *cis* and *trans* compartment of the nano-BLM resulting in a final concentration of 10^{-8} M. Single conductance states and multiples of those were observed as shown in the representative current trace in Fig. 39*A* about 10 minutes after gramicidin has been added to the solution.

(*A*)

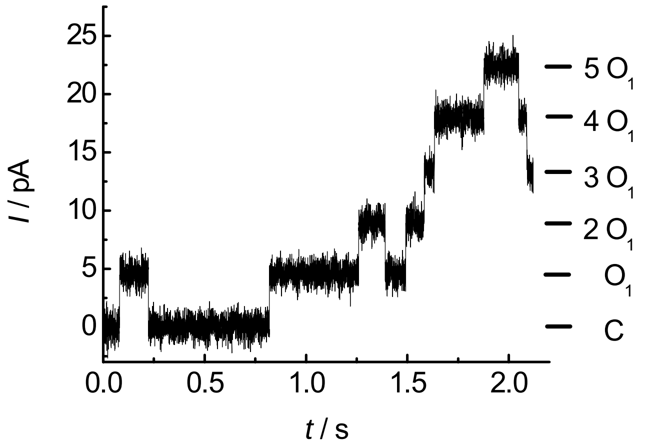

(*B*)

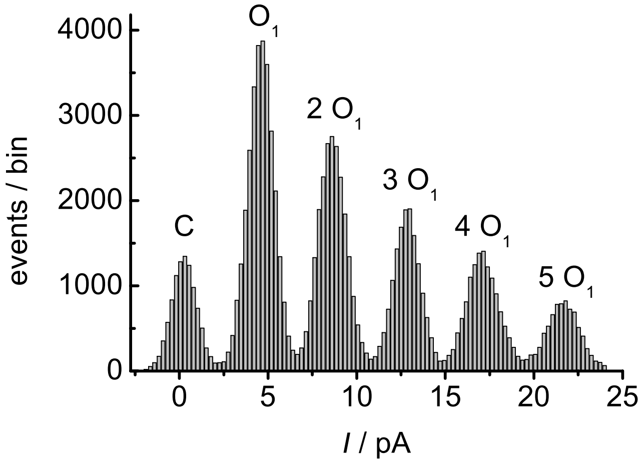

FIGURE 39: (*A*) Current traces of nano-BLMs after addition of gramicidin. The nano-BLM was symmetrically bathed in 0.5 M KCl and a holding potential of $V = 70$ mV was applied. Data were filtered at 1 kHz. Single and multi channel openings up to the 5th opening level (5 O_1) were recorded: C = 0.25 pA; O_1 = 4.35 pA; $2O_1$ = 8.35 pA; $3O_1$ = 12.61 pA; $4O_1$ = 16.77 pA; $5O_1$ = 21.45 pA. (*B*) Corresponding current amplitude histogram.

If gramicidin was added only to the *cis* side, the first conductance events were observed only after 1 hour. The statistical distribution of conductance states is shown in the histogram analysis in Fig. 39*B*. Single channel conductance states (O_1) as well as multiples of those with distinct conductance states up to the 5th opening level (5 O_1) were recorded. A single open state O_1 exhibits a current flow of (4.2 ± 0.15) pA, which translates in a gated conductance state of (60 ± 2) pS. Using the same conditions, conductance measurements were also carried out in 0.5 M CsCl solution resulting in a slightly increased mean conductance of (76 ± 5) pS compared to that obtained in 0.5 M KCl solution. In 0.5 M LiCl, only single channel openings (O_1) were observed, which occurred rather rarely with a mean conductance of (11 ± 2) pS.

Interestingly, the larger area of A = 7 mm^2 of the nano-BLM compared to a classical BLM with a typical area of A = 1 mm^2 does not influence the sensitivity of the measurement. The noise level is in the same range and is typically 2 pA (Fig. 39*B*) for the closed state. Thus, the experiment clearly demonstrates the applicability of nano-BLMs for single channel recordings.

4.4.2.2 Single channel recordings of synthetic Vpu$_{1\text{-}32}$ in micro-BLMs and porous matrix-supported BLMs

Micro-BLMs and porous matrix-supported BLMs, respectively are in principle well suited to studies of ion channel conductance. The aim of this study was to elucidate the influence of the self-assembled DPPTE-monolayer on channel activity.

First, micro-BLMs were utilized to investigate the channel activity of purified synthetic Vpu$_{1\text{-}32}$ comprising the transmembrane segment of Vpu. The peptide dissolved in trifluoroethanol was added to the buffer solution of the *cis*-chamber after a stable baseline was monitored. Channel events were mostly observed shortly after peptide addition, indicating its insertion into the micro-BLMs. Channel activity was observed for fourteen individual bilayer preparations. Shortly after peptide addition, the most frequently observed single channel openings of synthetic Vpu$_{1\text{-}32}$ displayed a conductance of (12 ± 3) pS at a holding potential of 50 mV in 5 mM Hepes, 0.5 M KCl, pH 7.4 (Fig. 40*A*). The current trace presented in Fig. 40*B* was monitored 3 hours after Vpu$_{1\text{-}32}$ addition. Distinct rectangular-shaped multi channel recordings with equally spaced conductance levels are discernable reflecting the simultaneous opening of up to 3 single channels exhibiting the similar conductance level. Each single open state displays a current flow of (0.71 ± 0.19) pA at a potential of 20 mV, which translates into a conductance state of (34 ± 9) pS. Fig. 40*C* shows a corresponding histogram analysis with four Gaussian distributions, which are attributed to the closed and three multiples of the opening state O_1. Also non-equally spaced conductance levels with 28 pS and 40 pS, respectively, were recorded (Fig. 40*D*), occurring coincidently and independently around 2 hours after the first channel events.

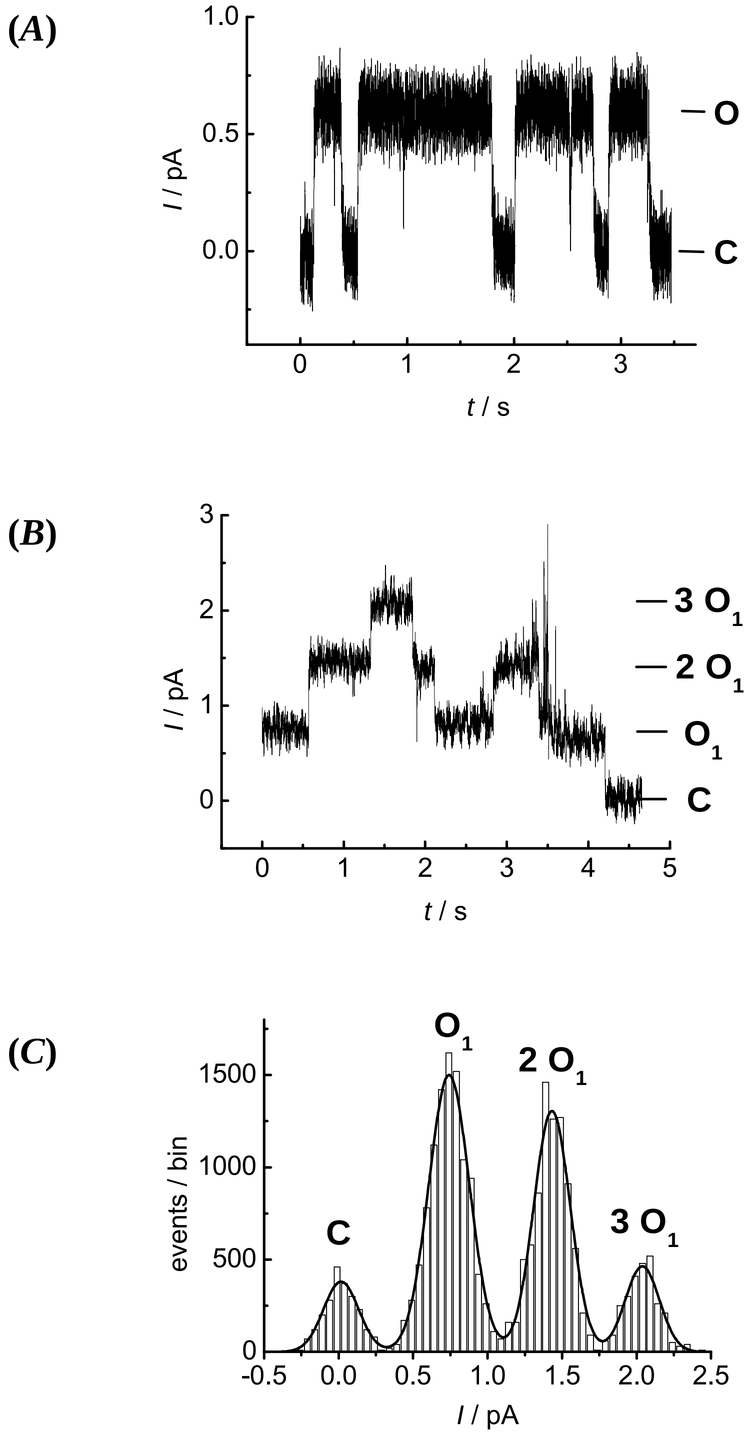

(*D*)

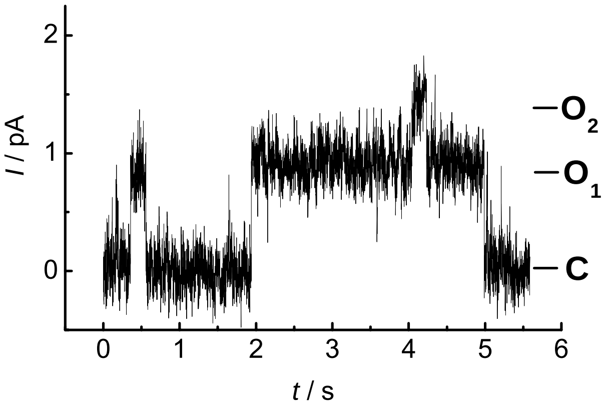

FIGURE 40: Channel recordings from synthetic transmembrane segments of Vpu reconstituted into micro-BLMs based on silicon macropores. Currents were recorded in symmetric 5 mM Hepes, 0.5 M KCl, pH 7.4. The solid line labelled with C indicates the current of the closed state, while O indicates that of the open states. In (*A*), a segment of a continuous recording, observed shortly after peptide addition to the buffer solution, illustrates the occurrence of the 12 pS channel applying a holding potential of 50 mV. The current trace shown in (*B*) was observed at a voltage of 20 mV approximately 3 hours after the first channel openings and displays multi channel openings with a similar distinct conductance state of 34 pS up to the third opening state. (*C*) Current histogram and Gaussian fits for multi channel recordings. (*D*) represents a current trace of two different conductance states of 28 pS and 40 pS, respectively, occurring at a voltage of 50 mV approximately 2 hours after peptide addition.

To investigate the influence of the first chemisorbed DPPTE-monolayer of the micro-BLMs on Vpu channel activity, porous matrix-supported BLMs formed without any functionalization were used for single channel recordings. Peptide was added to the buffer solution, and channel events were detected shortly after peptide addition. First, current traces were observed, which indicate a single channel undergoing transitions between a closed (C) and two open (O) states after applying a voltage of 50 mV (Fig. 41*A*). The statistical distribution of current states is shown in the histogram analysis in Fig. 41*B*. Two discrete channel openings with a conductance of 7.8 pS and 12.4 pS, respectively were calculated, and these occurred initially with almost equal frequency, but were considerably less frequently observed as the closed state. Already after a short incubation time, single channel events could not be resolved unambiguously anymore but rather noisy current traces were recorded at a holding potential of 50 mV (Fig. 41*C*). Although the histograms are not well resolved (data not shown) conductance levels of 12.2 pS, 29.6 pS, 53.0 pS, 168.4 pS, 291.6 pS and 430.4 pS could be assigned to the noisy openings even.

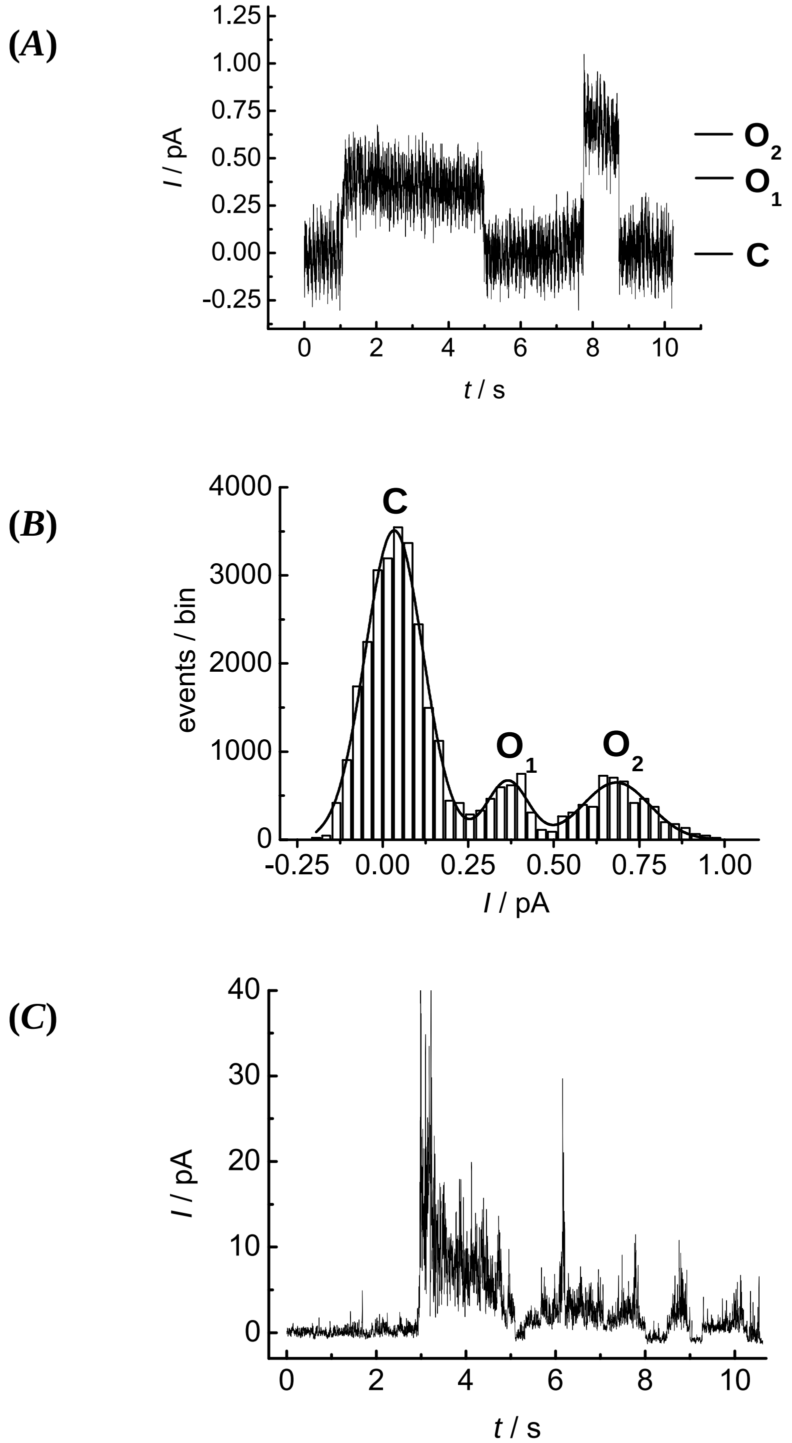

FIGURE 41: Channel recordings from synthetic transmembrane segments of Vpu reconstituted into porous matrix-supported BLMs based on silicon macropores. Short segments of continuous channel activity, recorded at a holding potential of 50 mV, were selected to illustrate the occurrence of channel conductance. The current trace in (*A*) displays a Vpu single channel undergoing transitions between the closed and two open states with conductance levels of 7.8 pS and 12.4 pS shortly after peptide addition to the buffer solution. (*B*) Current histogram and Gaussian fits of the channel events. In (*C*) a rather noisy current trace with conductance levels of 12.2 pS, 29.6 pS 53.0 pS, 168.4 pS, 291.6 pS and 430.4 pS is shown. This pattern of channel activity reproducibly occurred shortly after the first channel events.

Inhibition of Vpu channel activity by amiloride derivatives

It has been shown that amiloride derivatives depress ion channel activity of full-length Vpu reconstituted in classical BLMs [88]. The binding site for the inhibitors has been suggested to be located in the N-terminal transmembrane domain of Vpu [143]. The inhibitory effects of 5-(N,N-hexamethylene) amiloride (HMA), 5-(N,N-dimethyl) amiloride (DMA) and amiloride on the channel activity of Vpu reconstituted in micro-BLMs are compared in this study (Fig. 42). The addition of an aqueous solution of HMA to the *cis* and *trans* chambers with a final concentration of 100 µM resulted in complete inhibition of $\mathrm{Vpu}_{1\text{-}32}$ single channel activity after (10 ± 7) min ($n = 2$) (Fig. 42*A*). Single channel events were suppressed and the current flow returned to the baseline level corresponding to the closed state C. Inhibition of single channel activity was also found for DMA within the same time interval ($n = 1$), while amiloride itself with a final concentration of 100 µM in 5 mM Hepes, 0.5 M NaCl, pH 7.4 and a holding potential of 50 mV did not inhibit the channel activity of Vpu ($n = 2$). The inhibiting effects of the amiloride derivatives are summarized in Fig. 42*B*.

(*A*)

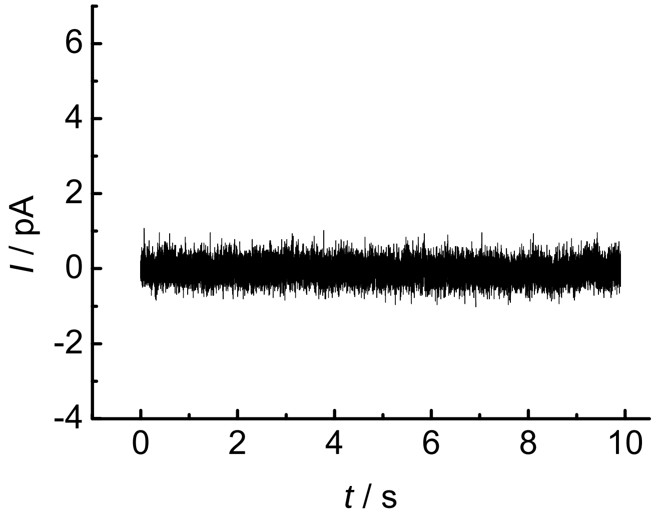

(*B*)

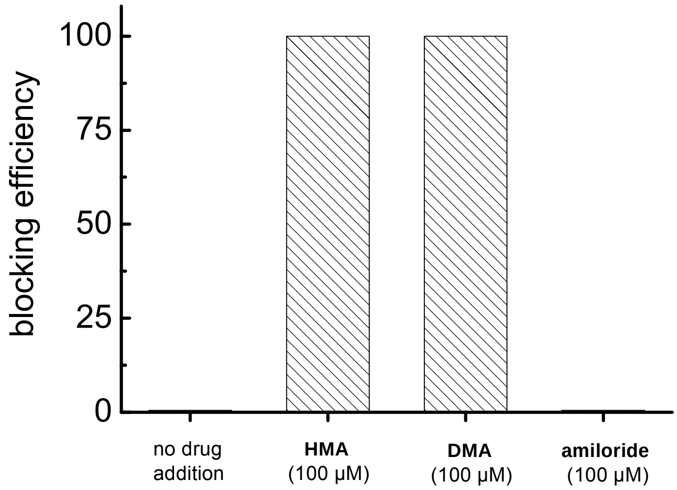

FIGURE 42: The current trace in (*A*) displays the result of Vpu channel inhibition by HMA. (*B*) Inhibiting effects of HMA, DMA and amiloride on Vpu channel activity. All experiments were performed using micro-BLMs in 5 mM Hepes, 0.5 M NaCl, pH 7.4 at a holding potential of $V = 50$ mV and a final drug concentration of 100 µM in both compartments.

4.4.2.3 Single channel recordings of alamethicin in nano-BLMs and porous matrix-supported BLMs

Alamethicin is known as a peptide that self-integrates into bilayers and forms voltage-gated ion channels of defined conductances by oligomerization. Alamethicin monomers were integrated into nano-BLMs bathed on either side in 0.5 M KCl while applying a holding potential of 70 mV after peptide addition to the *cis* side from an ethanolic solution resulting in a final concentration of approximately 10^{-7} M. The voltage-dependent activation of single alamethicin channels with up to five conductance states was observed (Figs. 43*A*/*B*).

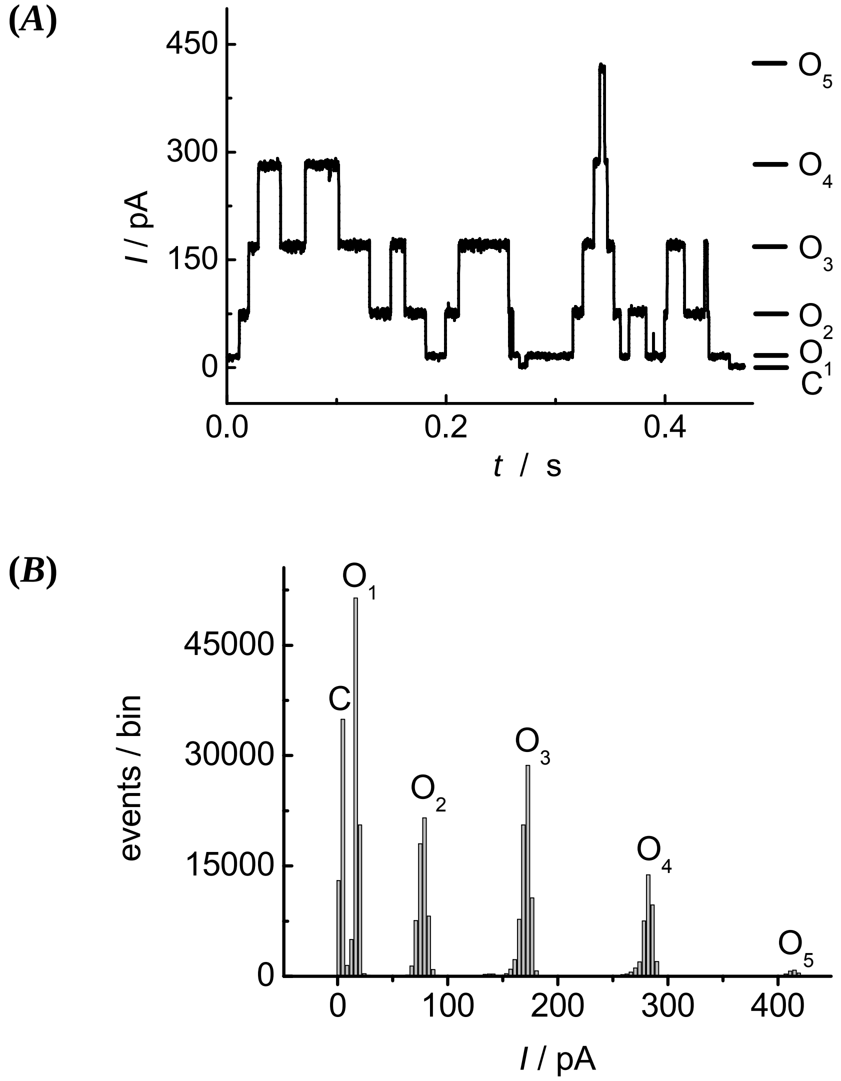

FIGURE 43: (*A*) Representative current trace showing single pore fluctuations induced by alamethicin. The nano-BLM was symmetrically bathed in 0.5 M KCl and a holding potential of $V = 70$ mV was applied. Data were filtered at 1 kHz. The whole burst of fluctuations is due to a single pore event, fluctuating between conductance levels O_1-O_5. O_1 = 16.4 pA; O_2 = 79.1 pA; O_3 = 171.7 pA; O_4 = 281.6 pA; O_5 = 415.2 pA. C = 3.0 pA reflects the current baseline with the channel closed. (*B*) Corresponding current amplitude histogram.

Induced by the applied positive potential, alamethicin channels appear as multilevel current bursts rising from the background current of <2 pA (closed state C) to conducting states of 420 pA (open state O_5). The pore can adopt several electrically distinct states, which are defined by the number of monomers making up the pore forming aggregate. Discrete conductance states up to the 5th conductance level (O_5) can be clearly resolved ranging between 0.2-6 nS. The lower conductance states occurred more frequently. Each change in the conductance state is due to the association or dissociation of an alamethicin monomer to an existing aggregate. Once an initial small channel has been formed, the conductance increases fast and in a stepwise manner. No notable channel activity of alamethicin was observed applying electrical potentials between -30 mV and +20 mV indicating the voltage-gating nature of alamethicin channels.

Alamethicin peptides were also inserted into porous matrix-supported BLMs based on porous silicon with pore sizes of 1 µm. The current trace in Fig. 44 recorded 15 minutes after the first single channel events, shows channel activity induced by alamethicin after incorporation in porous matrix-supported BLMs while applying a holding potential of $V = 20$ mV.

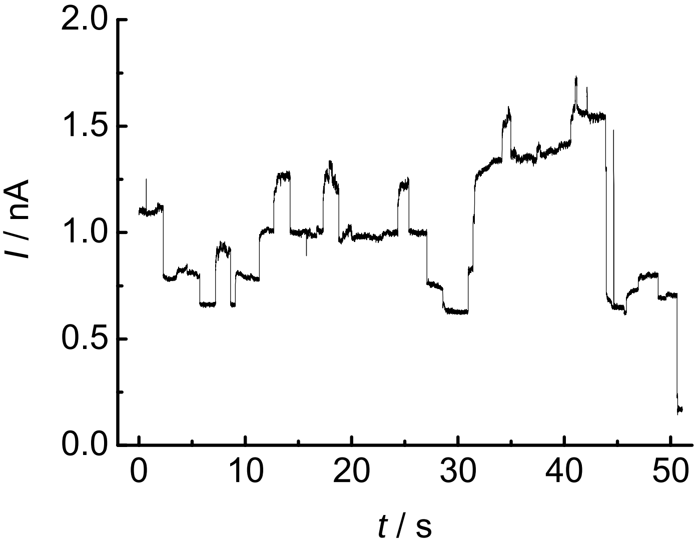

FIGURE 44: Alamethicin channel recordings, recorded 15 minutes after the insertion of the first monomers into a porous matrix-supported BLM bathed in 0.5 M KCl. A holding potential of $V = 20$ mV was applied. The trace presents partially clearly-resolved current fluctuations (larger and smaller ones) that could not longer be assigned to distinct conductance levels. The closed state exhibited a leakage current flow of 1 pA.

Besides discret single pore fluctuations shortly after peptide addition to the buffer solution (data not shown), high conductance levels were recorded due to the uptake of additional alamethicin monomers to the oligomeric bundles. It was no longer possible to address the current steps to distinct conductance levels. Large conductance jumps arise coincidently with smaller fluctuations, indicating the contribution of several conducting alamethicin bundles to the overall current flow. A current flow up to 2 nA through the conducting bundles was achieved without destruction of the membrane. According to the estimation that an alamethicin bundle fluctuates between conductance levels up to a current flow of 700 pA, around 3-7 alamethicin bundles may be simultaneously opened.

5 DISCUSSION

The aim of this work was to obtain artificial membran systems that are attached to a solid support so that they can be applied in chip technology with the future perspective to obtain high-throughput screening (HTS) assays and which exhibit high membrane resistances to perform single ion channel measurements. As solid supported membranes (SSMs) on the one hand are well suited for chip-based biosensors and black lipid membranes (BLMs) on the other hand exhibit high membrane resistances to allow for single channel recordings, the advantages of both membrane systems were tried to be combined in one. To support and stabilize a lipid bilayer while part of it was freestanding, highly ordered porous alumina and macroporous silicon substrates with pore sizes in the nano- and micrometer range were chosen. The pore-suspending lipid bilayers formed by the painting technique were referred to as nano-BLMs, micro-BLMs and porous matrix-supported BLMs. Solvent-free pore-suspending lipid bilayers were formed by spreading and fusion of thiolipid-containing vesicles.

5.1 Choice of porous substrates

The minimal requirement for an ion channel sensor is a small aperture in an insulating material that separates two electrolyte-containing compartments. Key requirements for supports are chemical, mechanical and electrical stability, low surface roughness and adjustable pore sizes and arrangement.

Hexagonally ordered pore arrays of billions of pores per square centimeter were produced by different etch procedures. These porous matrices exhibited pore diameters of (55 ± 8) nm, (280 ± 45) nm and (1.0 ± 0.1) µm and were used as supports for lipid bilayers. The porous substrates differ in their material – alumina and silicon.

Porous alumina with pore sizes of 55 nm and a porosity of 60 % ($4 \cdot 10^{10}$ pores/cm^2) was the result of the anodization of aluminum in oxalic acid solution at a voltage of 40 V. Pore arrays with pore sizes of 280 nm and a porosity of 33 % ($2 \cdot 10^9$ pores/cm^2) were also formed by anodization of aluminum, but in phosphoric acid solution applying a potential of 160 V. As the pore growth in alumina is as yet limited to a maximal pore size of around 300 nm [113], pore arrays with pore diameters of 1 μm and a porosity of 22 % (10^8 pores/cm^2) were etched in n-type silicon of (100)-orientation by a photo-electrochemical etch process conducted in hydrofluoric acid at a voltage of 2.7 V. After removal of the bulk aluminum and silicon at the lower surface followed by pore bottom opening, the pore arrays were continuously open and ready to use. The pore sizes are adjustable within a range of 20-300 nm for porous alumina [112-115, 117, 118, 144] and 0.7-3.5 μm for macroporous silicon [104, 120, 124, 126, 145, 146]. Depending on the pore depth, the pore arrays exhibit a good mechanical stability. Porous alumina substrates were used with a thickness of 150-200 μm while for porous silicon substrates, a thickness of 50 μm was sufficient in order to ensure mechanical stability, especially when mounting and fixing the porous substrate in the Teflon cell. Impedance spectroscopy revealed that the sieve-like alumina and silicon substrates are electrically inert in aqueous solution.

In recent years much research effort has been spent on the formation of highly insulating lipid bilayers on single pores in micromachined supports including the development of these supports. Fertig et al. fabricated an ′on-chip-pore′ in glass with a diameter in the low micrometer range using the ion-track etching technique, i.e. by irradiation of the glass chip with a single heavy ion and subsequent wet track etching [45]. Pantoja et al. micromachined single pores of 50-200 μm in diameter in silicon [52]. The fabrication of micropores with diameters from 2-800 μm in films of amorphous Teflon (Teflon AF) was reported by Mayer et al. [47]. There exists a broad variety of single apertures in different materials (glass, silicon, Teflon) with pore sizes of 1-800 μm in diameter used as supports for lipid bilayers. However, to the best of my knowledge no lipid bilayers suspending pores with pore sizes in the nano- and micrometer range have been reported and no lipid bilayers suspending pore arrays of millions of pores. Only recently, Mayer et al. reported on the preparation of planar lipid bilayers covering three pores of equal diameter (120 μm) to test for the possibility to form lipid bilayers in parallel [47]. Favero et al. described the formation of mixed hybrid lipid bilayers on randomly distributed pores of around 1 μm in diameter in polycarbonate filters exhibiting a relatively high surface roughness [53, 54]. For automation and parallelization of channel recordings required in drug screening assays, pore-suspending lipid bilayers based on highly ordered porous substrates with uniform pore sizes are more desirable. Thus, taking all criteria into account, hexagonally ordered porous alumina and silicon substrates of cylindrical-shaped pores with pore sizes in the nano- and micrometer range combine these requirements and are supposed to be best suited as substrates for chip-based high-throughput screening assays based on membrane ion channels.

5.2 Formation of pore-suspending lipid bilayers by the painting technique

5.2.1 Nano- and micro-BLMs based on prefunctionalized porous substrates

The lower surface of porous alumina and silicon substrates was coated with a thin gold layer. The employed vertical deposition technique (see chapter 3.2.2.1) ensured that only the top surface of the pore rims was covered, while the pore interior was not filled with gold. The selective functionalization of the gold-covered lower surface with hydrophobic monolayers of either 1,2-dipalmitoyl-*sn*-glycero-3-phosphothioethanol or 1-octadecanethiol allowed for the immobilization of lipid bilayers by spreading 1,2-diphytanoyl-*sn*-glycero-3-phosphocholine dissolved in *n*-decane across the porous matrix. The functionalization of the gold-covered pore rims with the chemisorbed hydrophobic monolayer favors the formation of pore-suspending lipid bilayers rather than a complete membrane coverage inside the pores as it was reported by Bourdillon and coworkers [147]. If the surface was not hydrophobic, lipid bilayer formation was not observed on the gold-covered pore rims.

Properties of nano-BLMs

Membrane capacitance

Nano-BLMs were formed on porous alumina with pore diameters of 55 and 280 nm. Impedance data were analyzed using a simple equivalent circuit composed of a parallel *RC*-circuit that describes the electrical behavior of a lipid membrane. Based on this model, a specific mean membrane capacitance of C_m^A = (0.65 ± 0.20) µF/cm^2

(n = 15) was obtained for nano-BLMs onto the prefunctionalized porous alumina substrates with pore diameters of 280 nm. This mean capacitance value indicates that single lipid bilayers have been formed on the porous alumina substrates. The specific capacitances are consistent with those reported for classical BLMs formed across an aperture in a Teflon foil, which are typical around 0.5 µF/cm^2 [38, 139], and with capacitance values of lipid bilayers formed across an aperture of a micromachined support. Lipid membranes suspending single apertures of 10-500 µm in diameter micromachined in silicon or glass chips were reported to exhibit specific capacitances of 0.3-1.1 µF/cm^2 [45, 48, 50, 52]. Since impedance studies indicate that the current exclusively flows through the pores, the specific membrane capacitances of nano-BLMs were calculated using the estimated porous area obtained from SEM images. Due to the error of the determined area the error of the specific capacitance and resistance values is estimated to be 10 %. Within this error, the determined capacitances are still in the same range as those reported for classical BLM preparations.

Membrane resistance

In contrast to C_m, the membrane resistance R_m of nano-BLMs strongly depends on the quality of the preparation and the age of the nano-BLM. Taking the actual area into account, specific membrane resistances of up to $R_m^A = 1.6 \cdot 10^8\ \Omega\ \text{cm}^2$ were obtained for nano-BLMs bathed in 0.5 M KCl solution. For classical BLMs unbuffered in 0.1 M KCl electrolyte solutions, specific resistances of about $10^8\ \Omega\ \text{cm}^2$ were reported [38, 139]. Cheng et al. [48] obtained specific membrane resistances of about $10^7\ \Omega\ \text{cm}^2$ for a lipid bilayer suspending an aperture being 128 µm in diameter, which was micromachined in gold/photoresist. However, for single channel recordings not the specific membrane resistance but the absolute value of the membrane resistance is the decisive parameter. By decreasing the area the resistance is increased. For example, Schmidt et al. [51] reported a membrane resistance exceeding $10^9\ \Omega$ obtained from membranes suspending one single aperture micromachined in a silicon chip with diameters of 0.6-7 µm. The specific resistance is, however, only around 5-400 Ω cm^2. For comparison, specific membrane resistances up to $1.6 \cdot 10^8\ \Omega\ \text{cm}^2$ were obtained on a total porous area of $A = 2.3\ \text{mm}^2$ comprising about 37 million pores each with a mean diameter of 280 nm.

A second interesting point concerning the membrane resistance is its time-dependency. R_m continuously decreases over time (see Fig. 22). This result was unexpected because in the case of traditional BLMs and those more recently described based on apertures manufactured in silicon or glass supports, membrane rupture leading to a complete loss of membrane resistance occurs in one single step. The stability of nano-BLMs exhibiting membrane resistances larger than 1 GΩ was calculated to be (1.5 ± 0.5) days. Even 4 days after formation, a nano-BLM still exhibits specific membrane resistances of $4 \cdot 10^5$ Ω cm^2, which is in the same range as those reported for solid supported membranes. For example, for lipid bilayers immobilized on semiconductor and gold surfaces, Wiegand et al. reported resistances ranging between 10^3-10^5 Ω cm^2 [18], while Purrucker et al. achieved membrane resistances up to 10^6 Ω cm^2 [17]. These solid supported membranes (SSMs) are typically stable for several days. The extraordinary high stability of nano-BLMs appears to be favored by the stabilizing effect of the porous substrate. In comparison, classical freestanding BLMs with pore diameters of 0.1-1 mm typically last not longer than 8 hours [38]. Cheng et al. [48] reported a stability of 5 hours for a lipid membrane suspending an aperture being 128 μm in diameter, while Schmidt et al. [51] obtained a stability of approximately 1 hour for a lipid bilayer suspending a 0.6-7 μm hole in silicon.

From the continuous decrease in membrane resistance led us conclude that in nano-BLMs, each single membrane covering a pore of the porous alumina matrix ruptures individually leading to the observed continuous decrease in R_m. This would imply that each membrane covering a pore is decoupled from the surrounding ones favored by the quasi-covalently fixed hydrophobic submonolayer on the gold-coated pore rims. This hypothesis is supported by the results obtained from porous matrix-supported BLMs (see chapter 5.2.2).

Studying the diffusion of the charged fluorescent dye 5,6-carboxyfluorescein (CF) through nano-BLMs confirmed that the quality and stability of the membrane decreases continuously over time, without completely collapsing at once. In contrast to the unrestricted diffusion of CF through neat porous alumina, a defect-free nano-BLM inhibits this passage. After 10 hours only a small amount of CF passed the nano-BLM accompanied by a small increase in fluorescence intensity in the *trans* compartment, indicating that the membrane was still intact and almost all pores were covered with a lipid bilayer. A slow, but continuous increase in fluorescence intensity over time supports again the idea that each membrane, covering a single pore, ruptures individually without that the whole nano-BLM collapses in one single step.

The continuous decrease in membrane resistance of nano-BLMs confirmed by impedance data and fluorescence intensity recordings indicates that a defect occurring at one site does not influence the stability of the entire membrane, i.e. a membrane suspending a single pore is decoupled from the others. Thus, scanning probe methods such as scanning ion conductance microscopy exhibiting lateral resolutions in the range of 10-100 nm would allow addressing each membrane-suspended pore individually [148-150]. Then, one would be able to measure on a membrane preparation even if some of the membranes suspending the pores are ruptured.

Properties of micro-BLMs

The pore suspending lipid bilayers termed micro-BLMs were formed by the painting technique based on macroporous silicon with pore diameters of 1 µm. For micro-BLMs, data analysis of impedance spectra revealed a mean specific capacitance of $C_m^A = (0.63 \pm 0.21)$ µF/cm^2, which is consistent with those obtained for classical BLMs and nano-BLMs [38, 139] and clearly indicates that even though the pores are by a factor of 4 larger in the case of macroporous silicon as porous substrate, single lipid bilayers have been formed. To observe single channel events with low noise, high membrane resistances in the GΩ regime are again required. Micro-BLMs exhibit membrane resistances larger than 1 GΩ, which are similar to those obtained for nano-BLMs. A maximum membrane resistance of R_m = 118 GΩ (1.8 GΩ cm^2) was obtained. To establish a membrane system suited for biosensor devices and high-throughput screening assays based on single channel recordings, not only the membrane resistance itself but also long-term stability with respect to the membrane resistance is required. A mean stability of 1 day was obtained for micro-BLMs exhibiting membrane resistances in the GΩ regime while for nano-BLMs suspending pores with pore sizes of 280 nm, a stability of 1.5 days was determined. Obviously, the pore size influences the long-term stability of the membrane. Though only two pore sizes are compared, the tendency seems to be that the smaller the pore diameter, the more long-term stable is the pore-suspending lipid bilayer. Similar to the results obtained for nano-BLMs based on porous alumina substrates, the membrane resistance continuously decreases versus time indicating that not the entire membrane collapses at once but each membrane patch suspending a pore ruptures individually. These observations in addition to those made for nano-BLMs strongly point toward the idea that each membrane suspending a pore is decoupled from the others.

5.2.2 Porous matrix-supported BLMs formed without prefunctionalization of the porous substrate

The question arose whether the immobilization of a lipid bilayer on the porous matrix via the chemisorbed DPPTE-submonolayer on the pore rims influences the electrical parameters of the membrane and its long-term stability. To address this question, lipid bilayers were prepared by simply spreading DPhPC in *n*-decane across porous alumina and macroporous silicon substrates without a prefunctionalization of the lower surface with a gold- and DPPTE-layer. The formation of porous matrix-supported BLMs was only successful based on macroporous silicon substrates and failed for porous alumina substrates. This membrane system was termed porous matrix-supported BLMs. Interestingly, a similar mean specific capacitance of $C_m^A = (0.78 \pm 0.34)\ \mu F/cm^2$ was obtained for porous matrix-supported BLMs from impedance analysis compared to nano- and micro-BLMs. The mean capacitance value is characteristic for the formation of single bilayers on the porous matrix [38, 139]. Membrane resistances were also very similar and were in the GΩ range. The most striking difference between micro-BLMs and porous matrix-supported BLMs was, however, their long-term stability. While for micro-BLMs, the membrane resistance decreased continuously, R_m dropped instantaneously to almost zero at a certain time occurring between 10 min and several hours in case of porous matrix-supported BLMs. The long-term stability of porous matrix-supported BLMs is obviously decreased compared to that of micro-BLMs although both membrane systems are based on macroporous silicon substrates with pore diameters of 1 µm. Both bilayer preparations only differ in the prefunctionalization of the porous substrate surface, i.e. the gold-coating of the top of the pore walls followed by chemisorption of self-assembled DPPTE-monolayers. Thus, the difference in membrane stabilities is attributed to the prefunctionalization of the substrate.

The quasi-covalent attachment of lipid bilayers to the silicon support via DPPTE-submonolayers not only stabilizes the micro-BLM, but also leads to another interesting advantage of micro-BLMs compared to matrix-suppported BLMs. As in case of micro-BLMs the membrane resistance decreases continuously, it is concluded that each membrane-suspended pore is decoupled from the others leading to a membrane system in which each membrane patch ruptures individually. Matrix-supported BLMs, though they might be slightly stabilized by the porous support, rupture in one single event. This collapse in one step has also been observed for conventional BLMs [38] spanning a small hole in a thin Teflon film and for those more recently described by Schmidt et al. [51] and Cheng et al. [48] based on individual apertures manufactured in silicon or glass support. These lipid bilayers suspending a single pore in the micrometer range and exhibiting a maximal stability of 5 hours, completely rupture at once.

In general one can conclude that nano- and micro-BLMs are better suited for long-term-dependent impedance measurements and single channel recordings than porous matrix-supported BLMs because of their reproducibility, reliability and the fact that the membrane resistance decreases continuously over time. As mentioned before, the quasi-covalently attached parts of nano- and micro-BLMs stabilize the entire lipid bilayer.

5.3 Formation of pore-suspending lipid bilayers by vesicle spreading and fusion

The formation of pore-suspending lipid bilayers by vesicle adsorption, spreading and fusion on the porous surface allows in principle the formation of solvent-free lipid bilayers covering porous substrates. The exclusion of the solvent from bilayer preparations is desirable as the solvent may influence the properties of the membrane and the functionality of integrated membrane proteins.

Lipid bilayer formation by chemisorption of thiolipid-containing vesicles

According to the results of Drexler et al. [135], highly ordered porous alumina substrates with pore diameters of 55 nm are suited as supports for solvent-free pore-suspending lipid bilayers formed by vesicle spreading and fusion. However, the heterogeneity of the surface of non-ordered porous alumina substrates resulted in an insufficient formation of lipid bilayers accompanied by bad accordance between data and fit [135].

Selective functionalization of the lower surface of the porous substrate with a thin gold layer and size exclusion of large unilamellar vesicles was supposed to prevent the formation of lipid bilayers within the pores as observed by Marchal et al. [151]. They functionalized the inner pore walls of porous alumina with a self-assembled monolayer of octadecyltrichlorosilane (OTS). Vesicles composed of 1,2-dimyristoyl-*sn*-glycero-3-phosphocholine (50 nm in nominal vesicle diameter) diffused into the pores of the porous alumina substrate with pore diameters of around 200 nm and fused with the inner OTS-treated surface to a bilayer.

As observed by impedance spectroscopy, porous alumina itself is electrically characterized by the resistance of the electrolyte R_{el} as the total current flows through the water-filled pores and not through the pore walls. All changes in the impedance spectrum after incubation of the porous alumina substrate with a thiolipid-containing vesicle suspension are thus attributed to the formation of a pore-suspending lipid bilayer. A change in the impedance spectra was observed, but the data revealed only limited accordance with the model comprising a simple parallel *RC*-element representing the electrical behavior of a planar lipid bilayer. Defects in the lipid bilayer occupied by water account for this deviation. An equivalent circuit accounting for the electrical properties of this imhomogeneous lipid bilayer system was chosen, which is composed of a parallel circuit consisting of a constant phase element and a resistor. Drexler et al. discussed in detail the usability of the constant phase element in circuit modeling, but pointed out its difficulty at the same time [134]. Since n was close to 1, the parameter A_{m} was still viewed as the capacitive behavior of the membrane, as a first approximation, and translated into $C_{\mathrm{m}}^{\mathrm{A}}$ taking the active porous area into account. Specific membrane capacitances of $C_{\mathrm{m}}^{\mathrm{A}} = 2\text{-}10\ \mu\mathrm{F/cm}^2$ were obtained for the best preparations concerning the pore coverage. These values are still much larger than those of common solid supported membranes and also indicate that the membrane preparation leads to defects within the membrane. Wiegand et al. reported membrane capacitances of C_m^A = 0.74-1.12 µF/cm^2 and membrane resistances R_m^A between 10^3-10^5 Ω cm^2 for lipid bilayers, immobilized on semiconductor and gold surfaces [18].

To determine a quality parameter of the formed solvent-free pore-suspending lipid bilayer, the pore coverage Θ was calculated making the following assumptions: The conductance G of the system consists of the conductance of the membrane-suspended porous areas G_m and that of uncovered pores represented by the conductance of the electrolyte solution G_{el}. The membrane resistance R_m was fixed to 1 GΩ, representing a typical resistance of an insulating lipid bilayer, which corresponds to a membrane conductance of 1 nS. Based on these assumptions, a pore coverage of Θ = 90 % was calculated for a pore-suspending lipid bilayer formed by incubation of the porous alumina substrate with DPPTE/DPhPC vesicles, which means that 1 out of 10 pores is uncovered. A potential disturbing factor that inhibits the complete coverage of the alumina matrix might be the arising boundary effects between the lipid bilayer and the sealing ring which borders the active area. The model for the calculation of the pore coverage only considers the porous area. But the alumina matrix consists of a porous part (60 %) and a solid supported part (40 %). It can be assumed that the membrane patches attached to the solid support via chemisorption completely cover the alumina pore racks. If this were the case, the lipid bilayer formed by fusion of DPPTE/DPhPC vesicles would cover around 95 % of the alumina matrix. Drexler et al. obtained a specific membrane capacitance of C_m^A = 2.6 µF/cm^2 and a specific membrane resistance of R_m^A = 43 kΩ cm^2 after incubation of highly ordered porous alumina substrates with vesicle suspensions (400 nm in nominal vesicle diameter) of a DPPTE/DOPC lipid mixture (72/28 wt %) and estimated that at least 65 % of the surface was covered by a lipid bilayer [134, 135].

The pore coverage of lipid bilayers was improved by optimization of several parameters such as lipid composition, incubation time, incubation temperature. The best pore coverage was obtained by spreading and fusion of DPPTE/DPhPC vesicles (60/40 wt %, 100 nm in nominal vesicle size) by using an incubation temperature above the main phase transition temperature of the lipid mixture. The addition of cholesterol to the lipid mixture did not result in a significant increase in pore coverage. An incubation time between 4-12 hours favored the formation of pore-suspending lipid bilayers containing fewer defects.

Since defect-free pore-suspending lipid bilayers with membrane resistances exceeding 1 GΩ were not obtained by vesicle spreading and fusion, single channel recordings were not performed.

5.4 Ion channel insertion in pore-suspending lipid bilayers

5.4.1 The dimeric gramicidin channel in nano-BLMs

The biomimetic properties and suitability of nano-BLMs for the development of biosensors have been analyzed and evaluated by monitoring the channel activity of gramicidin D. Gramicidin is only active if the membrane is as thin as one lipid bilayer. The formation of the conducting dimer was followed by means of impedance spectroscopy and single channel recordings.

Impedance analysis clearly demonstrated that the membrane resistance is decreased due to incorporation of conducting gramicidin dimers into nano-BLMs bathed in 0.1 M Na_2SO_4. Similar decreases in membrane resistances observed by means of impedance spectroscopy were already reported for solid supported membranes [95, 96, 152, 153]. Impedance spectroscopy is a versatile method to investigate ion channel activity. A decrease in membrane resistance can be observed even though the pore-suspending lipid bilayer is not defect-free and therefore does not exhibit membrane resistances in the GΩ regime necessary for single channel recordings.

For solid supported membranes immobilized on a polarizable electrode it is not feasible to monitor single channel events after insertion of a membrane active channel peptide. This can, however, be realized by using nano-BLMs. Bathed in 0.5 M KCl electrolyte solution, the different opening states of individual gramicidin channels

(O_1-$5O_1$) were clearly discernable corroborating the idea that single lipid bilayers have been formed on the porous support as it is well established that gramicidin ion channels can only be observed in single lipid bilayers. The mean conductance of around 60 pS applying a holding potential of 70 mV is in the conductance range reported by others [70, 75, 76, 154, 155]. No channel activity was observed before adding the peptide to the solution. Bamberg et al. [154] as well as Hladky and Haydon [75] reported on a gramicidin conductance of 50 pS in glyceryl-monooleate membranes bathed in 1 M KCl at a potential of 100 mV and a temperature of 23 °C.

The specificity of gramicidin ion channels was proven by using CsCl and LiCl in addition to KCl as bathing solution. The larger conductance in case of Cs^+ cations and the observed decrease in conductance for Li^+ cations are in line with the reported selectivity of gramicidin channels for monovalent cations, which is reported to be $Cs^+ > K^+ >> Li^+$ (sequence of conductance) [70] and confirms that the observed single channel events are the result of gramicidin insertion.

5.4.2 Ion channel activity of synthetic peptide $Vpu_{1\text{-}32}$ integrated in micro-BLMs and porous matrix-supported BLMs

Despite the difference in long-term stability, both membrane systems based on macroporous silicon, micro-BLMs as well as matrix-supported BLMs, allow in principle for single channel recordings and might bear the potential to be used for chip-based ion channel sensor devices. In order to elucidate the influence of the quasi-covalently attached hydrophobic DPPTE-monolayer on the gold-covered pore walls of the macroporous silicon, the channel activity of $Vpu_{1\text{-}32}$ was compared for both membrane preparations.

Channel activity of $Vpu_{1\text{-}32}$ in micro-BLMs

The suitability of micro-BLMs has been proven by investigating the channel activity of the synthetic peptide $Vpu_{1\text{-}32}$ comprising the transmembrane segment of the integral membrane protein Vpu encoded by HIV-1. Over the past years it has been established that the transmembrane α-helix (residues 8-25) of the Vpu polypeptide exhibits ion channel activity [85-92, 156-158]. All data were acquired from single channel recordings on classical planar lipid bilayers after reconstitution of full-length Vpu or truncated versions (Vpu_{1-27}, Vpu_{2-30+}, Vpu_{2-37}, Vpu_{2-51}) of the protein [85-92, 156-158].

By means of the newly established micro-BLM system, single and multi channel openings of heterogeneous conductance were recorded in a highly resolved manner. While the most frequent conductance state of (12 ± 3) pS in 5 mM Hepes, 0.5 M KCl, pH 7.4 was largely observed as distinct single channel openings, in some current traces it occurred together with some other conductance states. The second most frequently observed conductance state was (34 ± 9) pS. Ma et al. [158] reported a single channel conductance of (12 ± 2) pS as the most frequently observed opening for Vpu_{2-37} under similar conditions using classical BLMs. The conductance level of 12 pS is also consistent with experiments carried out by Ewart et al. [88] and Schubert et al. [90] using Vpu constructs including the transmembrane domain. The observed 12 pS conductance state is also observed for full-length Vpu with the most frequently occurring conductance of 12 pS, 22 pS [85, 87] and 30 pS [157] recorded in 0.5 M KCl. The precise number of Vpu monomers participating in the Vpu channel is not known yet although it has been modeled as a tetramer, pentamer and hexamer [159-161]. Computational [160, 161] and experimental evidence [159] is in favor of a pentameric model. Montal et al. [85, 159] suggest a structure composed of a water-filled pentameric helix bundle arising from the self-assembly of Vpu monomers to be compatible with the 12 pS conductance state.

The results obtained for Vpu channel activity indicate that micro-BLMs are well suited for single channel studies. Moreover, they show advantages over classical BLMs and lipid bilayers suspending single apertures in micromachined supports. Using micro-BLMs, multi channel openings were resolved with identical and different single conductance levels even hours after peptide, dissolved in trifluoroethanol, had been added in a reproducible manner. It appears that the chemisorbed DPPTE-monolayer reduces the probability of Vpu peptide insertion and influences the lateral mobility of integrated peptides.

Channel activity of Vpu_{1-32} in porous matrix-supported BLMs

To address the question, if Vpu peptide insertion and the lateral mobility of the peptide monomers in the membrane are influenced by the partial anchoring of the lipid bilayer to the porous substrate via the DPPTE-monolayer, single channel recordings were performed on pore-suspending lipid bilayers without functionalization, termed porous matrix-supported BLMs. In contrast to micro-BLMs, single channel events could not be observed in case of porous matrix-supported BLMs already approximately 30 min after peptide addition. Instead, large current bursts became visible, whose magnitudes increased over time presumably due to an increased number of inserted Vpu peptides. Such large conductance bursts of up to 430 pS were also reported by Ewart et al. [88, 89]. The large conductance levels might be a result of many simultaneously opened channels, or the association of a large number of Vpu monomers to large channel aggregates, respectively. An explanation for this observation may be found in the lateral mobility of incorporated Vpu monomers, which is hindered by the hybrid membrane fixed to the gold-covered surface via chemisorption of the thiolipid DPPTE in case of micro-BLMs. This would disfavor the formation of large oligomeric bundles of Vpu monomers, and as a consequence noisy multi channel bursts due to oligomerization by large conducting channel aggregates as observed in matrix-supported BLMs become unlikely.

The channel recordings performed almost immediately after incorporation of synthetic Vpu_{1-32} peptides in porous matrix-supported BLMs displayed conductance occasionally as low as 7.8 pS besides the typically occurring conductance of 12.4 pS. The latter value is similar to values reported earlier on the transmembrane domain reconstituted into lipid bilayers [90]. Small conductance values obtained from amphiphatic peptides and proteins are normal due to the lose assembly process and the dynamics of the lipid bilayer. It is conceivable that the low conductance level of 7.8 pS may be due to the channel formation process, since it is not observed at a later stage of the recordings.

The data of single channel recordings indicated that the channel activity of Vpu_{1-32} is influenced by the employed membrane system. It is supposed that the functionalization of the gold-coated porous substrate with chemisorbed DPPTE-monolayers hinders the peptide insertion and the lateral mobility of incorporated peptides, and thus enables longer lasting single channel recordings.

Inhibition of Vpu-induced ion channel activity by amiloride derivatives

Three different amilorides have been analyzed with respect to their potency to inhibit Vpu-induced ion channel activity to verify that the observed events result from specific Vpu ion channels and to analyze if micro-BLMs may be used for the development of high-throughput screening assays for potential drugs. Consistent with previous studies, amiloride does not influence Vpu channel activity considerably in a concentration of 100 µM. However, 5-(*N*,*N*-hexamethylene) amiloride and 5-(*N*,*N*-dimethyl) amiloride differing from amiloride only in the N-substituent at position 5 of the pyrazine ring fully suppress channel activity in a concentration of 100 µM. The hydrophobic substituents appear to be of particular importance for the inhibition of Vpu channel. Differences in the blocking sensitivity of HMA and DMA were not observed for the investigated concentration of 100 µM.

5.4.3 The voltage-gated alamethicin bundle integrated in nano-BLMs and porous matrix-supported BLMs

In contrast to gramicidin D and Vpu, which insert into bilayers without the application of a potential, a potential difference across the bilayer needs to be applied for the insertion of the peptide alamethicin. The different conductance levels are explained by the scenario that the peptide self-assembles into an α-helical bundle forming a pore. The number of helices that participate in the pore forming process vary between 4-11 [80] leading to different pore sizes and thus, to different conductance levels. The obtained conductance values of up to 0.4 nA were induced by alamethicin pore formation in nano-BLMs and represent typical single pore fluctuations. These conductance states are in reasonably good agreement with data reported in literature [77, 80, 81, 162]. Bezrukov and Vodyanoy reported on alamethicin current bursts rising from the background current of <1 pA to conducting states of up to 0.5 nA [78].

Alamethicin helices were also integrated in porous matrix-supported BLMs while applying a potential. Distinct conductance states up to an ion flux of 2 nA were clearly resolved without that the membrane ruptured. More than one alamethicin bundle opened simultaneously already after short incubation times. In comparison to nano-BLMs, it is supposed that more peptide monomers insert into porous matrix-supported BLMs and diffuse unhindered through the lipid bilayer enabling the formation of more and larger alamethicin bundles.

6 SUMMARY AND OUTLOOK

Ion channels are one of the main drug targets and are in the focus of various membrane biosensor applications and drug screening assays. The aim of this thesis was to develop and characterize a novel membrane system suspending highly ordered porous substrates. This hybrid membrane system was supposed to combine the advantages of freestanding and solid supported lipid membranes. While part of the lipid bilayer anchored to the surface of the porous matrix resembles a solid supported membrane, the pore-suspending parts can be viewed as freestanding lipid membranes.

Hexagonally ordered porous alumina and macroporous silicon substrates with pore diameters in the nano- and micrometer range were fabricated by different etching procedures and characterized in detail by impedance spectroscopy and scanning electron microscopy. These highly ordered sieve-like pore arrays of billions of pores per square centimeter were used as supports for lipid bilayer immobilization.

Two different methods were successfully developed to obtain pore-suspending lipid bilayers based on these porous substrates: (1) a painting technique and (2) a technique based on vesicle spreading and fusion:

(1) Painting technique: In order to ensure that the prepared bilayers suspend the pores and do not cover the inner pore walls, the top of the pore columns was selectively functionalized by coating with a thin gold layer followed by chemisorption of either 1,2-dipalmitoyl-*sn*-glycero-3-phosphothioethanol or 1-octadecanethiol. Lipid bilayers suspending the pores were obtained by painting 1,2-diphytanoyl-*sn*-glycero-3-phosphocholine dissolved in *n*-decane across the porous matrix. The membrane formation process was followed by means of electrical impedance spectroscopy, and membrane specific parameters were extracted from the impedance data by modeling the electrical behavior of these membrane systems by an adequate equivalent circuit consisting of a simple parallel $R_m C_m$-element. Specific membrane capacitances of $C_m^A = 0.7\ \mu F/cm^2$ were calculated indicating the formation of single lipid bilayers. Suspended lipid bilayers on porous alumina, which we termed nano-black lipid membranes (nano-BLMs) and those suspending macroporous silicon substrates, termed micro-BLMs, both exhibited membrane resistances in the gigaohm regime allowing for single ion channel recordings and an extraordinary high long-term stability. In contrast to

classical BLMs, which rupture in one single step, the membrane resistance of nano- and micro-BLMs decreases continuously, which was attributed to the fact that each membrane suspending a single pore can rupture individually due to the separation of the freestanding bilayer parts by the chemisorbed hydrophobic submonolayer. To prove this hypothesis porous matrix-supported BLMs were formed by painting 1,2-diphytanoyl-*sn*-glycero-3-phosphocholine across macroporous silicon substrates without pre-functionalization. Indeed, without the chemisorbed submonolayer, these matrix-supported lipid bilayers resemble classical BLMs. Though they exhibit typical membrane specific parameters, they rupture in one single event.

(2) Vesicle spreading and fusion: The formation of solvent-free pore-suspending lipid bilayers was achieved by spreading and fusion of thiolipid-containing large unilamellar vesicles on porous alumina substrates, which were covered on top of the pore columns with a thin gold layer. Impedance analysis revealed that these membranes were, however, not defect-free and thus, were as yet not suited for single channel recordings.

Pore-suspending lipid bilayers formed by the painting technique were proven to be ideally suited as membrane biosensors with fully functional transmembrane ion channels. The peptide antibiotics gramicidin and alamethicin as well as the transmembrane domain of the HIV-1 accessory peptide Vpu were successfully inserted into these novel chip-based membrane systems and peptide-characteristic conductance states were recorded. For Vpu, different amiloride derivates were elucidated as potential drugs to inhibit its channel activity. These measurements confirm the potential of nano- and micro-BLMs as membrane biosensors.

Pore-suspending lipid bilayers based on hexagonally ordered pore arrays will allow for automation and parallelization of ion channel recordings and will thus enable the development of high-throughput screening assays. Furthermore, the highly ordered porous structure serving as membrane support will allow adressing each substrate pore by space-resolved electrochemical techniques. This will enable one to perform several measurements on one support quasi-simultaneously.

Summary in German:

Ionenkanäle stellen eines der Hauptziele für die Medikamentenentwicklung dar und stehen deshalb besonders im Fokus verschiedenster Membranbiosensor-Anwendungen und Medikamenten-Testsystemen. Das Ziel dieser Arbeit war die Entwicklung und Charakterisierung eines neuartigen porenüberspannenden Membransystems, das durch hochgeordnete, siebartige Strukturen gestützt und dadurch stabilisiert wird. Dieses Hybrid-Membransystem sollte die Vorteile der freitragenden und der festkörpergestützten Lipidmembranen in sich vereinigen. Hierbei gleichen die Bereiche der Lipiddoppelschicht, die an der porösen Substratoberfläche verankert sind, den festkörpergestützten Membranen, wohingegen die porenüberspannenden Bereiche als freitragende Membranen gesehen werden können.

Durch verschiedene Ätzverfahren wurden hexagonal geordnete poröse Aluminiumoxid- und Silizium-Träger mit Porendurchmessern im Nano- und Mikrometerbereich hergestellt und anschließend durch Impedanzspektroskopie und Rasterelektronenmikroskopie charakterisiert. Diese hochgeordneten porösen Strukturen, bestehend aus Milliarden von Poren pro Quadratzentimeter, wurden als Trägermedien für Lipiddoppelschichten eingesetzt.

Es wurden zwei unterschiedliche Methoden entwickelt, um porenüberspannende Lipiddoppelschichten zu erzeugen: (1) die sogenannte „Painting“-Technik und (2) eine Technik, die auf dem Spreiten von Vesikeln und deren Fusion zu Lipiddoppelschichten beruht.

(1) Die „Painting“-Technik: Die Oberfläche der Porenstege wurde durch die Bedeckung mit einer dünnen Goldschicht, gefolgt von der Chemisorption von Dipalmitoylphosphatidylthioethanol oder Oktadekanthiol, selektiv funktionalisiert. Somit konnte gewährleistet werden, dass die Lipidmembranen ausschließlich die Poren überspannen und nicht die Innenwände der Poren auskleiden. Eine Lipiddoppelschicht wurde erzeugt, indem das Phospholipid Dipalmitoylphosphatidylcholin, gelöst in Dekan, über die poröse Matrix „gestrichen“ wurde. Der Membranbildungsprozess wurde mit Hilfe der Impedanzspektroskopie verfolgt und charakterisiert. Aus den Impedanzdaten wurden membranspezifische Parameter bestimmt, indem das elektrische Verhalten des Membransystems durch ein geeignetes elektrisches Ersatzschaltbild, das sich

zusammensetzt aus einer einfachen Parallelschaltung aus dem Membranwiderstand und der Membrankapazität, beschrieben wurde. Spezifische Membrankapazitäten um 0,7 $\mu F/cm^2$ bestätigten die Ausbildung von Lipiddoppelschichten. Membranen, basierend auf porösem Aluminat, wurden von uns entsprechend des Porendurchmessers „nano-BLMs“ und diejenigen, basierend auf makroporösem Silizium, dementsprechend „micro-BLMs“ genannt. Sowohl „nano“- als auch „micro-BLMs“ besitzen eine außergewöhnlich hohe Langzeitstabilität und Membranwiderstände im Gigaohm-Bereich, die Einzelkanalmessungen erlauben. Im Gegensatz zu den klassischen freitragenden Lipidmembranen, die in einem Ereignis komplett zusammenbrechen, verringert sich der Membranwiderstand von „nano“- als auch „micro-BLMs“ kontinuierlich. Dies kann der Tatsache zugeschrieben werden, dass jeder freitragende Membranbereich aufgrund der räumlichen Trennung durch die am porösen Substrat fixierten Membranbereiche, einzeln reißen kann. Um diese Hypothese zu überprüfen, wurden „porous matrix-supported BLMs“ mit der „Painting“-Technik erzeugt, jedoch ohne vorausgehende Funktionalisierung der porösen Oberfläche. Die „porous matrix-supported BLMs“ zeigten ebenfalls die typischen membranspezifischen Parameter. Da sie in einem Ereignis komplett zusammenbrachen, gleichen die „porous matrix-supported BLMs“ wiederum den klassischen freitragenden Membranen,

(2) Das Spreiten von Vesikeln: Die Bildung von lösungsmittelfreien porenüberspannenden Lipiddoppelschichten wurde durch Spreiten von thiolipidhaltigen unilamellaren Vesikeln auf einer goldbedeckten porösen Aluminiumoxid-Oberfläche erreicht. Die Auswertung der Impedanzdaten zeigte, dass diese lösungsmittelfreien Membranen nicht defektfrei ausgebildet werden konnten und sie daher bisher nicht für Einzelkanalmessungen geeignet waren.

Porenüberspannende Lipiddoppelschichten, die mit Hilfe der „Painting“-Technik erzeugt wurden, haben sich bereits als funktionsfähige Membranbiosensoren bewährt. Die peptidischen Antibiotika Gramicidin und Alamethicin, sowohl als auch die synthetisch hergestellte Transmembrandomäne des viralen Peptids Vpu, integrierten erfolgreich in die neuartigen chip-basierenden Membransysteme, und es wurden für die einzelnen Peptide charakteristische Leitfähigkeitsstufen gemessen. Anhand des viralen Peptids Vpu wurden zusätzlich verschiedene Amilorid-Derivate als potentielle Medikamente getestet, die die Kanalaktivität des Peptids verhindern. Diese Messungen bestätigen das Potential der „nano“- und „micro-BLMs“ als Membranbiosensoren.

Die porenüberspannenden Lipidmembranen, basierend auf hexagonal geordneten porösen Strukturen, werden in der Zukunft die Automatisierung und Parallelisierung von Ionenkanalmessungen, und darauf aufbauend, die Entwicklung von „High-throughput screening“-Systemen ermöglichen. Durch die hochgeordnete Porenanordnung ist es außerdem möglich, jede membranbedeckte Pore einzeln und systematisch durch hochauflösende elektrochemische Methoden zu charakterisieren. Somit könnten zeitgleich mehrere Messungen an einem Membransystem durchgeführt werden.

7 REFERENCES

1. Gorter, E., and Grendel, F. (1927). Bimolecular layers of lipoids on the chromocytes of the blood. Proc. Acad. Sci. *29*, 314-317.
2. Gorter, E., and Grendel, F. (1927). Spreading of the different lipoids final chromocytes of different animals. Proc. Acad. Sci. *29*, 318-320.
3. Garrett, R.H., and Grisham, C.M. (1995). Biochemistry (Fort Worth: Saunders College Publishing).
4. Lehninger, A.L., Nelson, D.L., and Cox, M.M. (1993). Principles of biochemistry, Second Edition (New York: Worth Publishers).
5. Vance, D.E., and Vance, J.E. (2002). Biochemistry of lipids, lipoproteins and membranes. In New Comprehensive Biochemistry, Volume 36, G. Bernardi, ed. (Amsterdam: Elsevier).
6. Singer, S.J., and Nicolson, G.L. (1972). The fluid mosaic model of the structure of cell membranes. Science *175*, 720-731.
7. Simons, K., and Ikonen, E. (2000). How cells handle cholesterol. Science *290*, 1721-1726.
8. Simons, K., and Ikonen, E. (1997). Functional rafts in cell membranes. Nature *387*, 569-572.
9. Morrissey, J.H. (2001). Morrissey lab protocol for preparing phospholipid vesicles (SUV) by sonication: Urbana-Champaign.
10. Olson, F., Hunt, C.A., Szoka, F.C., Vail, W.J., and Papahadjopoulos, D. (1979). Preparation of liposomes of defined size distribution by extrusion through polycarbonate membranes. Biochim. Biophys. Acta *557*, 9-23.
11. Namdeo, A., and Jain, N.K. (1996). Niosomes as drug carriers. Indian Journal of Pharmaceutical Sciences *58*, 41-46.
12. Mälkiä, A., Liljeroth, P., and Kontturi, K. (2001). Drug transfer through biomimetic Langmuir-Blodgett monolayers at a liquid-liquid interface. Analytical Sciences *17*, 345-348.
13. Fuchs, H. (1993). Atomic force and scanning tunneling microscopies of organic surfaces. J. Mol. Struct. *22*, 29-47.

14. Terrettaz, S., Stora, T., Duschl, C., and Vogel, H. (1993). Protein binding to supported lipid membranes: Investigation of the cholera toxin-ganglioside interaction by simultaneous impedance spectroscopy and surface plasmon resonance. Langmuir *9*, 1361-1369.
15. Wegener, J., Janshoff, A., and Steinem, C. (2001). The quartz crystal microbalance as a novel means to study cell-substrate interactions in situ. Cell. Biochem. Biophys. *34*, 121-151.
16. Janshoff, A., Galla, H.J., and Steinem, C. (2000). Piezoelectric mass-sensing devices as biosensors - an alternative to optical biosensors? Angew. Chem. Int. Ed. Engl. *39*, 4004-4032.
17. Purrucker, O., Hillebrandt, H., Adlkofer, K., and Tanaka, M. (2001). Deposition of highly resistive lipid bilayer on silicon-silicon dioxide electrode and incorporation of gramicidin studied by ac impedance spectroscopy. Electrochim. Acta *47*, 791-798.
18. Wiegand, G., Arribas-Layton, N., Hillebrandt, H., Sackmann, E., and Wagner, P. (2002). Electrical properties of supported lipid bilayer membranes. J. Phys. Chem. B *106*, 4245-4254.
19. Wiegand, G. (2000). Fundamental principles of the electric properties of supported lipid membranes investigated by advanced methods of impedance spectroscopy, TU München, München.
20. Groves, J.T., and Dustin, M.L. (2003). Supported planar bilayers in studies on immune cell adhesion and communication. J. Immunological Methods *278*, 19-32.
21. Cornell, B.A., Braach-Maksvytis, V., King, L.G., Osman, P.D.J., Raguse, B., Wieczorek, L., and Pace, R.J. (1997). A biosensor that uses ion-channel switches. Nature *387*, 580-583.
22. Blodgett, K.B. (1935). Films built by depositing successive monomolecular layers on a solid surface. J. Am. Chem. Soc. *57*, 1007-1022.
23. Langmuir, I., and Schäfer, V.J. (1938). Activities of urease and pepsin monolayers. J. Am. Chem. Soc. *60*, 1351-1360.
24. Cremer, P.S., and Boxer, S.G. (1999). Formation and spreading of lipid bilayers on planar glass supports. J. Phys. Chem. B *103*, 2554-2559.
25. Rapuano, R., and Carmona-Ribeiro, A.M. (1997). Physical adsorption of bilayer membranes on silica. J. Colloid. Interface. Sci. *193*, 104-111.

26. Jass, J., Tjarnhage, T., and Puu, G. (2000). From liposomes to supported, planar bilayer structures on hydrophilic and hydrophobic surfaces: an atomic force microscopy study. Biophys. J. *79*, 3153-3163.

27. Brian, A.A., and McConnell, H.M. (1984). Allogeneic stimulation of cytotoxic T cells by supported planar membranes. Proc. Natl. Acad. Sci. USA *81*, 6159-6163.

28. Tamm, L.K., and McConnell, H.M. (1985). Supported phospholipid bilayers. Biophys. J. *47*, 105-113.

29. Duschl, C., Liley, M., Corradin, G., and Vogel, H. (1994). Biologically addressable monolayer structures formed by templates of sulfur-bearing molecules. Biophys. J. *67*, 1229-1237.

30. Duschl, C., Liley, M., Lang, H., Ghandi, A., Zakeeruddin, S.M., Stahlberg, H., Dubochet, J., Nemetz, A., Knoll, W., and Vogel, H. (1996). Sulphur bearing lipids for the covalent attachment of supported lipid bilayers to gold surfaces: a detailed characterisation and analysis. Materials Science and Engineering *C4*, 7-18.

31. Bain, C.D., Troughton, E.B., Tao, Y., Evall, J., Whitesides, G.M., and Nuzzo, R.G. (1989). Formation of monolayer films by the spontaneous assembly of organic thiols from solution onto gold. J. Am. Chem. Soc. *111*, 321-335.

32. Steinem, C., Janshoff, A., von dem Bruch, K., Reihs, K., Goossens, J., and Galla, H.-J. (1998). Valinomycin-mediated transport of alkali cations through solid supported membranes. Bioelectrochem. Bioenerg. *45*, 17-26.

33. Lingler, S., Rubinstein, I., Knoll, W., and Offenhäuser, A. (1997). Fusion of small unilamellar lipid vesicles to alkanethiol and thiolipid self-assembled monolayers on gold. Langmuir *13*, 7085-7091.

34. Rädler, J., and Sackmann, E. (1997). Functionalization of solids by ultrathin soft polymer films and polymer/lipid film composites: Modeling of cell surfaces and cell recognition processes. Curr. Opin. Solid. St. M. *2*, 330-336.

35. Majewski, J., Wong, J.Y., Park, C.K., Seitz, M., Israelachvili, J.N., and Smith, G.S. (1998). Structural studies of polymer-cushioned lipid bilayers. Biophys. J. *75*, 2363-2367.

36. Terrettaz, S., Mayer, M., and Vogel, H. (2003). Highly electrically insulating tethered lipid bilayers for probing the function of ion channel proteins. Langmuir *19*, 5567-5569.

37. Müller, P., Rudin, D.O., Tien, H.T., and Wescott, W.C. (1963). Methods for the formation of single bimolecular lipid membranes in aqueous solutions. J. Phys. Chem. *67*, 534-535.

38. Tien, H.T., and Ottova, A.L. (2000). Membrane biophysics: planar lipid bilayers and spherical liposomes (Amsterdam and New York: Elsevier).

39. White, S.H. (1978). Formation of "solvent-free" black lipid bilayer membranes from glyceryl monooleate dispersed in squalene. Biophys. J. *23*, 337-347.

40. Montal, M., and Müller, P. (1972). Formation of bimolecular membranes from lipid monolayers and a study of their electrical properties. Proc. Natl. Acad. Sci. USA *69*, 3561-3566.

41. Trojanowicz, M. (2001). Miniaturized biochemical sensing devices based on planar bilayer lipid membranes. Fresenius J. Anal. Chem. *371*, 246-260.

42. Schuster, B., Sleytr, U.B., Diederich, A., Bahr, G., and Winterhalter, M. (1999). Probing the stability of S-layer-supported planar lipid membranes. Eur. Biophys. J. *28*, 583-590.

43. Osborn, T.D., and Yager, P. (1995). Formation of planar solvent-free phospholipid bilayers by Langmuir-Blodgett transfer of monolayers to micromachined apertures in silicon. Langmuir *11*, 8-12.

44. Fertig, N., George, M., Klau, M., Meyer, C., Tilke, A., Sobotta, C., Blick, R.H., and Behrends, J.C. (2003). Microstructured apertures in planar glass substrates for ion channel research. Receptors Channels *9*, 29-40.

45. Fertig, N., Meyer, C., Blick, R.H., Trautmann, C., and Behrends, J.C. (2001). Microstructured glass chip for ion-channel electrophysiology. Phys. Rev. E *64*, 1-4.

46. Fertig, N., Tilke, A., Blick, R.H., and Kotthaus, J.P. (2000). Stable integration of isolated cell membrane patches in a nanomachined aperture. Appl. Phys. Lett. *77*, 1218-1220.

47. Mayer, M., Kriebel, J.K., Tosteson, M.T., and Whitesides, G.M. (2003). Microstructured teflon membranes for low-noise recordings of ion channels in planar lipid bilayers. Biophys. J. *85*, 2684-2695.

48. Cheng, Y., Bushby, R.J., Evans, S.D., Knowles, P.F., Miles, R.E., and Ogier, S.D. (2001). Single ion channel sensitivity in suspended bilayers on micromachined supports. Langmuir *17*, 1240-1242.

49. Ogier, S.D., Bushby, R.J., Cheng, Y., Evans, S.D., Evans, S.W., Jenkins, T.A., Knowles, P.F., and Miles, R.E. (2000). Suspended planar phospholipid bilayers on micromachined supports. Langmuir *16*, 5696-5701.

50. Peterman, M.C., Ziebarth, J.M., Braha, O., Bayley, H., Fishman, H.A., and Bloom, D.M. (2002). Ion channels and lipid bilayer membranes under high potential using microfabricated apertures. Biomed. Microdevices *4*, 231-236.

51. Schmidt, C., Mayer, M., and Vogel, H. (2000). A chip-based biosensor for the functional analysis of single ion channels. Angew. Chem. Int. Ed. *39*, 3137-3140.

52. Pantoja, R., Sigg, D., Blunck, R., Bezanilla, F., and Heath, J.R. (2001). Bilayer reconstitution of voltage-dependent ion channels using a microfabricated silicon chip. Biophys. J. *81*, 2389-2394.

53. Favero, G., D'Annibale, A., Campanella, L., Santucci, R., and Ferri, T. (2002). Membrane supported bilayer lipid membranes array: Preparation, stability and ion-channel insertion. Anal. Chim. Acta *460*, 23-34.

54. Favero, G., Campanella, L., D'Annibale, A., Santucci, R., and Ferri, T. (2003). Mixed hybrid bilayer lipid membrane incorporating valinomycin: Improvements in preparation and functioning. Microchem. J. *74*, 141-148.

55. Nikolelis, D.P., and Siontorou, C.G. (1995). Bilayer lipid membranes for flow injection monitoring of acetylcholine, urea, and penicillin. Anal. Chem. *67*, 936-944.

56. Andreou, V.G., and Nikolis, D.P. (1998). Flow injection monitoring of aflatoxin M1 in milk and milk preparations using filter-supported bilayer lipid membranes. Anal. Chem. *70*, 2366-2371.

57. Mountz, J.M., and Tien, H.T. (1978). Photoeffects of pigmented lipid membranes in a microporous filter. Photochem. Photobiol. *28*, 395-400.

58. Bayley, H. (1999). Designed membrane channels and pores. Curr. Opin. Biotechnol. *10*, 94-103.

59. Marsh, D. (1996). Peptide models for membrane channels. Biochem. J. *315 (Pt 2)*, 345-361.

60. Futaki, S. (1998). Peptide ion channels: design and creation of function. Biopolymers *47*, 75-81.

61. Hanke, W., and Schlue, W.R. (1993). Planar lipid bilayers: Methods and applications (London: Academic Press).

62. Aidley, D.J., and Stanfield, P.R. (1996). Ion channels - Molecules in action (Cambridge, Melbourne: Cambridge University Press).

63. Ogden, D. (1987). Microelectrode Techniques - The Plymouth Workshop Handbook, Second Edition (Cambridge: The Company of Biologists Limited).

64. Hamill, O.P., Marty, A., Neher, E., Sakmann, B., and Sigworth, F.J. (1981). Improved patch-clamp techniques for high-resolution current recording from cells and cell-free membrane patches. Pflugers Arch. *391*, 85-100.

65. Sakmann, B., and Neher, E. (1995). Single-channel recording, Second Edition (New York: Plenum Press).

66. Hille, B. (1992). Ionic channels of excitable membranes, Second Edition (Sunderland, Massachusetts: Sinauer).

67. Miller, C. (1986). Ion channel reconstitution (New York: Plenum Press).

68. Numberger, M., and Draguhn, A. (1996). Patch-Clamp-Technik (Heidelberg: Spektrum Akademischer Verlag GmbH).

69. Sansom, M.S.P., Tieleman, D.P., and Berendsen, H.J.C. (1999). The mechanism of channel formation by alamethicin as viewed by molecular dynamics simulations. In Gramicidin related ion channel-forming peptides. (Chichester: John Wiley & Sons), pp. 128-145.

70. Myers, V.B., and Haydon, D.A. (1972). Ion transfer across lipid membranes in the presence of gramicidin A. II. The ion selectivity. Biochim. Biophys. Acta *274*, 313-322.

71. Müller, P., and Rudin, D.O. (1968). Action potentials induced in biomolecular lipid membranes. Nature *217*, 713-719.

72. Cross, T.A., Tian, F., Cotten, M., Wang, J., Kovacs, F., and Fu, R. (1999). Correlations of structure, dynamics and function in the gramicidin channel by solid-state NMR spectroscopy. In Gramicidin and related ion channel-forming peptides. (Chichester: John Wiley & Sons).

73. Wallace, B.A. (1990). Gramicidin channels and pores. Annu. Rev. Biophys. Biophys. Chem. *19*.

74. Marshall, G.R., and Beusen, D.D. (1994). The structural basis of peptide channel formation (Washington: American Chemical Society).

75. Hladky, S.B., and Haydon, D.A. (1972). Ion transfer across lipid membranes in the presence of gramicidin A. I. Studies of the unit conductance channel. Biochim. Biophys. Acta *274*, 294-312.

76. Andersen, O.S. (1983). Ion movement through gramicidin A channels. Biophys. J. *41*, 119-133.

77. Hall, J.E., Vodyanoy, I., Balasubramanian, T.M., and Marshall, G.R. (1984). Alamethicin. A rich model for channel behavior. Biophys. J. *45*, 233-247.

78. Bezrukov, S.M., and Vodyanoy, I. (1997). Signal transduction across alamethicin ion channels in the presence of noise. Biophys. J. *73*, 2456-2464.

79. Bechinger, B. (1997). Structure and functions of channel-forming peptides: Magainins, cecropins, melittin and alamethicin. J. Membrane Biol. *156*, 197-211.

80. Sansom, M.S.P. (1991). The biophysics of peptide models of ion channels. Prog. Biophys. Molec. Biol. *55*, 139-235.

81. Gordon, L.G.M., and Haydon, D.A. (1976). Kinetics and stability of alamethicin conducting channels in lipid bilayers. Biochim. Biophys. Acta *436*, 541-556.

82. Tieleman, D.P., Berendsen, J.C., and Sansom, M.S.P. (1999). An alamethicin channel in a lipid bilayer: Molecular dynamics simulations. Biophys. J. *76*, 1757-1769.

83. You, S., Peng, S., Lien, L., Breed, J., Sansom, M.S.P., and Woolley, G.A. (1996). Engineering stabilized ion channels: Covalent dimers of alamethicin. Biochemistry *35*, 6225-6232.

84. Aguilella, V., and Bezrukov, S.M. (2001). Alamethicin channel conductance modified by lipid charge. Eur. Biophys. J. *30*, 233-241.

85. Montal, M. (2003). Structure-function correlates of Vpu, a membrane protein of HIV-1. FEBS Lett. *552*, 47-53.

86. Fischer, W.B. (2003). Vpu from HIV-1 on an atomic scale: Experiments and computer simulations. FEBS Lett. *552*, 39-46.

87. Marassi, F.M., Ma, C., Gratkowski, H., Straus, S.K., Strebel, K., Oblatt-Montal, M., Montal, M., and Opella, S.J. (1999). Correlation of the structural and functional domains in the membrane protein Vpu from HIV-1. Proc. Natl. Acad. Sci. USA *96*, 14336-14341.

88. Ewart, G.D., Mills, K., Cox, G.B., and Gage, P.W. (2002). Amiloride derivatives block ion channel activity and enhancement of virus-like particle budding caused by HIV-1 protein Vpu. Eur. Biophys. J. *31*, 26-35.

89. Ewart, G.D., Sutherland, T., Gage, P.W., and Cox, G.B. (1996). The Vpu protein of human immunodeficiency virus type 1 forms cation-selective ion channels. J. Virol. *70*, 7108-7115.

90. Schubert, U., Ferrer-Montiel, A.V., Oblatt-Montal, M., Henklein, P., Strebel, K., and Montal, M. (1996). Identification of an ion channel activity of the Vpu transmembrane domain and its involvement in the regulation of virus release from HIV-1-infected cells. FEBS Lett. *398*, 12-18.

91. Park, S.H., Mrse, A.A., Nevzorov, A.A., Mesleh, M.F., Oblatt-Montal, M., Montal, M., and Opella, S.J. (2003). Three-dimensional structure of the channel-forming trans-membrane domain of virus protein "u" (Vpu) from HIV-1. J. Mol. Biol. *333*, 409-424.

92. Lamb, R.A., and Pinto, L.H. (1997). Do Vpu and Vpr of human immunodeficiency virus type 1 and NB of influenza B virus have ion channel activities in the viral life cycles? Virology *229*, 1-11.

93. Lawes, G. (1987). Scanning electron microscopy and X-ray microanalysis (Chichester: Wiley).

94. Reimer, L. (1985). Scanning electron microscopy: Physics of image formation and microanalysis (Berlin: Springer).

95. Steinem, C., Janshoff, A., Galla, H.-J., and Sieber, M. (1997). Impedance analysis of ion transport through gramicidin channels incorporated in solid supported lipid bilayers. Bioelectrochem. Bioenerg. *42*, 213-220.

96. Vallejo, A.E., and Gervasi, C.A. (2002). Impedance analysis of ion transport through gramicidin channels in supported lipid bilayers. Bioelectrochem. *57*, 1-7.

97. Bard, A.J., and Faulkner, L.R. (2001). Electrochemical methods - Fundamentals and applications, Second Edition (New York: John Wiley & Sons, Inc.).

98. Bard, A.J., and Stratmann, M. (2003). Instrumentation and electroanalytical chemistry (Weinheim: WILEY-VCH).

99. Schmickler, W. (1996). Interfacial electrochemistry (New York: Oxford University Press).

100. Macdonald, J.R. (1987). Impedance spectroscopy - emphasizing solid materials and systems (New York: Whiley & Sons).

101. Jones, S.W. (1990). Whole-cell and microelectrode voltage clamp. In Neuromethods, Vol. 14: Neurophysiological Techniques, Volume 14, A.A. Boulton and G.B. Baker, eds. (Clifton, New Jersey: The Humana Press).

102. Sherman-Gold, R. (1993). The Axon Guide.

103. Keller, F., Hunter, M.S., and Robinson, D.L. (1953). Structural features of oxide coatings on aluminum. J. Electrochem. Soc. *100*, 411-419.

104. Lehmann, V. (1993). The physics of macropore formation in low-doped n-type silicon. J. Electrochem. Soc. *140*, 2836-2843.

105. Bailey, G., and Wood, G.C. (1974). Morphology of anodic films formed on aluminum in oxalic acid. Transactions of the institute of metal finishing *52*, 187-199.

106. O´Sullivan, J.P., and Wood, G.C. (1970). Porous anodic films on aluminum. Proceedings of the Royal Society of London. Series A, Mathematical and Physical Sciences *317*, 511-543.

107. Siejka, J., and Ortega, C. (1977). An O^{18} study of field-assisted pore formation in compact anodic films on aluminum. J. Electrochem. Soc. *124*, 883-891.

108. Jessensky, O., Müller, F., and Gösele, U. (1998). Self-organized formation of hexagonal pore arrays in anodic alumina. Appl. Phys. Lett. *72*, 1173-1175.

109. Diggle, J.W., Downie, T.C., and Goulding, C.W. (1968). Anodic oxide films on aluminium. pp. 365-405: Newcastle upon Tyne.

110. Parkhutik, V.P., and Shershulsky, V.I. (1992). Theoretical modeling of porous oxide growth on aluminium. J. Phys. D: Appl. Phys. *25*, 1258-1263.

111. Wehrspohn, R.B., Nielsch, K., Birner, A., Schilling, J., Müller, F., Li, A.-P., and Gösele, U. (2001). Electrochemically prepared high-aspect-ratio highly ordered pore arrays and applications. In Second International Symposium on Pits and Pores Meeting of The Electrochemical Society. pp. 2000-2025: San Francisco, USA.

112. Nielsch, K., Choi, J., Schwirn, K., Wehrspohn, R.B., and Gösele, U. (2002). Self-ordering regimes of porous alumina: the 10% porosity rule. Nano Lett.

113. Li, A.P., Müller, F., Birner, A., Nielsch, K., and Gösele, U. (1998). Hexagonal pore arrays with a 50-420 nm interpore distance formed by self-organization in anodic alumina. J. Appl. Physics *84*, 6023-6026.

114. Jessensky, O. (1997). Untersuchungen zum Porenwachstum in 6H-Siliziumkarbid und anodischem Aluminiumoxid, Martin-Luther-Universität Halle-Wittenberg, Halle (Saale).

115. Jessensky, O., Müller, F., and Gösele, U. (1998). Self-organized formation of hexagonal pore structures in anodic alumina. J. Electrochem. Soc. *145*, 3735-3740.

116. Masuda, H., and Fukuda, K. (1995). Ordered metal nanohole arrays made by a two-step replication of honeycomb structures of anodic alumina. Science *268*, 1466-1468.

117. Li, A.P., Müller, F., Birner, A., Nielsch, K., and Gösele, U. (1999). Fabrication and microstructuring of hexagonally ordered two-dimensional nanopore arrays in anodic alumina. Adv. Mater. *11*, 483-487.

118. Li, A.P., Müller, F., Birner, A., Nielsch, K., and Gösele, U. (1999). Polycrystalline nanopore arrays with hexagonal ordering on aluminium. J. Vac. Sci. Technol. A *17*, 1428-1431.

119. Masuda, H., Hasegwa, F., and Ono, S. (1997). Self-ordering of cell arrangement of anodic porous alumina formed in sulfuric acid solution. J. Electrochem. Soc. *144*, L127-130.

120. Lehmann, V., and Föll, H. (1990). Formation mechanism and properties of electrochemically etched trenches in n-type silicon. J. Electrochem. Soc. *137*, 653-658.

121. Licht, S. (2002). Semiconductor electrodes and photoelectrochemistry. In Encyclopedia of electrochemistry, Volume 6, M. Stratmann, ed. (Weinheim: Wiley-VCH).

122. Ronkel, F., and Schultze, J.W. (2000). Electrochemical aspects of porous silicon formation. J. Porous Mater. *7*, 11-16.

123. Smith, R.L., and Collins, S.D. (1992). Porous silicon formation mechanisms. J. Appl. Phys. *71*, R1-R22.

124. Lehmann, V. (2002). Electrochemistry of silicon (Weinheim: Wiley-VCH Verlag GmbH).

125. Seidel, H., Csepregi, L., Heuberger, A., and Baumgaertel, H. (1990). Anisotropic etching of crystalline silicon in alkaline solutions. I. Orientation dependence and behavior of passivation layers. J. Electrochem. Soc. *137*, 3612-3626.

126. Müller, F., Birner, A., Gösele, U., Lehmann, V., Ottow, S., and Föll, H. (2000). Structuring of macroporous silicon for applications as photonic crystals. J. Porous Mater. *7*, 201-204.

127. Florin, E.L., and Gaub, H.E. (1993). Painted supported lipid membranes. Biophys. J. *64*, 375-383.

128. McConnell, H.M., Watts, T.H., Weis, R.M., and Brian, A.A. (1986). Supported planar membranes in studies of cell-cell recognition in the immune system. Biochim. Biophys. Acta *864*, 95-106.

129. Kalb, E., Frey, S., and Tamm, L.K. (1992). Formation of supported planar bilayers by fusion of vesicles to supported phospholipid monolayers. Biochim. Biophys. Acta *1103*, 307-316.

130. Keller, C.A., and Kasemo, B. (1998). Surface specific kinetics of lipid vesicle adsorption measured with a quartz crystal microbalance. Biophys. J. *75*, 1397-1402.

131. Pignataro, B., Steinem, C., Galla, H.J., Fuchs, H., and Janshoff, A. (2000). Specific adhesion of vesicles monitored by scanning force microscopy and quartz crystal microbalance. Biophys. J. *78*, 487-498.

132. Reviakine, I., and Brisson, A. (2000). Formation of supported phospholipid bilayers from unilamellar vesicles investigated by atomic force microscopy. Langmuir *16*, 1806-1815.

133. MacDonald, R.C., MacDonald, R.I., Menco, B.P., Takeshita, K., Subbarao, N.K., and Hu, L.R. (1991). Small-volume extrusion apparatus for preparation of large, unilamellar vesicles. Biochim. Biophys. Acta *1061*, 297-303.

134. Drexler, J. (2003). Herstellung porenüberspannender Lipidmembranen auf Basis poröser Aluminate und deren Charakterisierung mittels elektrischer Impedanzspektroskopie, Universität Regensburg, Regensburg.

135. Drexler, J., and Steinem, C. (2003). Suspended lipid bilayers on porous alumina investigated by electrical impedance spectroscopy. J. Phys. Chem. B *107*, 11245-11254.

136. De Laet, J., Terryn, H., and Vereecken, J. (1996). The use of impedance spectroscopy and optical reflection spectroscopy to study modified aluminium surfaces. Electrochim. Acta *41*, 1155-1161.

137. Plant, A. (1993). Self-assembled phospholipid/alkanethiol biomimetic bilayers on gold. Langmuir *9*, 2764-2767.

138. Römer, W., and Steinem, C. (2004). Impedance analysis and single-channel recordings on nano-black lipid membranes based on porous alumina. Biophys. J. *86*, 955-965.

139. Benz, R., Fröhlich, O., Läuger, P., and Montal, M. (1975). Electrical capacity of black lipid films and of lipid bilayers made from monolayers. Biochim. Biophys. Acta *394*, 323-334.

140. Steinem, C. (1997). Ionentransport in festkörpergestützten Lipiddoppelschichten - Eine Untersuchung der Aktivität von Melittin, Gramicidin, Valinomycin und Bakteriorhodopsin, Universität Münster, Münster.

141. Hennesthal, C., Drexler, J., and Steinem, C. (2002). Membrane-suspended nanocompartments based on ordered pores in alumina. ChemPhysChem *3*, 885-889.

142. Hennesthal, C., and Steinem, C. (2000). Pore-spanning lipid bilayers visualized by scanning force microscopy. J. Am. Chem. Soc. *122*, 8085-8086.

143. Lemaitre, V., Ali, R., Kim, C.G., Watts, A., and Fischer, W.B. (2004). Interaction of amiloride and one of its derivatives with Vpu from HIV-1: A molecular dynamics simulation. FEBS Lett. *563*, 75-81.

144. Nielsch, K. (2002). Hochgeordnete ferromagnetische Nano-Stabensembles, Martin-Luther-Universität Halle-Wittenberg, Halle (Saale).

145. Birner, A., Grüning, U., Ottow, S., Schneider, A., Müller, F., Lehmann, V., Föll, H., and Gösele, U. (1998). Macroporous silicon: A two-dimensional photonic bandgap material suitable for the near-infrared spectral range. Phys. Stat. Sol. (a) *165*, 111-117.

146. Lehmann, V., and Gösele, U. (1991). Porous silicon formation: A quantum wire effect. Appl. Phys. Lett. *58*, 856-858.

147. Proux-Delrouyre, V., Laval, J.M., and Bourdillon, C. (2001). Formation of streptavidin-supported lipid bilayers on porous anodic alumina: Electrochemical monitoring of triggered vesicle fusion. J. Am. Chem. Soc. *123*, 9176-9177.

148. Korchev, Y.E., Bashford, C.L., Milovanovic, M., Vodyanoy, I., and Lab, M.J. (1997). Scanning ion conductance microscopy of living cells. Biophys. J. *73*, 653-658.

149. Korchev, Y.E., Gorelik, J., Lab, M.J., Sviderskaya, E.V., Johnston, C.L., Coombes, C.R., Vodyanoy, I., and Edwards, C.R. (2000). Cell volume measurement using scanning ion conductance microscopy. Biophys. J. *78*, 451-457.

150. Korchev, Y.E., Milovanovic, M., Bashford, C.L., Bennett, D.C., Sviderskaya, E.V., Vodyanoy, I., and Lab, M.J. (1997). Specialized scanning ion-conductance microscope for imaging of living cells. J. Microsc. *188 (Pt 1)*, 17-23.

151. Marchal, D., Bourdillon, C., and Demé, B. (2001). Small-angle neutron scattering by highly oriented hybrid bilayer membranes confined in anisotropic porous alumina. Langmuir *17*, 8313-8320.

152. Gassa, L.M., Vallejo, A.E., Alonso-Romanowski, S., and Vilche, J.R. (1997). Identification of channel membrane processes in bilayer lipid membranes by electrochemical techniques. Bioelectrochem. Bioenerg. *42*, 187-192.

153. Alonso-Romanowski, S., Gassa, L.M., and Vilche, J.R. (1995). An investigation by EIS of gramicidin channels in bilayer lipid membranes. Electrochim. Acta *40*, 1561-1567.

154. Bamberg, E., Noda, K., Gross, E., and Läuger, P. (1976). Single-channel parameters of gramicidin A,B and C. Biochim. Biophys. Acta *419*, 223-228.

155. Bamberg, E., and Benz, R. (1976). Voltage-induced thickness changes of lipid bilayer membranes and the effect of an electric field on gramicidin A channel formation. Biochim. Biophys. Acta *426*, 570-580.

156. Cordes, F.S., Tustian, A.D., Sansom, M.S., Watts, A., and Fischer, W.B. (2002). Bundles consisting of extended transmembrane segments of Vpu from HIV-1: Computer simulations and conductance measurements. Biochemistry *41*, 7359-7365.

157. Kochendoerfer, G.G., Jones, D.H., Lee, S., Oblatt-Montal, M., Opella, S.J., and Montal, M. (2004). Functional characterization and NMR spectroscopy on full-length Vpu from HIV-1 prepared by total chemical synthesis. J. Am. Chem. Soc. *126*, 2439-2446.

158. Ma, C., Marassi, F.M., Jones, D.H., Straus, S.K., Bour, S., Strebel, K., Schubert, U., Oblatt-Montal, M., Montal, M., and Opella, S.J. (2002). Expression, purification, and activities of full-length and truncated versions of the integral membrane protein Vpu from HIV-1. Protein Science *11*, 546-557.

159. Becker, C.F., Oblatt-Montal, M., Kochendoerfer, G.G., and Montal, M. (2004). Chemical synthesis and single channel properties of tetrameric and pentameric TASPs (template-assembled synthetic proteins) derived from the transmembrane domain of HIV virus protein u (Vpu). J. Biol. Chem. *279*, 17483-17489.

160. Grice, A.L., Kerr, I.D., and Sansom, M.S. (1997). Ion channels formed by HIV-1 Vpu: A modelling and simulation study. FEBS Lett. *405*, 299-304.

161. Lopez, C.F., Montal, M., Blasie, J.K., Klein, M.L., and Moore, P.B. (2002). Molecular dynamics investigation of membrane-bound bundles of the channel-forming transmembrane domain of viral protein U from the human immunodeficiency virus HIV-1. Biophys. J. *83*, 1259-1267.

162. Vodyanoy, I., Hall, J.E., and Balasubramanian, T.M. (1983). Alamethicin-induced current-voltage curve asymmetry in lipid bilayers. Biophys. J. *42*, 71-82.

ANNEX

A1 Abbreviations (alphabetically)

AC	Alternating current
BLM	Black lipid membrane
CF	5,6-Carboxyfluorescein
CPE	Constant phase element
d	Day
DC	Direct current
DMA	5-(*N*,*N*-Dimethyl) amiloride hydrochloride
DODAB	*N*,*N*-Dioctadecyl-*N*,*N*-dimethyl ammonium bromide
DOPC	1,2-Dioleoyl-*sn*-glycero-3-phosphocholine
DPhPC	1,2-Diphytanoyl-*sn*-glycero-3-phosphocholine
DPPTE	1,2-Dipalmitoyl-*sn*-glycero-3-phosphothioethanol
EIS	Electrical impedance spectroscopy
el	Electrolyte
em	Emission
Eq	Equation
ex	Excitation
F	Farad
Fig	Figure
FRET	Fluorescence resonance energy transfer
g	Gram
h	Hour
HEPES	*N*-2-Hydroxyethylpiperazine-*N*'-2-ethanesulfonic acid
HF	Hydrofluoric acid
HMA	5-(*N*,*N*-Hexamethylene) amiloride
HTS	High-throughput screening
IR	Infrared
LB	Langmuir-Blodgett

LS	Langmuir-Schäfer
LUV	Large unilamellar vesicles
m	Membrane; Meter
M	molar
min	Minute
MLV	Multilamellar vesicles
mol	Moles
MPA	3-Mercapto propionic acid
MUDA	11-Mercapto undecanoic acid
N	Newton
o	overall
ODT	1-Octadecanethiol
Pa	Pascal
PS	Porous structure
PSM	Painted supported membrane
R	Reaction
RT	Room temperature
s	Second
S	Siemens
SAM	Self-assembled monolayer
SEM	Scanning electron microscopy
SFM	Scanning force microscopy
SSM	Solid supported membrane
SUV	Small unilamellar vesicles
TM	transmembrane
Tris	Tris (hydroxymethyl) aminoethan
V	Volts
wt	Weight
°C	Degrees centigrade

c	Centi	10^{-2}
m	Milli	10^{-3}
µ	Micro	10^{-6}
n	Nano	10^{-9}
p	Pico	10^{-12}
k	Kilo	10^{3}
M	Mega	10^{6}
G	Giga	10^{9}

A2 Symbols (alphabetically)

A	Area; Constant phase element
c	Concentration
C	Capacitance, Capacitor
d	Thickness
E	Energy
f	Frequency
I	Current
h	Planck´s constant
h^+	Hole
G	Conductance
i	Complex unit
L	Inductivity, Inductor
m	Mass
M	Molecular weight
n	Number of experiments
R	Resistance, Resistor
t	Time
V	Voltage
Z	Impedance

$\|Z\|$	Absolute magnitude of the impedance
Z'	Real part of the impedance
Z''	Imaginary part of the impedance
ε_0	Natural constant; Permittivity of vacuum
ε_r	Dielectric constant
γ	Surface tension
φ	Phase shift
λ	Wavelength
π	Surface pressure
Θ	Surface coverage
σ	Warburg impedance
τ	Time constant
ν	Frequency
ω	Radial frequency

A3 Chemicals (alphabetically)

Aceton	Merck (Darmstadt)
Alamethicin	Sigma-Aldrich (Taufkirchen)
Amiloride hydrochloride-hydrate	Sigma-Aldrich (Taufkirchen)
Argon	Linde (München)
Caesium chloride	Merck (Darmstadt)
5,6-Carboxyfluorescein	Fluka (Deisenhofen
Chloroform	Merck (Darmstadt)
Cholesterol	Sigma-Aldrich (Taufkirchen)
Chromium(VI) oxide	Merck (Darmstadt)
Copper(II) chloride-2-hydrate	Riedel-de Haen (Seelze)
n-Decane	Sigma-Aldrich (Taufkirchen)
DMA	Sigma-Aldrich (Taufkirchen)

DODAB	Sigma (Steinheim)
DOPC	Avanti Polar Lipids (Alabaster, AL, USA)
DPhPC	Avanti Polar Lipids (Alabaster, AL, USA)
DPPTE	Avanti Polar Lipids (Alabaster, AL, USA)
Ethanol	Fluka (Neu-Ulm)
Gramicidin D	Sigma-Aldrich (Taufkirchen)
HEPES	Serva (Heidelberg)
HMA	Sigma-Aldrich (Taufkirchen)
Hydrofluoric acid 40%	Merck (Darmstadt)
Isopropanol	Merck (Darmstadt)
Lithium chloride	Merck (Darmstadt)
3-Mercapto propionic acid	Sigma-Aldrich (Taufkirchen)
11-Mercapto undecanoic acid	Probior (München)
Mercury(II) chloride	Merck (Darmstadt)
Methanol	Merck (Darmstadt)
Mucasol®	Merck (Darmstadt)
Nitrogen	Linde (München)
ODT	Merck-Schuchardt (Hohenbrunn)
Oxalic acid dihydrate	Merck (Darmstadt)
ortho-Phosphoric acid 85 %	Merck (Darmstadt)
Potassium chloride	Merck (Darmstadt)
Sodium chloride	Merck (Darmstadt)
Sodium sulfate	Merck (Darmstadt)
Sulfuric acid 95-97 %	Merck (Darmstadt)
Tris	Sigma-Aldrich (Taufkirchen)
Vpu	Wolfgang Fischer, Oxford University

A4 Materials (alphabetically)

Aluminum	Goodfellow (Huntingdon, UK)
Gold	Elektronen Optik Service (Dortmund)
Kalrez® perfluoroelastomer O-rings	Du Pont Dow Elastomers (Newark, USA)
Parafilm	American National Can (Chicago, USA)
Platin wire	Goodfellow (Huntingdon, UK)
Polycarbonate membranes	Avestin (Ottawa, USA)
Silicon wafer	Wacker (Burghausen)
Silver wire	Goodfellow (Huntingdon, UK)
Titanium	Elektronen Optik Service (Dortmund)

A5 Instrumentation

Etching equipment

Keithley 2400 Source Meter	Keithley Instruments (Cleveland, USA)
Tektronix PS 280 DC Power Supply	Tektronix Inc. (Beaverton, USA)
Tektronix Power Supply EA-PS 9300-02	Tektronix Inc. (Beaverton, USA)
Ecoline RE 104	Lauda GmbH (Königshofen)

Fluorescence intensity recordings

Aminco-Bowman Series 2 Luminescence Spectrometer	SLM-Aminco (Rochester/NY, USA)

Impedance spectroscopy

Impedance/Gain-Phase Analyzer SI 1260 1296 Dielectric Interface	Solartron Instruments (Farnborough, UK)

Scanning electron microscopy

Jeol JSM-6300*F* Scanning Microscope	Jeol in Germany (München)
Zeiss DSM 950	Zeiss (Oberkochen)

Single channel recordings

Axopatch 200*B* Patch-Clamp Amplifier Digidata 1322*A* A/D-Converter	Axon Instruments (Forster City, USA)

Water purification system

Milli-Q RO 10 Plus Milli-Q plus 185	Millipore GmbH (Eschborn)

Other instrumentation

Microbalance Ohaus	Ohaus (Prine Brook, New York, USA)
Miniextruder Liposofast®	Avestin (Ottawa, USA)
pH-Meter Knick 761 *Calimatic*	Knick (Berlin)
pH-Electrode InLab® 423	Mettler Toledo Prozessanalytik (Steinbach)
Plasma Cleaner PDC 32G-2	Harrick (New York, USA)
Sputter Coater 108 auto Thickness Controller mtm 20	Cressington (Watford, USA)
Ultrasonic Bath Bandelin Sonorex Super RK 255 H	Bandelin Electronic (Berlin)

A6 Publications, oral and poster presentations

Publications:

Winfried Römer, Claudia Steinem (2004)
"Impedance analysis and single channel recordings on nano-BLMs based on porous alumina"
Biophys. J. *86 (2)*, 955-965

Winfried Römer, Yuen H. Lam, Dahlia Fischer, Anthony Watts, Wolfgang B. Fischer, Petra Göring, Ralf B. Wehrspohn, Ulrich Gösele, Claudia Steinem (2004)
"Channel activity of a viral transmembrane peptide in micro-BLMs: Vpu_{1-32} from HIV-1"
submitted to Chemistry and Biology

Oral presentation:

"Nano-BLMs on highly ordered porous alumina - preparation, stability and insertion of ion channels"
3rd Bio Sensor Symposium, March/April 2003, Potsdam, Germany

Poster presentations:

"Pore-spanning lipid bilayers mimicking the cell membrane"
NanoBioTec 2001, September 2001, Münster, Germany

"Solid supported lipid bilayers on different porous substrates"
Jahrestagung der Deutschen Gesellschaft für Biophysik, September 2002, Dresden, Germany

A7 Curriculum vitae

Personal Data

Name:	Winfried Römer
Date of Birth:	July 10, 1976
Place of Birth:	Höchstädt an der Donau (Germany)
Nationality:	German
Marital Status:	Single
Address:	Wilhelm-Bauer-Str. 35, 89407 Dillingen an der Donau (Germany)
E-mail:	winfried.roemer@chemie.uni-regensburg.de

Relevant scientific education

since 09/01:	PhD studies at the Institute of Analytical Chemistry, Chemo- and Biosensors, University of Regensburg (Germany) Thesis: “Impedance analysis and single ion channel recordings on pore-suspending lipid bilayers based on highly ordered pore arrays” Supervisor: Prof. Dr. Claudia Steinem
04/02:	Training in single ion channel recordings at the University of Oxford (UK), Department of Biochemistry, Biomembrane Structure Unit
02/02:	Training in semiconductor electrochemistry and scanning electron microscopy at the MPI of Microstucture Physics in Halle (Germany)
10/01:	Training in membrane biology at the University of Münster (Germany), Department of Biochemistry
11/96 - 08/01:	Studies in biology and chemistry at the University of Regensburg (Germany) Degree: 1st state examination in biology and chemistry
11/99 - 07/00:	“Zulassungsarbeit” at the Institute of Analytical Chemistry, Chemo- and Biosensors, University of Regensburg Subject: „Immuno-chromatographic pregnancy test” Supervisor: Prof. Dr. Otto S. Wolfbeis

STATEMENT OF INDEPENDENCE

Herewith, I declare that I have conceived and written this dissertation without any inadmissible help and/or material that has not been explicitly indicated. All sources of information that were used have been referred. This dissertation has not been submitted elsewhere, neither in- nor outside the country. I have not previously attempted to complete this or any other PhD thesis.

Regensburg, June 2004

Winfried Römer